Dipl.-Ing. Hannes Grübler, BSc

System Design of Fractional Horsepower Electric Drives

DOCTORAL THESIS

to achieve the university degree of

Doktor der technischen Wissenschaften (Dr. techn.)

submitted to

Graz University of Technology, Austria

Supervisor and First Assessor:
Univ.-Prof. Dr.-Ing. Annette Mütze
Electric Drives and Machines Institute, Graz University of Technology, Austria

Second Assessor:
Prof. Dr. Damir Žarko
Department of Electric Machines, Drives and Automation, University of Zagreb, Croatia

Graz, April 2021

AFFIDAVIT

I declare that I have authored this thesis independently, that I have not used other than the declared sources/resources, and that I have explicitly indicated all material which has been quoted either literally or by content from the sources used. The text document uploaded to TUGRAZonline is identical to the present doctoral thesis.

Date	Signature

Contents

Table of Contents I

Abstract 1

Zusammenfassung 3

Acknowledgments 5

1 Introduction 7

1.1 Background of the Work . . . 8

1.1.1 Research Questions . . . 8

1.1.2 Auxiliary Drives in Automotive Applications . . . 8

1.2 Brushless Drives . . . 10

1.2.1 General Introduction . . . 10

1.2.2 Introduction to Small BLDC Machines . . . 11

1.2.3 Software in Use . . . 17

1.3 List of Publications . . . 19

2 Baseline Illustrations 21

2.1 Example Case Drive . . . 21

2.2 FHP Specific Modeling Particularities . . . 25

2.2.1 Analytic Model of the Selected Example Case Drive . . . 26

2.2.2 FEA Model of the Example Case Drive . . . 26

2.2.3 Model Improvements . . . 28

2.3 Comments on Design Techniques . . . 30

3 Improved Modeling Approaches 33

3.1 Iron Losses . . . 33

3.1.1 Modified Loss-Surface Method . . . 35

3.1.2 Loss-Surface–Based Iron Loss Prediction . . . 37

3.1.3 Comparison of Iron Loss Measurements and Loss-Surface Prediction . . . 38
3.1.4 Example Case Study with the Example Case Drive . . . 40
3.1.5 Summary Iron Loss Determination . . . 44
3.2 Stray Paths . . . 45
3.2.1 Permanent Magnet Related Stray Paths . . . 45
3.2.2 Current Related Stray Paths . . . 48
3.2.3 Summary Stray Paths . . . 51

4 Computer Aided System Optimization 53
4.1 Statement of the Problem . . . 53
4.2 Choice of an Optimization Methodology . . . 54
4.2.1 Gradient-Based Optimization . . . 54
4.2.2 Stochastic Optimization . . . 54
4.2.3 Optimization Technique Selection . . . 56
4.2.4 Employing the Optimization Methodology to the Models . . . 56
4.3 Multiphysical System Modeling . . . 58
4.3.1 Setup . . . 58
4.3.2 Example Case Study: Switching Angle Optimization for a BLDC Switching Strategy . . . 59
4.4 Surrogate Modeling . . . 63
4.4.1 Overview . . . 63
4.4.2 Investigated Space Mapping Approach . . . 64
4.5 Summary Computer Aided System Optimization . . . 68

5 Reflections on the Topic 69
5.1 Systematic Design Workflow . . . 69
5.2 Example Case Study . . . 74
5.2.1 Topology Choice Workflow . . . 74
5.2.2 Design Workflow . . . 76
5.2.3 Compilation of Design Data . . . 78
5.2.4 Summary Example Case Study . . . 78

Conclusion 81

A Baseline Illustrations 83
A.1 Test-Setup for Static Material Investigations . . . 83

A.1.1 Baseline Illustrations for Material Investigations 83
A.1.2 Description of the DC-Test 83
A.2 Details of the FEA Models Used 84
A.3 Analytic Model as MATLAB® Code 86

B Improved Modeling Approaches **91**
B.1 Details on Loss-Surface Investigations 91
B.1.1 Overview 91
B.1.2 Test Setup for Loss-Surface Measurements 93
B.1.3 Toroidal Iron Sample for Loss-Surface Measurements 93
B.2 Test-Setup for Stray Path Investigations 95
B.2.1 Description 95
B.2.2 Measurements 95

C Computer Aided System Optimization **97**
C.1 Switching Angle Investigations 97
C.1.1 Test-Setup for Switching Angle Investigations 97
C.2 Space Mapping 98
C.2.1 Transformation Case Study 98

Bibliography **101**

Abstract

The automotive industry is facing significant changes. Never before, advances in decarbonizing the drive train or automated driving have been discussed so clearly. In the shadow of the main propulsion machine or integrating new sensor technologies in cars, auxiliary drives are only of minor interest in the research community. But also here, the recent trends and developments call for the redesign of well established auxiliary systems. Examples are electrical brake boosters, transmission actuation, or electrical power steering. Although such systems have already been established in series cars, tightened requirements on safety for automated driving, or efficiency for drives in continuous operation continue to challenge design engineers.

This thesis contributes to established models and workflows, widely used for designing electric machines. Looking at iron losses, widely used approaches, e.g., based on the Steinmetz equation, underestimate iron losses and require the aid of correction factors. Utilizing a loss-surface approach, based on experimental data, the difference between experimental and loss-surface results can be reduced to below 5 %. Magnet related stray paths and inductances are analyzed and separated, due to limited knowledge thereof for fractional horsepower electric motors. Finite element analysis (FEA) is mainly used for these investigations, where experimental data for the stator laminations and the rotor yoke is used for considering material degradation.

Eventually, an analytic model, extended by the developed loss-surface approach, the enhanced 3D-finite element (FE) model, and a multiphysical system model are linked together via software. An alternative approach for computational expensive models is discussed. A design workflow, utilizing these models and allowing for the automation of repetitive tasks is implemented. By comparison to an established design process, 33 % savings in design time is expected thereof. Modular setup of the models enables for the straightforward extension or sharing of the findings in the future.

Zusammenfassung

Die Automobilindustrie befindet sich in einem bedeutsamen Wandel. Nie zuvor wurden Fortschritte im Bereich der CO_2-Reduktion von Antriebssträngen oder das automatisierte Fahren so deutlich diskutiert. Im Schatten dieser frequentierten Forschungsgebiete sind jedoch Hilfsantriebe für automotive Anwendungen nur ein Nebenschauplatz. Nichtsdestotrotz erzwingen Umbrüche in der Automobilindustrie auch Neuentwicklungen im Bereich gut etablierter Hilfssysteme im Fahrzeug. Beispiele für solche Hilfssysteme sind elektrische Bremskraftverstärker, Aktuatoren im Getriebe und elektrische Servolenkungen. Obwohl diese Hilfssysteme bereits seit vielen Jahren eingesetzt werden, gibt es für die Entwickler durch steigende Anforderungen im Bereich Sicherheit oder Energieeffizienz immer noch Herausforderungen zu bewältigen.

Diese Dissertation trägt zu einer Verbesserung etablierter Modelle und Methoden für das Design elektrischer Kleinantriebe bei. Am Beispiel der Berechnung von Eisenverlusten in elektrischen Maschinen ist der Einsatz von Zuschlagsfaktoren üblich. Die Anwendung eines entwickelten *loss-surface* Verfahrens kann diesen Unterschied zwischen Berechnung und Messung reduzieren, und unter 5 % halten. Magnetische Streupfade werden jeweils analysiert und aufgeteilt, um einen Informationsgewinn für elektrische Kleinantriebe zu erhalten. Die Materialveränderung durch Bearbeitung wird bei der dabei verwendeten FEA durch den Einsatz experimentell ermittelter Materialdaten berücksichtigt.

Abschließend wird ein *Design Workflow* unter Einbeziehung der aus der verbesserten Modellierung gewonnenen Erkenntnisse aufgebaut. Alle eingesetzten Modelle wurden über eine Modellierungs- und Optimierungs-Software miteinander verknüpft. Diese Software ermöglicht eine Automatisierung sich wiederholender Vorgänge, wie etwa bei der Optimierung. In diesem Zusammenhang wird auch eine Methode zur Verringerung der Rechenzeit von aufwändigen Modellen diskutiert. Im Vergleich zu einem etablierten *Design Workflow* wird damit eine Zeitersparnis von 33 % erreicht. Dieser modulare Aufbau der eingesetzten Modelle ermöglicht in Zukunft eine einfache Erweiterbarkeit.

Acknowledgments

This dissertation was written within the framework of the Christian Doppler Laboratory for Brushless Drives for Pump and Fan Applications at Graz University of Technology, Graz, Austria, between April 2016 and April 2021.

At this opportunity, I would like to leave a thank you for all the people who accompanied me on this journey:

First and foremost, I would like to thank my doctorate supervisor Prof. Dr.-Ing. Annette Mütze who gave me the opportunity to write this thesis and endlessly supported me on the way.

Special thanks go to my beloved girlfriend Barbara, my parents Renate and Manfred, as well as my friends and relatives for their understanding, support, and encouragement.

Next, I would like to thank my colleagues at the Electric Drives and Machines Institute for the fruitful discussions and helping out whenever when I was stuck at some point.

I would also like to thank Prof. Dr. Damir Ẑarko from the Department of Electric Machines, Drives and Automation, University of Zagreb, Croatia for taking on the role as second assessor.

I am also grateful for the outstanding cooperation with the Mechatronic Systems GmbH, Wies, Austria. In memoriam of DI Hans-Jörg Gasser.

The financial support from the Christian Doppler Research Association (CDG) is gratefully acknowledged.

Chapter 1

Introduction

Designing permanent magnet (PM) fractional horsepower (FHP) motors for automotive drives, primarily pump and fan applications, has recently seen increased interest, e.g., [1–5]. Changes in the automotive sector, such as automated driving, extensive requirements on reliability and heightened interest in high efficiency, even in the FHP range, require sophisticated design techniques to meet the industry's high standards. Not only costs and volume, but also characteristics such as efficiency, noise-vibration-harshness (NVH), and electromagnetic compatibility (EMC) must be considered at an early design stage of such a drive, in order to prevent time-consuming design iterations. Modeling these characteristics requires multi-physical simulations, which are known to be computationally expensive. Additional, datasheet values may not hold anymore for some of the model components, since the small geometries are more exposed to the manufacturing process and suffer from a relative larger degradation than their conventional integer horsepower counterparts.

This thesis adresses such selected challenges by identifying the limitations of existing design methodologies and suggesting appropriate solutions for use with FHP drives. With respect to improving the modeling approaches, a method to determine the iron losses based on a well-defined experimental approach is suggested. With additional experimental investigations, the obtained material data can also be used for enhancing motor models, e.g., the FE model. Such an accurate motor model can then be integrated in a superior system optimization framework. This thesis investigates the use of a surrogate model and its role in substituting the need of FEA. The use of the different models within an optimizer routine is analyzed, too. The thesis concludes with reflections on the topic, notably an interpretation of the use of the findings to enhance industrial design processes.

1.1 Background of the Work

1.1.1 Research Questions

State of the art design processes for automotive auxiliary drives use a combination of analytic predictions with subsequent FEA. As the use of the software is time consuming and the computational power is limited, the number of possible individuals for comparison and multiphysical investigations is small.

This thesis identifies the compromises inherent in the use of established design techniques when applied to the design of FHP drives and suggests appropriate solutions. In detail, the following research questions are addressed:

- Improved Modeling Approaches
  - How can iron losses be estimated with satisfactory accuracy and effort?
  - How can stray paths be modeled with satisfactory accuracy and effort?
- Computer Aided System Optimization
  - What are promising approaches to reduce design time?
  - Which optimization methods are suitable?
  - How can the relationship between input parameters and output performance parameters be quantified?
- Reflections on the Topic
  - What is, considering a given optimization process, an appropriate design methodology?

1.1.2 Auxiliary Drives in Automotive Applications

The significance of research in the field of FHP drives for automotive applications is illustrated by analysis of such drives in a common series car. The focus is on auxiliary drives for pump and fan applications in the fractional horsepower range, i.e., below 200 W. The Golf series of the Volkswagen AG is chosen for illustration, i.e., the earlier Golf III (production period 1991-1997) and the more recent Golf VII (production period 2012-2019). The FHP drives are classified into performance (e.g., starter), safety (e.g., electromechanical brake booster), and comfort (e.g., electromechanical window lifter) related applications. The results, shown in Figures 1.1 and 1.2, and

Tables 1.1 and 1.2, respectively, build on data obtained from the cars' circuit diagrams of the cable harness, obtained from [6,7]. Within some 11 to 12 years, the number of FHP drives more than doubled, from 23 to 47, with the largest increase with comfort related drives.

The increase in the number of total auxiliary drives is clearly visible, especially in the number of comfort related drives, however, pumps and fans still have a significant share. Most of these latter drives are in continuous use, e.g., transmission actuation [8], brake systems [3,9,10], and advanced thermal systems [11], and thus play a central role in the performance of the vehicles in terms of energy usage and have been also becoming more safety relevant recently, as underlined in the references. However, such a development renewed interest not only in the performance parameters of these small drives, but also in fault tolerance, durability, electromagnetic emission, and noise.

With 47 auxiliary drives per car, and 850.000 Golf VII produced in 2019 [12], already 40.000.000 auxiliary drives were produced for the Golf VII in 2019 only.

Table 1.1: FHP drives of the Golf III (basic version), 23 auxiliary drives in total.

application	number	share	type	number	share
performance	10	43.5 %	fans	4	17.4 %
safety	6	26.1 %	pumps	3	13.0 %
comfort	7	30.4 %	other	16	69.6 %

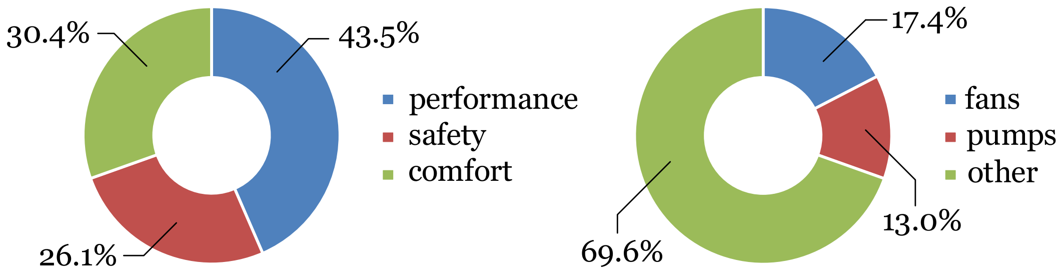

(a) (b)

Figure 1.1: Golf III (basic version) FHP drives breakdown with (a) separation into performance, safety, and comfort related drives and (b) separation into fan, pump, and other applications with 23 drives in total; data based on [6].

Table 1.2: FHP drives for Golf VII (basic version), 47 auxiliary drives in total.

application	number	share	type	number	share
performance	15	31.9 %	fans	5	10.6 %
safety	9	19.2 %	pumps	7	14.9 %
comfort	23	48.9 %	other	35	74.5 %

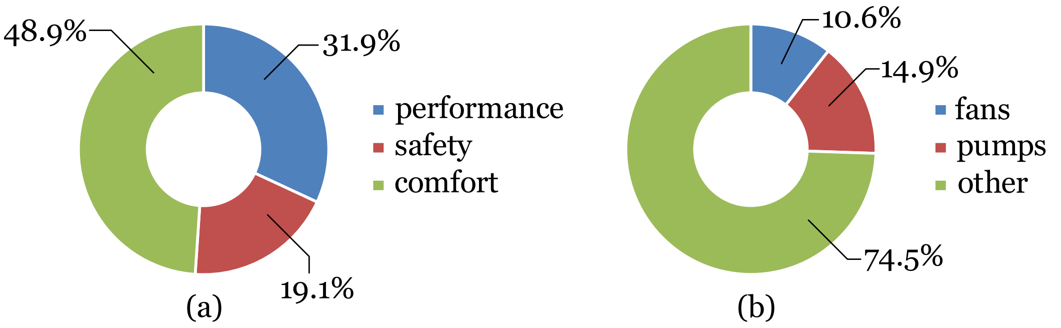

(a) (b)

Figure 1.2: Golf VII (basic version) FHP drives breakdown with (a) separation into performance, safety, and comfort related drives and (b) separation into fan, pump, and other application with 47 drives in total; data based on [7].

To put the number of auxiliary drives in context, the authors of [13] investigated an executive car, an S-Class limousine from Mercedes Benz, and identified 135 auxiliary drives, the authors of [14] also mention around 100 electric drives in one car. In comparison to the basic version of a recent Golf class from Volkswagen with close to 50 auxiliary drives, the limousine investigated in [13] has more than 2.5 as many auxiliary drives as the Golf. This can be explained mostly by more comfort related drives, i.e., actuators for seat adjustment or fans for seat ventilation.

1.2 Brushless Drives

1.2.1 General Introduction

Owing to their advantages, brushless direct current (BLDC) motors have been progressively substituting established motor concepts in many applications. Today, BLDCs are used in office automation, household appliances, and especially in the automotive sector and aerospace industry [15]. Examples are given by, transmission actuation [8], advances in thermal systems [11], electric brake boosters [3], LED car headlights [4], electric oil pumps for gearbox lubrication [5], electric servo steerings [16], and many other auxiliary electric drives [17]. The high degree of integration in such applications often brings forth additional, partially demanding requirements, for example on efficiency (e.g., additional heat in an already highly integrated application), acoustic noise (e.g., household appliances or drives in the passenger compartment), electromagnetic interference (especially for automotive applications), volume (e.g., integration of a drive in an existing application), robustness (e.g., extreme temperature range from -40 to 120 °C, vibrations, lifetime of 10 years and more), drift of parameters (e.g., bearing wear-out), cost-efficiency, and manufacturability (e.g., few and easily mountable parts). BLDCs are known for high efficiency, high power density, low rotor inertia and weight, good controllability, and for low-maintenance [18]. On the downside, position sensors, e.g., encoders or Hall effect sensors, are required for effective control. Estimation-based, i.e., sensorless control strategies have also been proposed, which, on the one hand, reduce the component count, but, on the other hand, are more complex and often lack precision [18–20].

BLDC motors can be manufactured in many different designs such as with inner- or outer-rotor, or with surface or interior magnets. In low-cost and FHP applications, the single-phase stator often houses a concentrated winding which can be either of unifilar or of bifilar type. These motors are combined with an inverter circuit responsible for the electronic commutation [20].

1.2.2 Introduction to Small BLDC Machines

Most of the motors used in cars are permanent magnet electric motors. They provide a high energy density which results in small size machine designs. Many of them use brushless (electrical) commutation instead of mechanical brushes and commutators. These machines can generally be separated into two types of motors [21]:

- Brushless DC Motors (BLDC)
- Permanent Magnet Synchronous Motors (PMSM)

These two machines differ by their commutation. While PMSMs are sine commutated, BLDC motors normally do have block commutation. Therefore, another difference between PMSM and BLDC machines is the back-electromotive force or BEMF (u_{EMF}). Different magnetization of the magnets lead to either a sine wave BEMF or to a trapezoid-shaped BEMF.

Figures 1.3(a) and (b) show the BEMF and the phase current of one phase of a PMSM (often used with sine wave BEMF), and an BLDC motor, respectively (usually operating with trapezoidally-shaped BEMF).

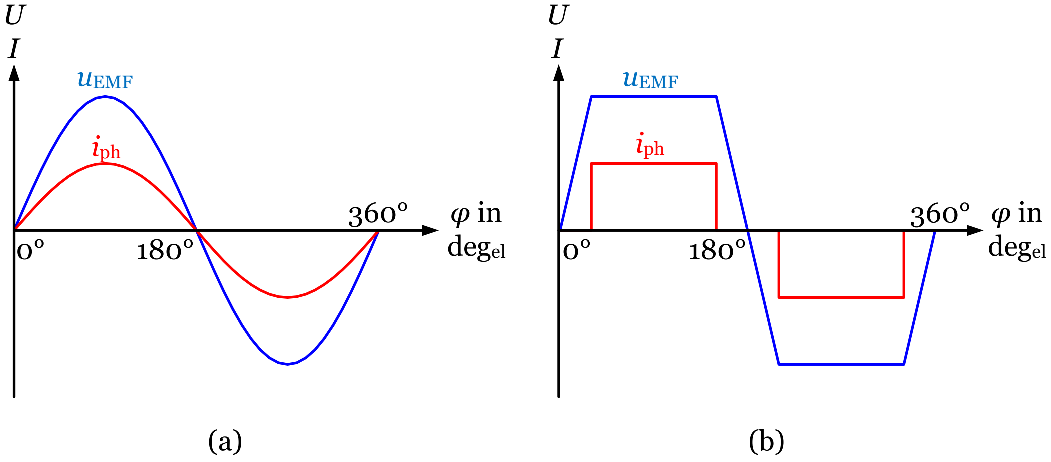

Figure 1.3: BEMF and phase current (a) for PMSM machines and (b) for BLDC machines.

Advantages of BLDC motors include lower switching losses, because PWM is not essential but widely used for current control, and lower costs because BLDC motors do need less information on the rotor position resulting in lower part count, especially for single phase types. On the other hand, the BLDC machines produce higher torque ripples during commutation and therefore more noise, together with higher core losses, due to higher harmonics [22].

Electric machines in general, and hence BLDC machines, can be further divided by the positioning or placement of the rotor and the stator [23, p. 117-124]:

Figures 1.4(a) and (b) illustrate inner-rotor and outer-rotor machines respectively. These two motor types differ in their fields of application. Inner-rotor type motors are often used in highly dynamic applications, because of their lower inertia. Another advantage is that the windings are on the outside and thus the heat resulting from the copper loss can be better extracted. In contrast to this, the windings of outer-rotor motors are easier to assemble, and the motors have a larger relative air-gap radius what increases the torque. In addition, fan blades can be directly attached to the rotor, and hence outer-rotor machines are often used in pumps, fans, and hard disc drives [23, p. 117-124].

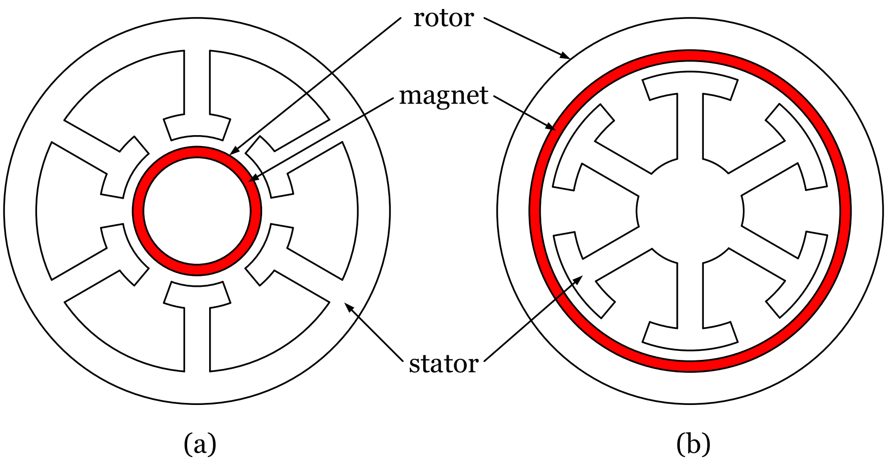

Figure 1.4: Illustration of (a) inner-rotor and (b) outer-rotor motor topology, as per [23, p. 117-121].

Furthermore, machines can be distinguished by their number of phases, namely multi-phase and single-phase machines. Most multi-phase machines are designed as three phase machines as shown in Figure 1.5(a). To enhance safety, e.g., for automated driving, multi-phase machines could be of increasing interest, as illustrated by a five-phase steering actor presented in [24]. Because of their higher efficiency (always two phases are energized) they are commonly used in applications where more power is needed. In addition, with multi-phase machines, the return conductor can be omitted. Such machines normally need twice the number of switches as they have phases, i.e., six switches in the case of a common three-phase machine, for their control. The electric circuit is illustrated in Figure 1.6.

Due to a comparatively lower efficiency, single-phase machines are typically used for powers of up to a few watts. Although they are less efficient than three phase motors as outlined above, they are less costly and easier to manufacture [25].

Single-phase brushless DC motors are often used in applications where low starting torque is needed, e.g., pumps or fans.

Single-phase motors have the disadvantage that they have positions with zero torque (also called dead points) which can lead to problems at the start of the motor. Therefore, these machines need auxiliary measures such as an asymmetric air gap to create an additional reluctance torque component. This can be realized

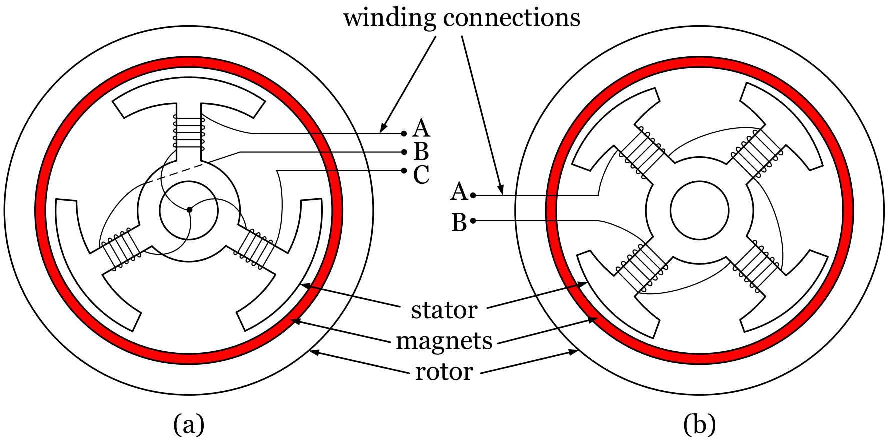
winding connections
A
B
C
A
B
stator
magnets
rotor
(a)
(b)

Figure 1.5: Model of (a) a 3-phase motor adapted from [26] and (b) a single-phase motor design, illustrated as per [2].

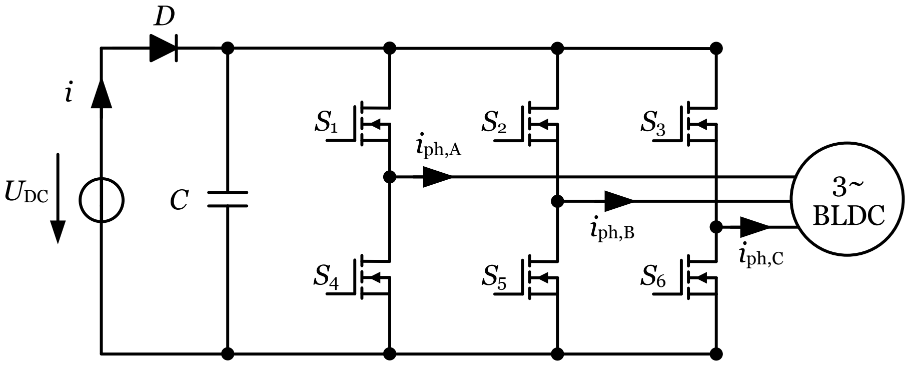
D
i
U_{DC}
C
S_1
S_2
S_3
S_4
S_5
S_6
$i_{ph,A}$
$i_{ph,B}$
$i_{ph,C}$
3~
BLDC

Figure 1.6: Electric circuit for the three phase machine, illustrated as per [27].

with a tapered-air gap, with stepped-teeth, with asymmetric-teeth, or with notched-teeth [28]. As per [29], a tapered-air gap is best in terms of cogging torque peaks. Another method to obtain a self-starting rotor position can be achieved with parking magnets. This has the disadvantage of more costs for the motor and is hence not often used with small machines [30].

Single-phase machines can be separated into monofilar and bifilar wound motors, as illustrated in Figures 1.7(a) and 1.7(b).

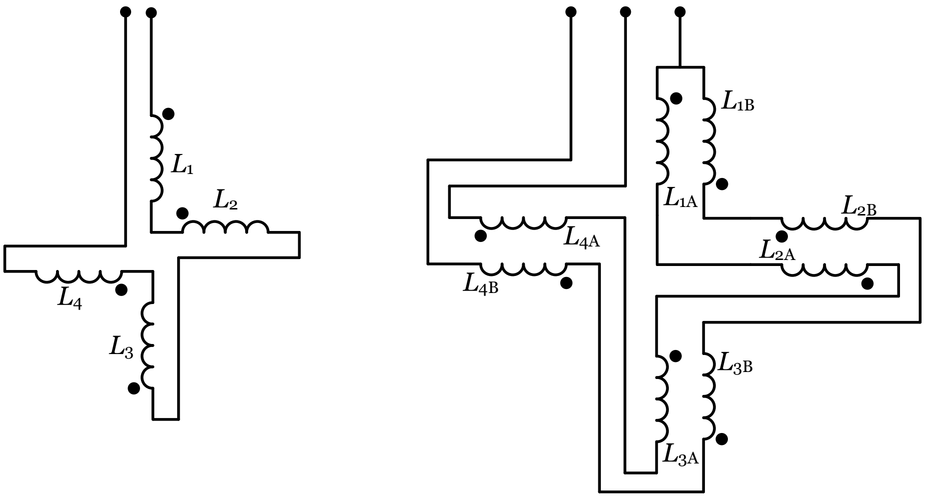

(a) (b)

Figure 1.7: Winding configuration: (a) monofilar winding from [31], and (b) bifilar winding, illustrated as per [32].

Monofilar wound motors only have one wire, which is wound alternating around the stator teeth. In contrast, bifilar wound motors have two coils wound around each tooth in alternating directions. Here, one end of one coil is connected to the end of the other coil, and the winding terminals are connected separately.

The electric circuits of a monofilar and of a bifilar wound machine are shown in Figures 1.8 and 1.9, respectively. The BLDC motor is represented as a serial connection of an inductance, a resistor, and the BEMF-source.

Machines with monofilar windings need four switches to run the motor. Although bifilar wound motors need more copper than monofilar wound machines, they only require two switches. Hence, bifilar wound machines are more common in low budget drives. Recent trends of integrating power electronics and logic to a system

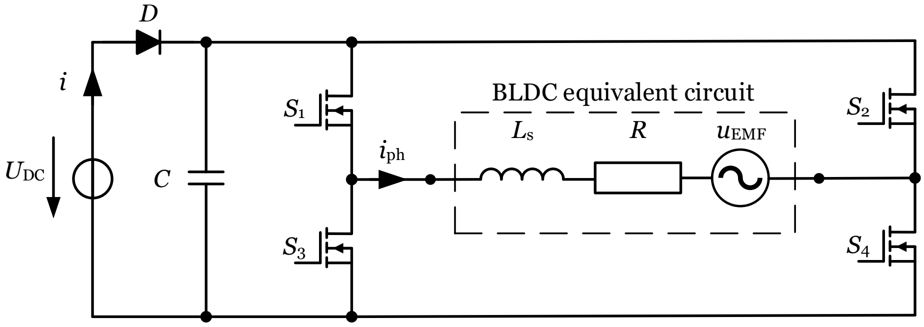
D
i
U_{DC}
C
S_1
S_3
i_{ph}
BLDC equivalent circuit
L_s
R
u_{EMF}
S_2
S_4

Figure 1.8: Electric circuit of a single-phase BLDC machine with a monofilar winding, illustrated as per [33].

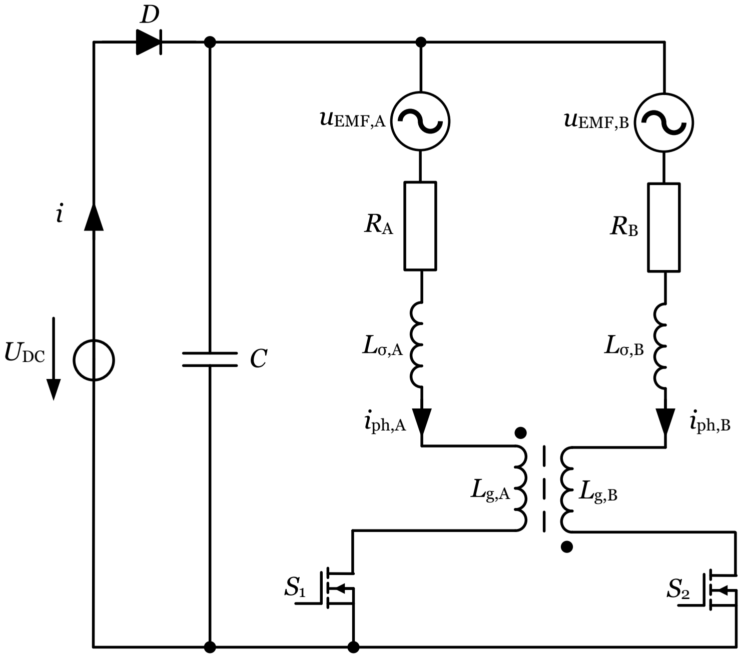
D
i
U_{DC}
C
$u_{EMF,A}$
$u_{EMF,B}$
R_A
R_B
$L_{\sigma,A}$
$L_{\sigma,B}$
$i_{ph,A}$
$i_{ph,B}$
$L_{g,A}$
$L_{g,B}$
S_1
S_2

Figure 1.9: Electric circuit of a single-phase BLDC machine with a bifilar winding, illustrated as per [34].

on chip may bring a shift into the selection of these motor topologies, because, as presented in [35], integration of control logic and power electronics on one integrated circuit is possible.

1.2.3 Software in Use

The following software is used in Chapter 4 for the implementation of a multiphysical system setup, introduced at this point to give a central overview. The models of the multiphysical setup are implemented with the following software, which are interfaced with Python® scripts.

Python®

Python® is a programming language, extendable with libraries for scientific computing, interfacing other software, or visualization. For executing the Python® scripts the Python® interpreter of SyMSpace® is used.

SyMSpace®

SyMSpace® is a software framework for simulation and optimization of generic systems and models. Hence, the name is an acronym of System Model Space. The software consists of two main components: One for systematic model setup and simulation, the other for stochastic optimization, linked via an internal interface. The software is mostly open source, and large parts are free to use. Python® is utilized twofold: To implement certain models via internal scripts, and to interface simulation software for accessing external models.

LTSpice®

LTSpice® is a simulation software for electronic circuits based on the SPICE® solver. A function block for numerical integration allows solving auxiliary differential equations, here to simulate the mechanical system of pumps and fans, the electric motor, and the electronic ciruit. LTSpice® is interfaced via the Python® programming language, handling the settings for the netlist, starting the simulation via command line, and collecting and post-processing the simulation data. LTSpice® is used for system optimization in combination with the optimizer of the SyMSpace® software package.

JMAG-Designer®

JMAG-Designer® is a software package, with emphasis on designing electromagnetic energy converters. Along with the FE solver, a number of assistants for pre- and post-processing are provided, e.g., meshing or iron loss determination.

Basic circuit simulation is provided with a built-in simulator. For rapid prototyping, pre-defined analytic models of common electromagnetic energy converters are provided via JMAG-express®, which is a subset of JMAG-Designer®. Utilization of the JMAG-Designer® package is discussed in Chapter 5, as part of a comparison to an enhanced design workflow.

JMAG® is additionally used for the investigations in Chapter 3, and for providing the graphical representation of FE models in Chapter 2 and in the Appendix.

Software References

Further information for the introduced software can be found in [36] (Python®), [37] (SyMSpace®), [38] (LTSpice®), and [39] (JMAG®).

1.3 List of Publications

The work presented in this thesis has resulted in the following *first author* publications. The papers are subjected to copyright by the *Institute of Electrical and Electronics Engineers (IEEE)*. The journal publication is an extended version of preceding conference publication (J1/C1).

Journal Publication:

[J1] **H. Gruebler**, S. Leitner, A. Muetze, and G. Schoener, "Improved Switching Strategy for a Single-Phase Brushless Direct Current Fan Drive and its Impact on Efficiency," in *IEEE Transactions on Industry Applications*, vol. 54, no. 6, pp. 6050–6059, Nov.-Dec. 2018.

Conference Publications:

[C1] **H. Gruebler**, S. Leitner, A. Muetze, and G. Schoener, "Improved Switching Strategy for a Single-Phase Brushless Direct Current Motor and its Impact on Motor Efficiency," *2017 IEEE International Electric Machines and Drives Conference (IEMDC)*, Miami, FL, USA, 2017, pp. 1–6.

[C2] **H. Gruebler**, F. Krall, S. Leitner, and A. Muetze, "Loss-Surface-Based Iron Loss Prediction for Fractional Horsepower Electric Motor Design," *2018 20th European Conference on Power Electronics and Applications (EPE'18 ECCE Europe)*, Riga, 2018, pp. P.1–P.8.

[C3] **H. Gruebler**, F. Krall, S. Leitner, and A. Muetze, "Space Mapping-Based Fractional Horsepower Permanent Magnet Motor Design," *2019 IEEE International Electric Machines and Drives Conference (IEMDC)*, San Diego, CA, USA, 2019, pp. 455–460.

Chapter 2

Baseline Illustrations

2.1 Example Case Drive

FHP motor details

The example case motor comprises a four-pole outer PM rotor and a four-slot stator with a concentrated bifilar winding. It is designed to provide a mechanical output power of up to 1 W at a mechanical operating speed of $n = 5000\,\mathrm{rpm}$. Figure 2.1 shows the motor topology, the driver circuit, and a picture of the stator. The drive system is used for an automotive fan application.

Model overview

Figure 2.1 shows an overview of the example case drive, presenting the motor's cross-sectional area with selected dimensions, the corresponding driver circuit and a photo of the stator with bifilar windings. Exemplarily, Figure 2.2 shows two 3D-FEA models of the example case motor, pointing out the rotor overhang (ROH), a typical FHP motor's particularity. This overhang enhances air-gap flux and hence power density but, since the ROH is asymmetric, also introduces axial forces.

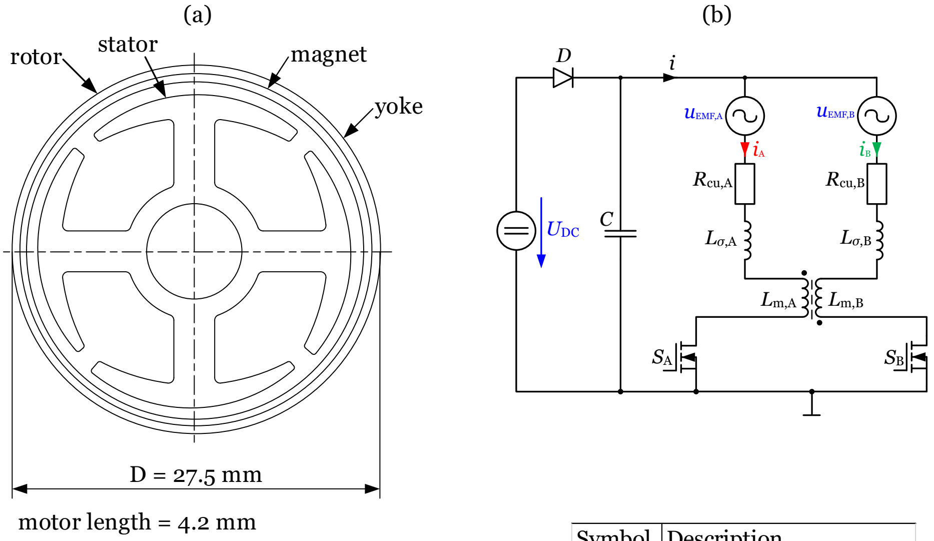
(a)
rotor
stator
magnet
yoke
D = 27.5 mm
motor length = 4.2 mm
(b)
D
i
$u_{\mathrm{EMF,A}}$
$u_{\mathrm{EMF,B}}$
i_{A}
i_{B}
$R_{\mathrm{cu,A}}$
$R_{\mathrm{cu,B}}$
U_{DC}
C
$L_{\sigma,\mathrm{A}}$
$L_{\sigma,\mathrm{B}}$
$L_{\mathrm{m,A}}$
$L_{\mathrm{m,B}}$
S_{A}
S_{B}

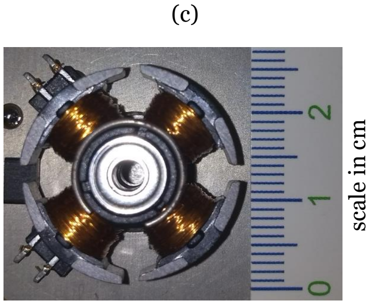
(c)
0
1
2
scale in cm

Symbol	Description
U_{DC}	on-board power supply
D	diode
C	capacitor
i	total current
$u_{\mathrm{EMF,A\text{-}B}}$	back EMF
$R_{\mathrm{Cu,A\text{-}B}}$	winding resistance
$L_{\sigma,\mathrm{A\text{-}B}}$	stray inductance
$L_{\mathrm{m,A\text{-}B}}$	main inductance
$S_{\mathrm{A\text{-}B}}$	switches

Figure 2.1: Example case drive: (a) sketch of the rotor and stator with selected dimensions, (b) electric driver circuit including motor equivalent circuit, and (c) photo of the stator with the bifilar windings.

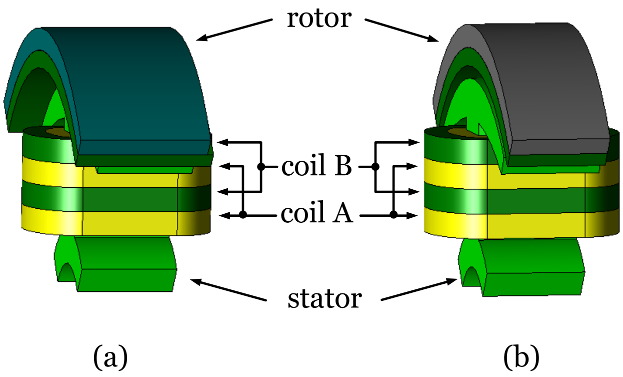

Figure 2.2: 3D-FEA models of the example case FHP motor; (a) with ROH, (b) without ROH; the BEMF computed from the 3D model without ROH is equivalent to the one computed from the 2D-FEA model, confirming the important role of the ROH; [40].

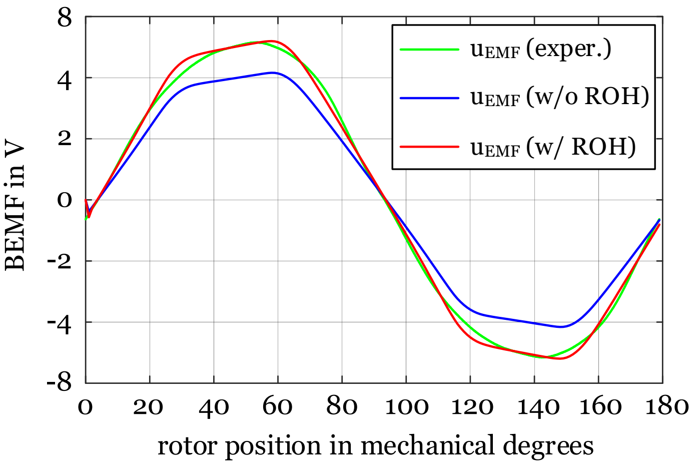

Figure 2.3: FEA investigation with the models shown in Figure 2.2, illustrating the impact of the ROH with a difference in BEMF amplitude of 25 %, with well aligned experimental results, as reported in [40].

Inductance

The computation of the main inductance is discussed in Section 3.2.2. The results obtained from a 3D-FEA model with straightforward settings for coil configuration, material settings according to the respective datasheets, and magnet setup, as shown in Figure 2.4 (a), differ by 47 % from the measured value. The bifilar winding of the example case machine has thus been modeled as an eight layer winding, as shown in Figure 2.4 (b). The material parameters of the core and of the yoke are adjusted by data determined experimentally, hence, material data that included the manufacturing process, see Figure 2.5. Thereby, the computational error of the inductance could be reduced down to 22 %.

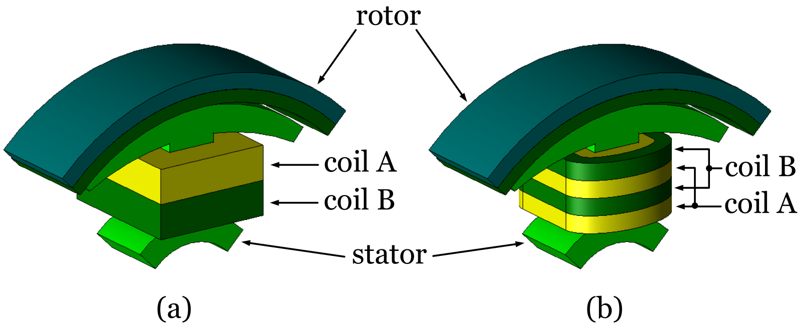

Figure 2.4: Improved modeling of the bifilar winding, whereby the straightforward representation of two lumped windings is replaced by an eight-layer winding;[1] [40]. This measure improved the modeling accuracy by 5 %.

Material degradation

The material degradation due to the manufacturing process is a recurring topic. The relatively large impact of the cutting process on the small geometric structures, as present with FHP motors, leads to very different material parameters than presented in the datasheets. Experimental results of material investigations presented in Figures 2.5 (a) and (b) support this expectation, since the measured relative permeabilities differ from the relative permeabilities stated in the datasheets by up to a factor of five. The cutting process does not only influence (as the commonly used correction factors suggest) the iron losses, but also the motor's magnetization characteristic and hence the parameters of the equivalent circuit, such as the motor inductance.

---

[1] The actual implementation of the winding is shown in Figure 1.7 in Section 1.

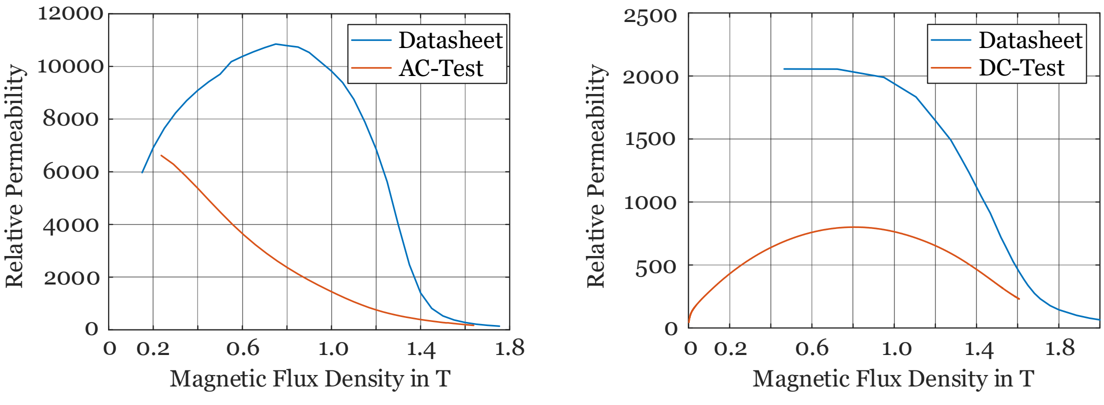

(a)

(b)

Figure 2.5: Comparison of datasheet values versus experimental results of $\mu_r B$-curves of (a) stator laminations and (b) rotor back iron. Details on the experiments are given in Appendix A.1 and Appendix B.1.2.

2.2 FHP Specific Modeling Particularities

This section presents an analytic and a 3D-FEA model of the example case drive. The models will be used for application of a surrogate model described in Section 4.4.

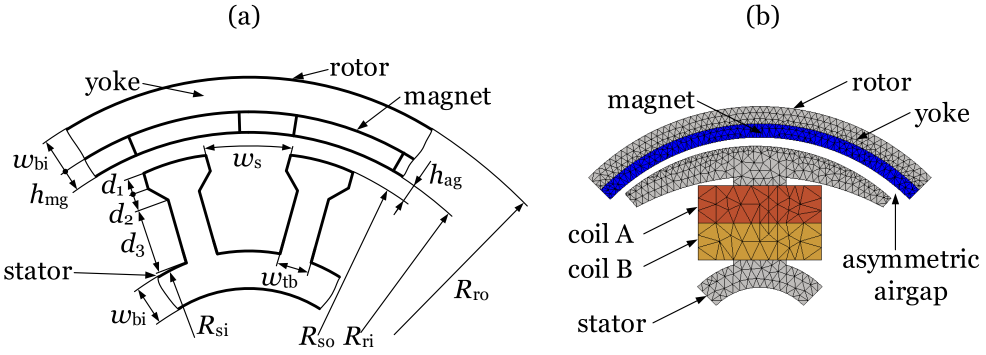
(a)
(b)
yoke
rotor
magnet
w_{bi}
h_{mg}
w_s
h_{ag}
d_1
d_2
d_3
stator
w_{tb}
w_{bi}
R_{si}
R_{so}
R_{ri}
R_{ro}
magnet
rotor
yoke
coil A
coil B
asymmetric airgap
stator

Figure 2.6: (a) coarse model (sketch with geometric parameters), (b) fine model (quarter 3D-FE model of the motor due to symmetries).

2.2.1 Analytic Model of the Selected Example Case Drive

A sketch of an outer rotor PM machine, along with independent model parameters (see also Tables 2.1 and 2.2), is presented in Figure 2.6(a). An analytic model based on this geometry is usually submitted to an optimization algorithm as the initial step in the proposed design workflow. Appendix A.3 shows the implementation of the analytic model.

The analytic model originates from the equations derived in [41, p. 125ff] and remains as simple as possible, hence, non-linearities of the materials or some geometric characteristics such as the asymmetric airgap are not considered. This demands only low computational effort and eventually allows for stochastic optimization.

While the parameters shown in Table 2.2 are fixed (referred to as specification), the parameters shown in Table 2.1 are left to be varied to identify the geometric structure that provides best performance via automated optimization.

Table 2.1: Varying independent parameter set for the optimization of the coarse motor models geometry.

No.	Varying Parameters	Description
1	R_{so}	outer stator radius
2	h_{ag}	air gap height
3	h_{mg}	magnet height
4	d_1	pole shoe depth 1
5	d_2	pole shoe depth 2
6	d_3	conductor slot depth
7	w_{s}	slot opening
8	L_{mt}	motor length

2.2.2 FEA Model of the Example Case Drive

Figure 2.6(b) shows the example case drive in the form of a 3D-FE mesh created with the JMAG-Designer® software package. This model is used for considering certain unique characteristics of FHP PM machines (e.g., asymmetric airgap, aspect ratios, magnet and winding overhang) or material non-linearities. Although symmetries are exploited, with up to 2h, the computational time for the transient computation

Table 2.2: Fixed specification parameter set for the optimization of the coarse motor model.

No.	Fixed Parameters	Description
1	α_m	magnet fraction
2	p	number of pole pairs
3	Q	number of stator slots
4	B_r	remanent flux density (PM)
5	H_c	coercive magnetic field (PM)
6	B_max	max. flux density (iron)
7	E_max	max. BEMF at rated speed
8	n_mech	rated mechanical speed
9	P_mech	rated mechnical power
10	N_ph	number of phases
11	k_st	iron stacking factor
12	k_cp	copper filling factor
13	ξ_oh	upper operating temperature
14	ξ_ol	lower operating temperature
15	ξ_ref	reference temperature
16	$\$_\mathrm{Cu,spec}$	specific price for the copper
17	$\$_\mathrm{FeS,spec}$	specific price for the stator stack
18	$\$_\mathrm{FeY,spec}$	specific price for the rotor yoke

of the presented fine model is comparably long. Appendix A.2 shows an example of such a computation.

As shown in Figure 2.3, neglecting, e.g., the ROH, causes a comparably large difference between 3D-, and 2D-FEA results. Therefore, 2D-FEA is not suitable to investigate FHP PM motors, because the aspect ratios of these machines require 3D effects to be taken into consideration.

2.2.3 Model Improvements

Iron losses and stray paths were identified as the phenomena of most importance with respect to the improvement of the modeling of FHP motors. The loss overview in Figure 2.7 illustrates their respective paths of influence.

Operating conditions and material characteristics that cause non-linear and often difficult to predict magnetic properties, such as saturation, the cutting process, notably with small structures, and significant harmonic content in the distribution of the flux density, alter the material behavior as provided by the datasheets. Construction constraints for low-cost applications, i.e., limited space, may, in addition, result in non-ideally distributed magneto-motive forces. The approach proposed in this thesis is based on experimental obtained datasets. It not only enhances the iron loss determination, but also contributes to improving the modeling of the stray paths by utilizing these experimental data.

Stray paths do not directly account for losses. However, leakage reduces the flux provided by the permanent magnets and by the current flow through the coils and thus increases the current demand to obtain a certain torque. This in turn increases the ohmic losses in the winding, where $P_{\mathrm{Cu}} \propto I^2$. Therefore, any improvement on the stray paths, what requires appropriate modeling, will directly affect the efficiency. Stray paths also significantly influence the inductances of FHP PM machines. Detailed knowledge thereof is important, e.g., for model-based sensorless control strategies. In addition, the leakage inductance shall be kept low so as to decrease the voltage drop across the leakage inductance, since the DC-Link voltage for automotive applications is low in general, and exposed to large variations additionally.

As shown in Figure 2.7, friction related losses also affect the motor performance. They may significantly influence the mechatronic system. Examples are given by, e.g., high viscosity of lubricants at cold temperatures that may increase the start-up

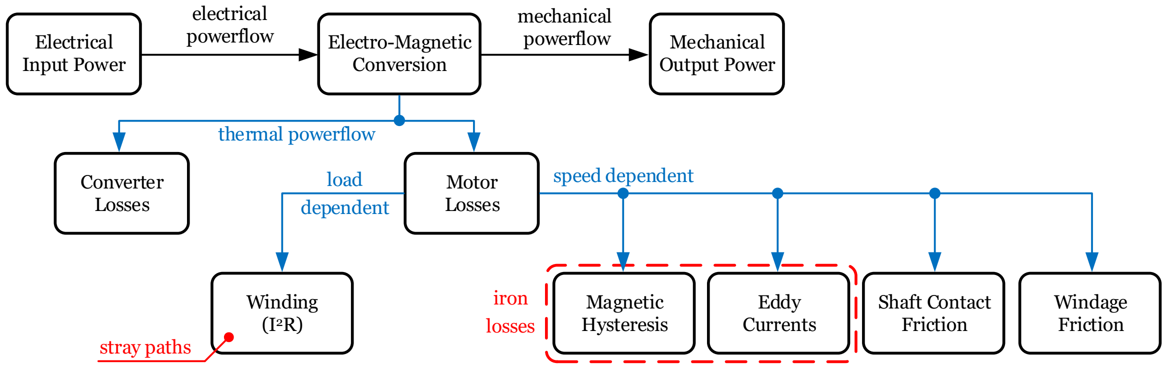
Electrical Input Power
electrical powerflow
Electro-Magnetic Conversion
mechanical powerflow
Mechanical Output Power
thermal powerflow
Converter Losses
load dependent
Motor Losses
speed dependent
Winding (I²R)
stray paths
iron losses
Magnetic Hysteresis
Eddy Currents
Shaft Contact Friction
Windage Friction

Figure 2.7: Loss overview, showing the paths of influence of the parasitic phenomena investigated in detail in this thesis, illustrated as per [42].

torque significantly. Reduction of such losses is, however, beyond the scope of this thesis.

Model improvement illustration based on the Steinmetz equation

For illustrating the improvement of iron loss computation, investigations with the Steinmetz equation:

$$p_{\mathrm{fe}} = k f^{\alpha} \hat{B}^{\beta}, \tag{2.1}$$

are presented here, where p_{fe} is the specific iron loss density in $\mathrm{W/m^3}$, k, α, and β are dimensionless material constants, f is the frequency of the magnetization in Hz, and $\hat{B}$ is the peak flux density in T. The material constants are determined via a parameter fit of datasheet values in a master thesis [43, p. 32], jointly developed with the author of this thesis. The example case drive's lamination material is M250-35A electrical steel. As per Figure 3.5 in Section 3.1.4, the flux densities peak amplitude is 1.4 T, the investigated operating speed of 5000 rpm results in a frequency of magnetization of $166.6\dot{7}$ Hz. Therefore, Table 2.10 in [43, p. 32] provides the material parameters shown in Table 2.3.

Submitting these values to (2.1) provides p_{fe}, with (3.9) in Section 3.1.4, the absolute iron losses P_{fe} can be determined and are presented in Table 2.4.

This result is compared with the findings of Section 3.1.4.

Table 2.3: Steinmetz material parameters for the M250-35A soft magnetic material, for a flux densities peak amplitude of 1.4 T, and a frequency of magnetization of $166.6\dot{7}$ Hz, as provided by Table 2.10 in [43, p. 32].

k	α	β
40.5	1.3	2.5

Table 2.4: Iron loss computation results based on the Steinmetz equation, for the example case drive. $V_{\text{fe, stator}}$ is provided by the CAD data of the FE model.

p_{fe}	$V_{\text{fe, stator}}$	P_{fe}
W/m^3	m^3	mW
$7.3\,10^{4}$	$7.79\,10^{-7}$	56.9

2.3 Comments on Design Techniques

At large, design approaches utilizing estimations based on analytic models, followed by detailed investigations with numerical tools, are used. This is evident by the design frameworks available for machine design, e.g., JMAG Designer® [39]. With a certain experience of the designer, this methodology provides well-suited solutions. However, these approaches do have their limits, e.g., with short development cycles and different requirements on FHP drives, as outlined above for the automotive sector. The characteristics of the different sub-systems are often non-linear, and a seemingly non-optimal design of a given sub-system may lead to a better performance of the overall system. An example for this is presented in [44], an optimal *LC*-filter design for an industrial drive system with some 4 kW rated power is discussed.

This thesis proposes approaches based on system simulation and optimization that allow for selection of the individually optimum tools via implemented interfaces. This enables considerations on a system level providing a good overview of optimal solutions for a given problem. This thesis shows how the models are implemented and linked, and illustrates the approach for the example case drive.

Figure 2.8 gives a qualitative overview of design time for (a) a conventional approach with an FEA tool and trial and error optimization and (b) with enhanced modeling and optimization.

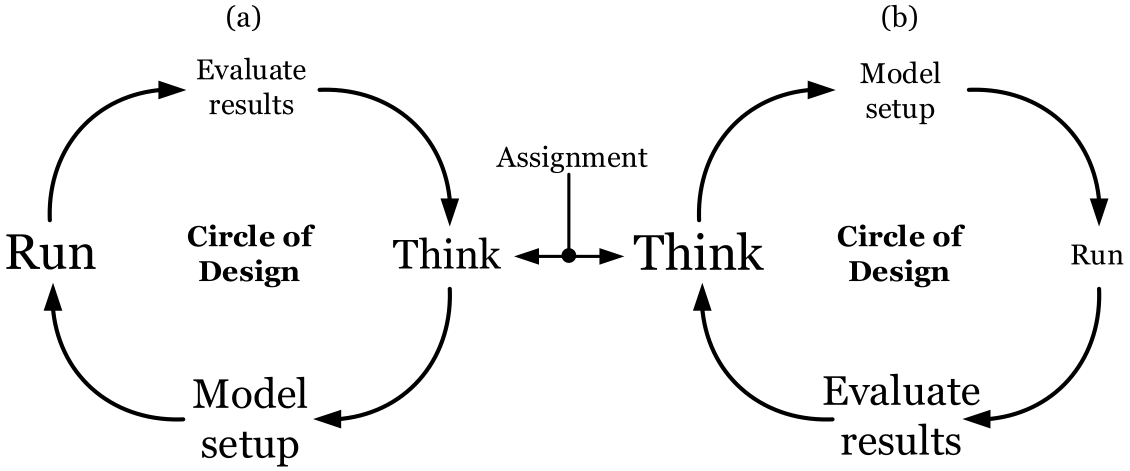
(a)
Evaluate results
Run
Circle of Design
Think
Model setup
Assignment
(b)
Model setup
Think
Circle of Design
Run
Evaluate results

Figure 2.8: Illustration of design circles for (a) a conventional approach with an FEA tool and trial and error optimization and (b) with enhanced modeling and optimization, illustrated as per [45].

Chapter 3

Improved Modeling Approaches

With FHP PM machines, material degradation and manufacturing tolerances have a larger impact on the machine performance than with larger machines. In addition, the unconventional aspect ratios increase the difficulties in modeling machines, notably with respect to their leakage paths. This chapter investigates enhancements of conventional modeling approaches to obtain reasonable accuracy with FHP PM machines too, so as to further analyze selected machine parameters and machine performance parameters.

To this aim, this chapter proposes an improved modeling approach for iron losses and a thorough investigation of the different stray paths. The chapter first reviews established modeling approaches for iron losses and presents the ideas of the loss-surface approach. Then, it investigates the different stray paths. Both analyses include experimental results of the example case drive.

3.1 Iron Losses

State of the art iron loss prediction, such as implemented as part of the post-processing in commercially available FEA software, is typically based on modifications of the well-known Steinmetz equation or approaches based on loss separation (see, e.g., [46] for an overview). The main drawback of these approaches is their reliance on datasheet values, where the parameters for the formulas are optimized for a certain frequency and a range of flux densities. The authors in [47] illustrate how the error in iron loss determination increases when the frequencies of the flux densities differ from those upon the loss parameters are based. Additionally, the influence of the different manufacturing steps on the steel sheets' characteristics is difficult to consider a priori. Figure 3.1 shows an overview of the different models to calculate the iron losses that have been proposed in the literature.

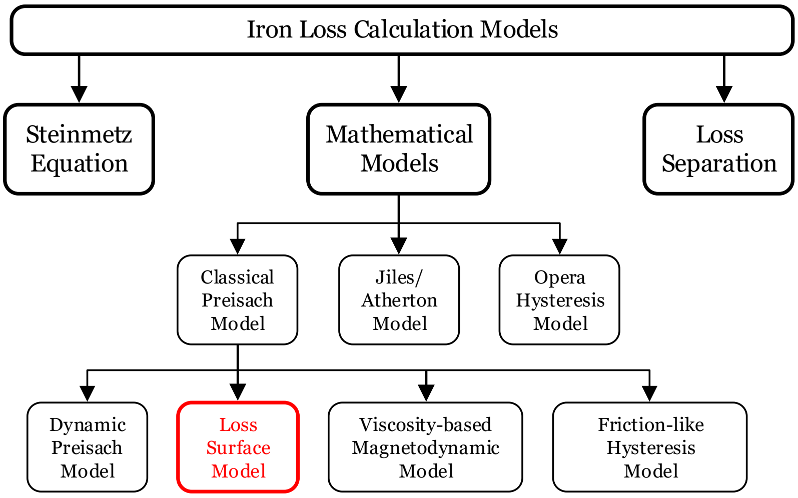
Iron Loss Calculation Models
Steinmetz Equation
Mathematical Models
Loss Separation
Classical Preisach Model
Jiles/ Atherton Model
Opera Hysteresis Model
Dynamic Preisach Model
Loss Surface Model
Viscosity-based Magnetodynamic Model
Friction-like Hysteresis Model

Figure 3.1: Overview of common iron-loss models with a detailed presentation of mathematical models, based on [46].

A loss-surface–based modeling approach provides a suitable alternative to handle the challenges described above. This approach assumes that the material behavior can be thoroughly defined by the amplitude of the flux density B and its time derivative $dB(t)/dt$ in the sheet's cross-section (e.g., [48–50]). The proposed approach links the applied magnetic field H with the flux density B and its time derivative $dB(t)/dt$, representing the material behavior by a characteristic surface $S = p_{\text{spec}}\,(B, dB(t)/dt)$, where p_{spec} are the instantaneous specific iron losses. [48] and [49] propose a separation into static and dynamic material characterization, in which the static part is implemented with hysteresis models based on the well-known approaches of Preisach [51] or Jiles/Atherton [52]. However, mathematical hysteresis models are complex and difficult to implement in design tools such as FEA software. Therefore, the approach proposed in [50] is used in this thesis. It uses a quasi-time-invariant modeling, and hence is indicated by the prefix "modified," described in more detail in the following section.

3.1.1 Modified Loss-Surface Method

The loss-surface of a certain material must be determined experimentally. To this aim, test equipment such as single-sheet-tester, Epstein frame, or toroidal specimen together with corresponding power amplifier and measurement equipment are required. The need for such experimental investigation comes with the advantage of the possibility to consider real test conditions, e.g., the influence of cutting and stacking on specimen of similar size as the final machine/device.

The approach is validated experimentally by applying the algorithm to the example case drive, which is discussed in Section 3.1.4. Figure 3.2 depicts a measured loss-surface for an M250-35A toroidal iron sample. The details are discussed in Appendix B.1.3.

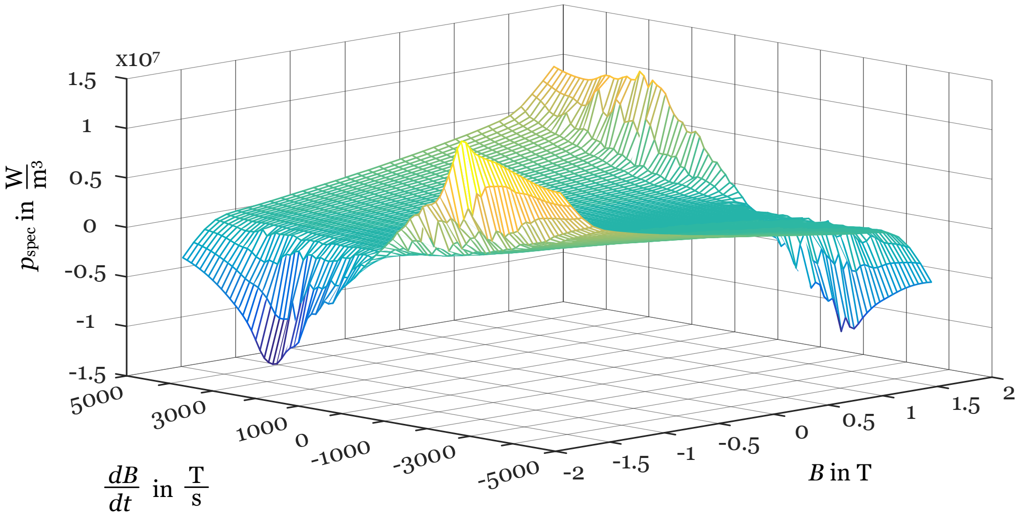

Figure 3.2: Exemplary loss-surface of an M250-35A toroidal iron sample, details are discussed in Appendix B.1.3.

Proposed Model

As proposed in [53], the instantaneous specific power losses p_{spec} can be calculated based on instantaneous magnetic field quantities,

$$p_{\text{spec}}(t) = H(t)\frac{dB(t)}{dt}, \tag{3.1}$$

where H is the magnetic field strength, and dB/dt is the rate of change in the magnetic flux density. The drawback of (3.1) is that B and H are interdependent, calling for elaborate time-dependent modeling, starting from the initial curve in the *BH*-plane, which is practically not feasible. To overcome this drawback, the specific power losses are modeled by

$$p_{\mathrm{spec}}(t) = f\left(B(t), \frac{dB(t)}{dt}\right), \tag{3.2}$$

where the flux density B and and its rate of change dB/dt are obtained from measuring the primary current and the secondary voltage of the specimen, i.e., Epstein frame or toroidal sample, respectively. From (3.1), the specific losses p_{spec} on the z-axis of the loss-surface, shown in Figure 3.2, can be related to the magnetic field strength H.

Loss-Surface Determination

The authors in [48–50] and the approach in this thesis use a triangularly shaped waveform of flux density in the material which is advantageous in the experimental determination of the loss-surface as the measured datapoints are distributed in the B-dB/dt plane as evenly as possible. Such a waveform allows for the obtainability of different values of B for a fixed value of $|dB/dt|$ for each of the investigated frequencies. The specific instantaneous power p_{spec} is obtained for every pair of magnetic flux B and its time derivative dB/dt. The magnetic flux density is obtained by Faraday's law of induction. To this aim, the secondary voltage of the used test specimen u_{sec} is integrated,

$$B(t) = \frac{1}{N_{\mathrm{sec}} S_{\mathrm{m}}} \int u_{\mathrm{sec}}\, dt, \tag{3.3}$$

where N_{sec} is the number of turns on the secondary winding and S_{m} is the cross-sectional area of the steel. The specific instantaneous iron losses p_{spec}, used to determine the loss-surface, can be calculated from (3.1)

$$p_{\mathrm{spec}}(t) = H(t)\frac{dB(t)}{dt} = \frac{N_{\mathrm{pri}}}{l_{\mathrm{m}}} i_{\mathrm{pri}}(t) \frac{1}{N_{\mathrm{sec}} S_{\mathrm{m}}} u_{\mathrm{sec}}(t), \tag{3.4}$$

where N_{pri} is the number of turns on the primary winding and l_{m} is the mean magnetic path length [53]. The measured quantities are the primary current i_{pri} and the secondary voltage u_{sec}. A detailed presentation of the test setup is provided in Appendix B.1.2.

To obtain the specific instantaneous iron losses for an arbitrary pair of B and dB/dt, a thin-plate spline algorithm [54] was chosen for interpolation between the measured data points of the loss-surface. Thereby, a smooth surface

$$S(\vec{x}) = \sum_{j=1}^{n} \lambda_j \|\vec{x} - \vec{x}_j\|^2 \log\|\vec{x} - \vec{x}_j\| + c_0 + c_1 x_1 + c_2 x_2, \ \vec{x} \in \mathbb{R}^2, \tag{3.5}$$

is obtained, where the vector $\vec{x}$ contains the flux density B and its time derivative dB/dt

$$\vec{x} = \begin{pmatrix} x_1 \\ x_2 \end{pmatrix} = \begin{pmatrix} B \\ \frac{dB}{dt} \end{pmatrix}, \tag{3.6}$$

and c_0-c_2 are coefficients for the thin-plate spline algorithm, to construct the actual loss-surface, obtained from the measured data. Details for obtaining these coefficients are given in [54].

3.1.2 Loss-Surface–Based Iron Loss Prediction

Toroidal Iron Stack

A toroidal ring setup was chosen for validation because of its simple magnetic circuit and notably its chosen iron stack cross-sectional area closely resembles that of FHP drives. The cross-sectional area of the ring, with about 3.9 mm in width and 5.3 mm in height has similar geometric dimensions as the cross-sectional areas of the drives to which the obtained results are applied. Further details are provided in Appendix B.1.3.

Iron Loss Determination

For a given measurement point, the mean iron loss density p_{fe} is determined by the mean value of the specific instantaneous losses $p_{\mathrm{spec}}(t)$ over one period T:

$$p_{\mathrm{fe}} = \frac{1}{T} \int_{t_0}^{t_0+T} p_{\mathrm{spec}}(t)\,\mathrm{d}t. \tag{3.7}$$

For any given combination $(B, dB/dt)$, the mean iron loss density can be obtained from the experimentally determined mean iron loss density, as per (3.7), and the thin-plate spline interpolation of (3.5).

3.1.3 Comparison of Iron Loss Measurements and Loss-Surface Prediction

The influence of the sample size and the samples' manufacturing on the determined loss-surface is ascertained as follows: Three different samples have been prepared. Samples "EP,w" and "EP,n" refer to Epstein frame samples with different widths, "wide" and "narrow," so as to investigate the influence of the cutting process. The third sample is a toroidal iron stack (index: ring), as described in Appendix B.1.3. Table 3.1 compares the computed mean iron loss densities $p_{\mathrm{EP,w}}$, $p_{\mathrm{EP,n}}$, and p_{ring}, predicted with the different previously measured corresponding loss-surfaces, and the directly measured reference loss density p_{meas} of the toroidal iron stack. $p_{\mathrm{EP,w}}$ and $p_{\mathrm{EP,n}}$ are the computed mean iron loss densities obtained from loss-surfaces based on Epstein frame samples with wide ($p_{\mathrm{EP,w}}$, width of the strips: 30 mm) and narrow ($p_{\mathrm{EP,n}}$, width of the strips: 5 mm) iron samples. p_{ring} is obtained from a loss-surface based on the toroidal iron stack. Two different waveforms, sinusoidal signals with an additional third harmonic component (30 % of the main amplitude, 180° and 0° phase shift for waveform I and II, respectively) with base frequencies of 50 and 200 Hz are chosen for evaluation. The errors e_{i} are computed from

$$e_{\mathrm{i}} = \left(\frac{p_{\mathrm{i}}}{p_{\mathrm{meas}}} - 1\right) \cdot 100\%, \text{ where i} = \text{EP,w; EP,n; ring.} \tag{3.8}$$

Figures 3.3 (a)-(b) show the example case waveforms of the flux density used for the analysis. Figures 3.3 (c)-(f) show the predicted instantaneous iron losses for the different loss-surfaces (Epstein frame ($p_{\mathrm{EP,w}}$, $p_{\mathrm{EP,n}}$) and toroidal specimen (p_{ring})). The predictions are compared to the measured instantaneous iron losses obtained from the toroidal specimen. The results show a certain immunity to change of frequency and waveform of the magnetic flux density. On the other hand, the samples' preparation (e.g., material degradation due to cutting, shown by the significant difference between wide and narrow Epstein samples in Figure 3.3), used to determine the respective loss-surfaces, has a significant impact.

Table 3.1: Comparison of measured and predicted mean iron loss densities for the toroidal sample as per Appendix B.1.3, based on three loss-surfaces determined from different samples.

Waveform	f_B	p_meas	$p_\mathrm{EP,w}$	$p_\mathrm{EP,n}$	p_ring	$e_\mathrm{EP,w}$	$e_\mathrm{EP,n}$	e_ring
–	Hz	$\frac{\mathrm{kW}}{\mathrm{m}^3}$	$\frac{\mathrm{kW}}{\mathrm{m}^3}$	$\frac{\mathrm{kW}}{\mathrm{m}^3}$	$\frac{\mathrm{kW}}{\mathrm{m}^3}$	%	%	%
I	50	15.66	14.17	17.53	16.10	-9.5	11.9	2.8
I	200	91.08	83.99	109.01	95.25	-7.8	19.7	4.6
II	50	16.82	15.67	19.47	17.50	-6.8	15.8	4.0
II	200	111.13	98.10	131.46	113.41	-11.7	18.3	2.1

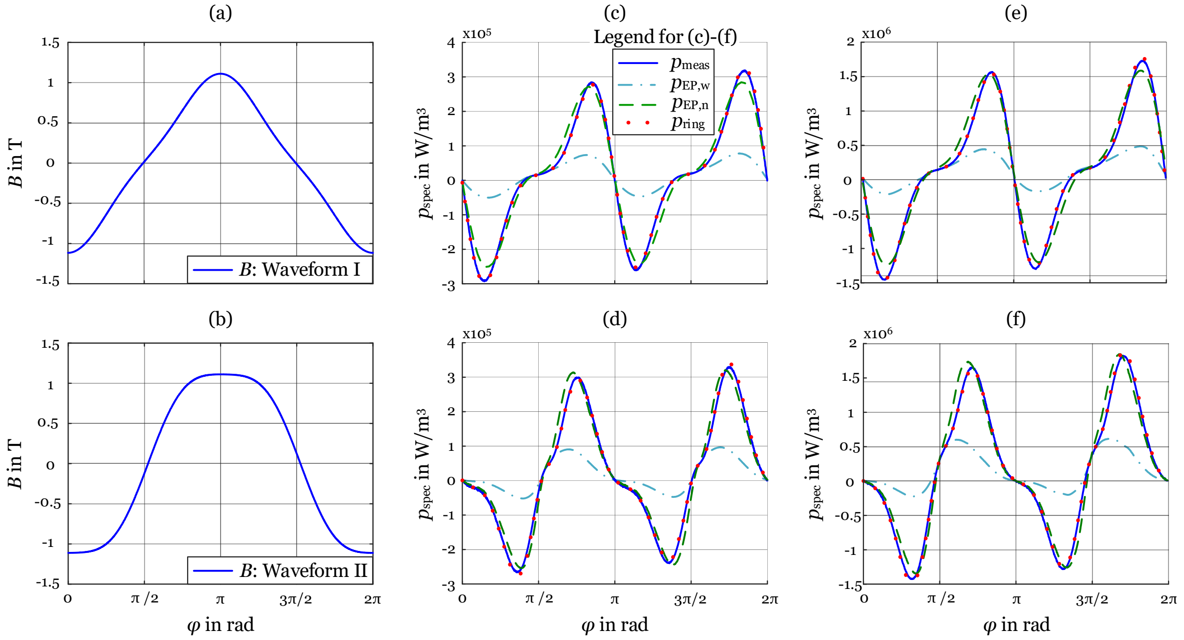

Figure 3.3: Waveforms of flux density (a)-(b), instantaneous losses for f=50 Hz (c)-(d), and for f=200 Hz (e)-(f) in the toroidal iron stack for the respective waveforms.

3.1.4 Example Case Study with the Example Case Drive

This case study is intended to demonstrate how the loss-surface approach can be applied for practical use. To this aim, the example case drive is investigated. The iron-loss results obtained with the loss-surface algorithm are compared with experimentally obtained data from measurements with a rheometer, as explained in [55].

Setup

For the case study, operating points from 2000 to 6000 rpm are chosen, since this speed range is common for automotive fan applications. The lamination sheets of the stator are glued together with Backlack® technology (indicated by "BL"), in the same way as are the sheets in the toroidal sample, upon which the loss-surface data is based. Experimental results for an example case drive's stator package with mechanical interlockings (indicated by "IL") are compared. The investigated stator packages are shown in Figure 3.4. In this example case study, no-load operation of the example case drive is investigated. Therefore, only permanent magnet induced iron losses are present.

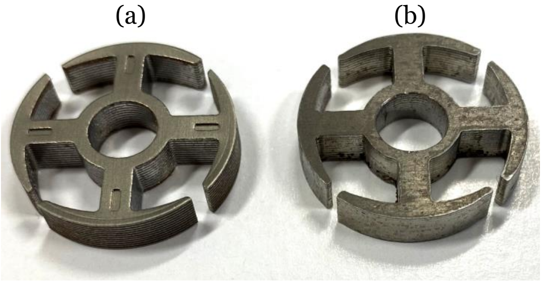

Figure 3.4: Photos of the example case drive's stator package with (a) laminations with mechanical interlockings, and (b) a lamination stack glued with Backlack® technology, as illustrated per [56].

Methodology

For computing iron losses, the flux density distribution in the iron volume of interest has to be determined. Figure 3.5(a) shows such a flux density distribution for an electrical rotor position of $\varphi_{\text{el}} = 0°$. The figure presents the flux density in the cross-sectional stator area of the example case drive.

The flux density at the stator tooth bottom is investigated. The exact position is indicated in Figure 3.5(a), and is chosen for investigation because, due to flux concentration, the largest flux density amplitudes in the stator iron volume are expected there. The numerically computed flux density within this area, B_{num}, is then presented in Figure 3.5(b).

Due to the rotation of the rotor, the flux density distribution in the cross-sectional stator area of the example case drive changes. Therefore, it is assumed that the course of flux density from Figure 3.5(b) is present in each infinitesimal volume element of the stator iron. This assumption allows for the application of:

$$P_{\text{fe}} = p_{\text{fe}} \cdot V_{\text{fe, stator}}. \tag{3.9}$$

P_{fe} are the absolute iron losses in W, p_{fe} is the mean iron loss density in W/m^3, and $V_{\text{fe, stator}}$ is the stator's iron volume in m^3.

When applied to the magnetic flux density with the stator iron, the loss-surface algorithm assigns to each pair of B and dB/dt specific iron losses p_{spec} in W/m^3, e.g., see Figure 3.3. With (3.7), the specific iron losses p_{fe} are determined.

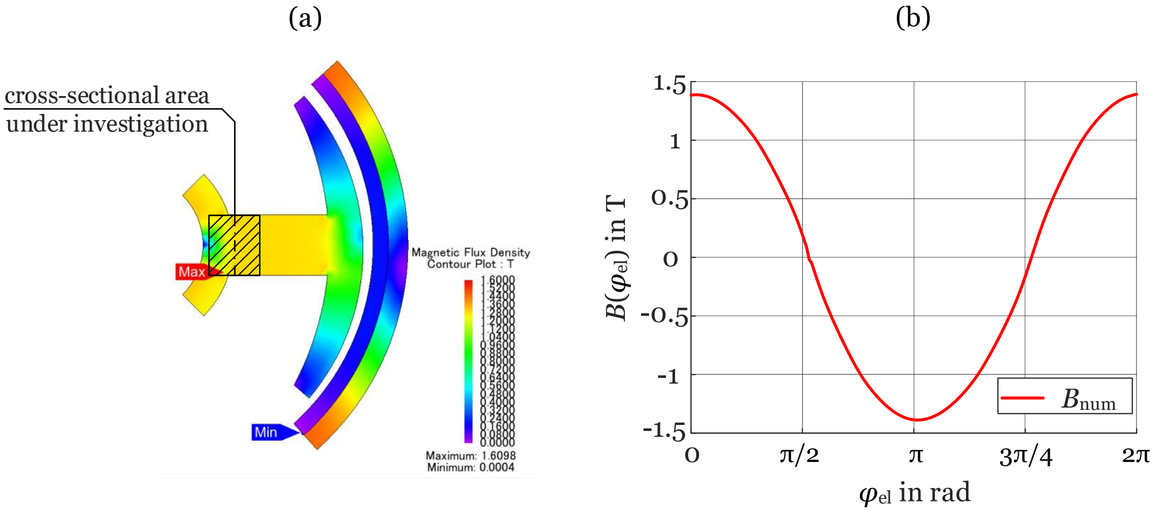
(a)

(b)

Figure 3.5: Analysis of the flux density at the bottom of the stator tooth with (a) sketch of the investigated cross-sectional area, and (b) computed average flux density in this area as it changes with the electrical rotor position φ_{el}.

Results

The results of the iron-loss investigations are presented in Figure 3.6 and Table 3.2. Five operating points with different rotor speeds are investigated, both, experimentally with precise rheometer measurements and theoretically by the loss-surface algorithm. The difference between these two approaches is below 5 %, which can be considered excellent in terms of iron-loss determination.

Table 2.4 in Section 2.2.3 provides an example case drive's iron loss computation based on the Steinmetz equation. For the rotor speed of 5000 rpm at no-load operation, the difference between the computation and experimental result is -20 %. With the loss-surface approach a difference of only 0.7 % can be achieved for this rotor speed. The difference between results from the loss-surface algorithm and experimental results, $e_{\text{LSS-i}}$, is determined by (3.10).

$$e_{\text{LSS-i}} = \left(\frac{P_{\text{fe,exper,i}}}{P_{\text{fe,LSS}}} - 1 \right) \cdot 100\%, \text{ where i} = \text{BL, IL} \tag{3.10}$$

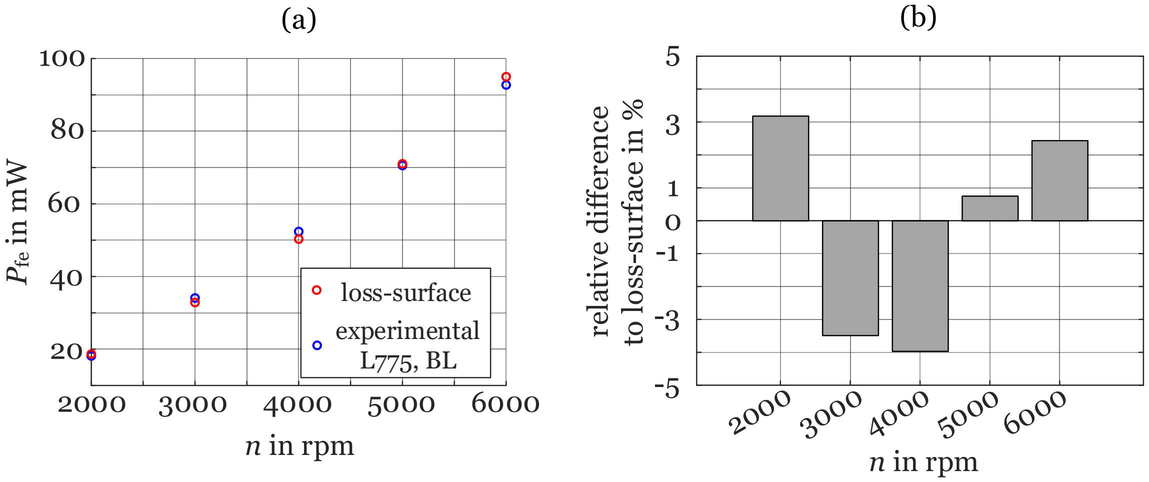

Figure 3.6: Experimental and loss-surface–based iron loss results of the example case drive's stator for the different rotor speeds at no-load operation with (a) absolute values of the iron losses, for both investigations and (b) relative difference between the experimental results to the loss-surface–based results.

Table 3.2: Comparison of experimental ($P_{\mathrm{fe,exper,BL}}$) and loss-surface–based mean iron losses ($P_{\mathrm{fe,LSS}}$) for the stator of the example case drive for different rotor speeds.

n	$P_{\mathrm{fe,LSS}}$	$P_{\mathrm{fe,exper,BL}}$	$e_{\mathrm{LSS\text{-}exper}}$
rpm	mW	mW	%
2000	18.1	18.7	3.3
3000	34.1	32.9	-3.5
4000	52.4	50.3	-4.0
5000	70.6	71.1	0.7
6000	92.7	95.0	2.5

Applicability of the findings

The applicability of the findings is analyzed by introducing further experimental results. Figure 3.7(a) shows these additional experimental results from another example case drive's stator package. The laminations of this additional package have been cut by mechanical punching and are stacked with mechanical interlockings. This analysis of different cutting and packaging techniques shall quantify how large the difference between a prototype (typically laser-cut and glued) and a series version (typically punched with interlockings), in terms of iron-losses, may be. Figure 3.7 and Table 3.3 extend the example case study's findings of Figure 3.6 and Table 3.2.

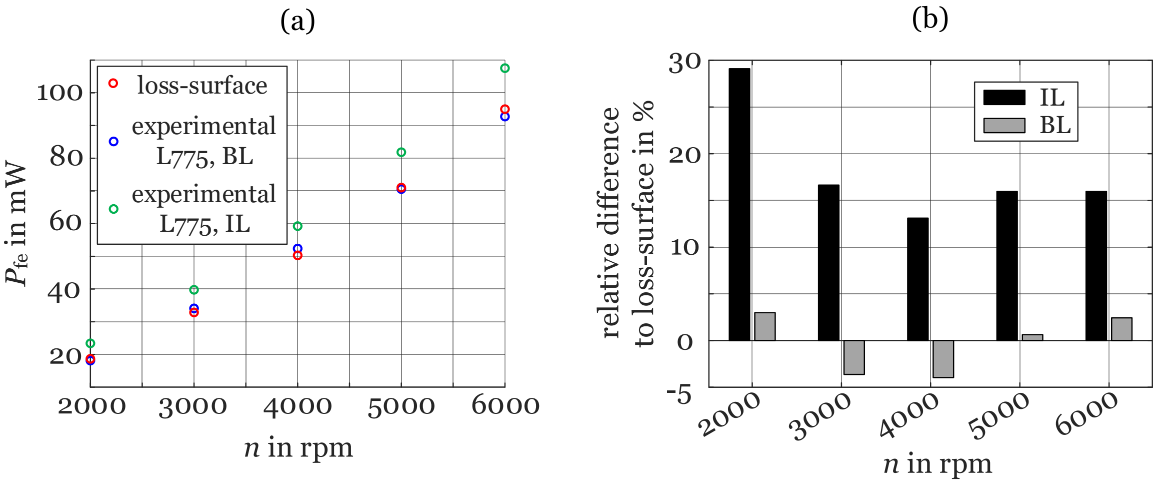

Figure 3.7: Experimental (BL and IL) and loss-surface–based iron loss results of the example case drive's stator for different rotor speeds at no-load operation with (a) absolute values and (b) relative differences between the experimental and the loss-surface–based results.

As expected, the measured iron losses for the IL stator package are larger. Beside the operating point at 2000 rpm, the difference to the loss-surface results for the speeds from 3000 to 6000 rpm is in constant range of +15±2 %.[1] As per [57, p. 452], correction factors between 1.7 and 2.5 apply to align iron loss computations with experimental results. Therefore, the difference of +15±2 % can still be considered as good.

Table 3.3: Comparison of measured ($P_{\mathrm{fe,exper,BL}}$ and $P_{\mathrm{fe,exper,IL}}$) and loss-surface–based mean iron losses ($P_{\mathrm{fe,LSS}}$) for the stator of the example case drive for different operating points with respect to rotor speed.

n	$P_{\mathrm{fe,LSS}}$	$P_{\mathrm{fe,exper,BL}}$	$e_{\mathrm{LSS\text{-}BL}}$	$P_{\mathrm{fe,exper,IL}}$	$e_{\mathrm{LSS\text{-}IL}}$
rpm	mW	mW	%	mW	%
2000	18.1	18.7	3.3	23.4	29.3
3000	34.1	32.9	-3.5	39.8	16.7
4000	52.4	50.3	-4	59.2	13
5000	70.6	71.1	0.7	81.8	15.9
6000	92.7	95.0	2.5	107.5	16

3.1.5 Summary Iron Loss Determination

The iron losses of FHP motors with arbitrary waveforms can be predicted from a previously determined iron loss-surface. The influences of material degradation due to cutting are considered implicitly. Iron loss determination by the loss-surface approach, as proposed here, can therefore improve the accuracy of the FHP drive design process.

Accuracy is best when the size and processing of the iron sample is similar to the later application. In addition to that, influences induced by temperature or mechanical stress could be considered. In a first case study, the difference e_{ring} between the losses computed from a ring-sample loss-surface and experimental data, was below 5 % (Table 3.1). In a second example case study, with the example case drive, the error between the iron losses determined with the loss-surface algorithm and experimental data determined from rheometer measurements was below 5 % again.

---

[1] The outlier for 2000 rpm can be explained by the weak data set of the loss-surface for lower flux density frequencies, see Appendix B.1.1.

Experimental results from an example case drive's series stator package (IL), shows constant +15±2 % larger iron losses compared to its prototype version (BL), as expected. These results provide an estimate of how large the difference between the iron losses of a prototype and a series version is.

3.2 Stray Paths

As mentioned in Section 2.2, stray paths directly influence how much of the fields generated by the magnets (permanent/electro) contribute to the torque production and thus also the machine's energy conversion efficiency.

This section summarizes the findings reported on in a master thesis [40], jointly developed with the author of this thesis. Here, no specific model is developed, but the application of well known design concepts from larger machines, to determine the different stray paths, is thoroughly investigated.

Figure 3.8 gives an overview of the classification of the stray paths used for the analysis that is further discussed in the following Sections 3.2.1 and 3.2.2. Leakage paths affecting the flux of the magnets on the one hand, and leakage paths affecting the flux generated by the currents in the coils on the other hand, are distinguished.

For the analysis, results obtained from 3D-FEA are compared with experimental results and will be discussed in this section. Details on the experimental investigations are provided in Appendix B.2. As per Section 2.2.2, 2D-FEA is not suitable because of these small machines' aspect ratios.

3.2.1 Permanent Magnet Related Stray Paths

Classification

Figure 3.9 shows the classification of the permanent magnet related flux paths. Investigated are the rotor leakage flux ϕ_{rl} and the stator leakage flux ϕ_{sl}, as shown in Figure 3.9(a), with the boxes in red. Figure 3.9(b) and Figure 3.10 indicate these fluxes in the cross-sectional area of the example case drive.

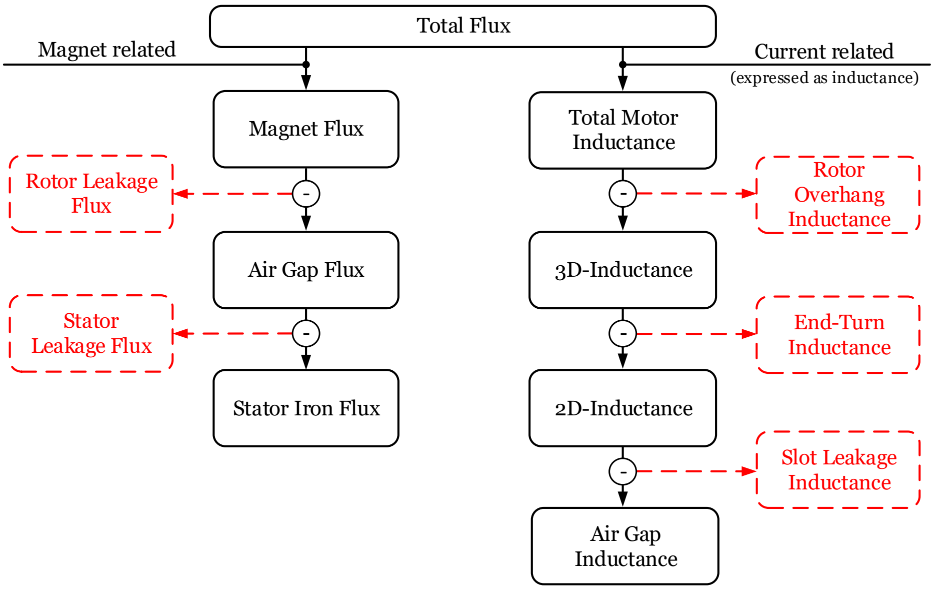
Total Flux
Magnet related
Current related
(expressed as inductance)
Magnet Flux
Rotor Leakage Flux
-
Air Gap Flux
Stator Leakage Flux
-
Stator Iron Flux
Total Motor Inductance
-
Rotor Overhang Inductance
3D-Inductance
-
End-Turn Inductance
2D-Inductance
-
Slot Leakage Inductance
Air Gap Inductance

Figure 3.8: Stray paths overview, for details on the permanent magnet related paths see Section 3.2.1, for details on the statorcurrent related paths see Section 3.2.2.

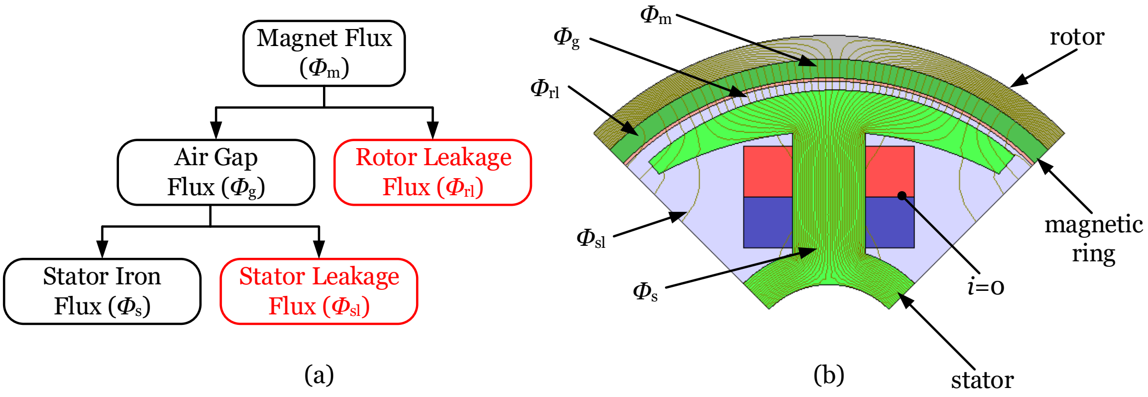
Magnet Flux (Φ_m)
Air Gap Flux (Φ_g)
Rotor Leakage Flux (Φ_{rl})
Stator Iron Flux (Φ_s)
Stator Leakage Flux (Φ_{sl})
Φ_m
Φ_g
Φ_{rl}
Φ_{sl}
Φ_s
rotor
magnetic ring
i=0
stator

(a) (b)

Figure 3.9: Flux distribution of the flux generated by the permanent magnets, illustrated as (a) block diagram and (b) magnetic flux lines visualized with a 3D-FEA model.

Determination

The magnet related stray paths are mainly investigated by the help of the FEA model, introduced in Section 2.2.2. Figure 3.10 shows how the magnet flux is separated. A magnetostatic analysis is conducted where the rotor position, in which the magnet's pole is directly located over the poleshoe, is chosen. In this position, the flux density in the stator tooth is at its maximum, which is considered the worst case for the occurrence of the stator leakage. The FE software allows for the straightforward determination of the different fluxes. To this aim, surfaces are identified through which the fluxes are measured. These surfaces are highlighted in Figure 3.10 and indicated as the flux permeating the magnet surface ϕ_{m}, the flux permeating the poleshoe surface ϕ_{g}, and the flux permeating the cross-sectional area on the stator tooth bottom ϕ_{s}. Since the investigated example case drive also has a non-zero rotor overhang (see Figure 2.2), axial flux must be considered and hence the end surfaces of the rotor and the stator are included in the calculation. The flux distribution is directly determined in the 3D-FEA software, the results are presented in Figure 3.11.

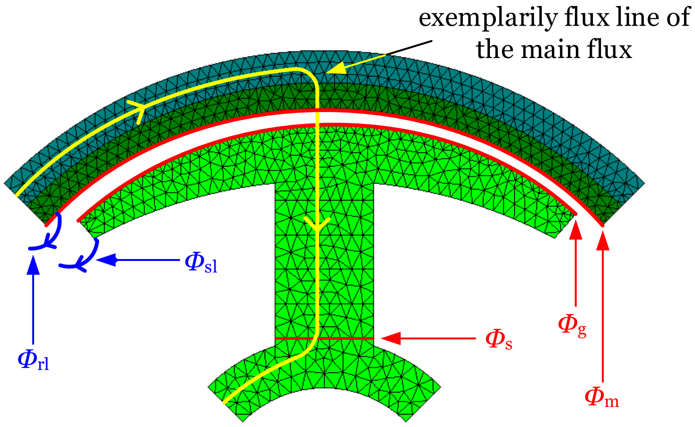

Figure 3.10: FE model of the example case drive showing the areas for the computation of the different flux components, the paths of the main and the two leakage fluxes.

Results

The flux components as determined from the FE computations are shown in Figure 3.11. For this no-load condition, 89.3 % of the magnet's flux links with the coil and hence is available for torque production. This finding is slightly larger than the range stated in Hanselman [23, p. 72] according to which the leakage flux ranges between 0 % and 10 % with respect to the magnet flux ϕ_{m}, for surface mounted magnets.

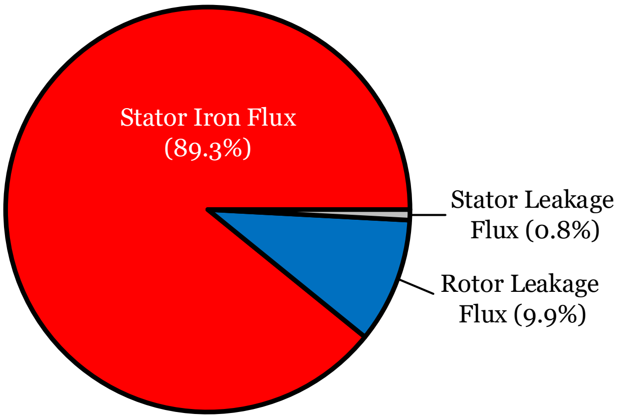
(a)

(b)

Flux Path	Symbol	Value	Share
-	-	µVs	%
Magnet Flux	Φ_{m}	15.53	100
Rotor Leakage Flux	Φ_{rl}	1.54	9.9
Airgap Flux	Φ_{g}	13.99	90.1
Stator Leakage Flux	Φ_{sl}	0.12	0.8
Stator Iron Flux	Φ_{s}	13.87	89.3

Figure 3.11: Magnet flux separation of the example case drive, (a) graphical representation as pie chart and (b) corresponding data with absolute and relative values.

3.2.2 Current Related Stray Paths

Classification

To model the stray paths related to the flux generated by the current through the coils, different inductances are distinguished from one another, as shown in Figure 3.12. Together they form the total motor inductance L_{s}.

Determination

The total motor inductance is determined from the time constant τ of an RL-network, see Figure 3.13. At standstill, a BLDC motor's electric equivalent circuit resembles such a network, see Figure 1.8. A rectangular voltage is applied to one winding while the other is left floating. Two rotor positions were chosen for minimum/maximum flux density in the stator tooth, respectively, because the permeabilities of the cores

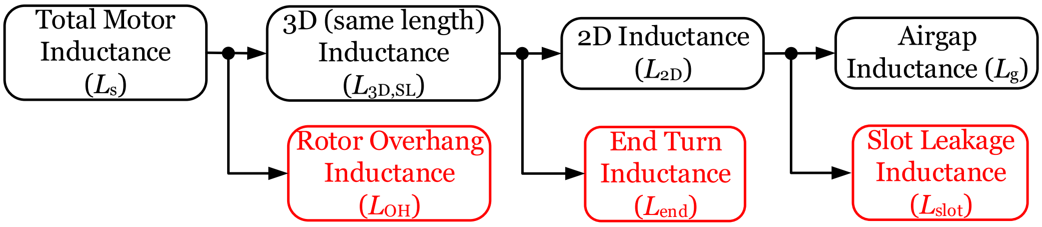
Total Motor Inductance (L_s)
3D (same length) Inductance ($L_\mathrm{3D,SL}$)
2D Inductance (L_2D)
Airgap Inductance (L_g)
Rotor Overhang Inductance (L_OH)
End Turn Inductance (L_end)
Slot Leakage Inductance (L_slot)

Figure 3.12: Flux distribution of the flux generated by the current through the coil, expressed in the form of inductances.

depend on the flux density, see Figure 2.5 in Section 2.1. At 3 and at 48 mechanical degrees, the flux density in the stator tooth reaches its minimum/maximum, respectively.[2] Figure 3.14 depicts the flux density distribution in the example case drive's cross-sectional area at these rotor positions.

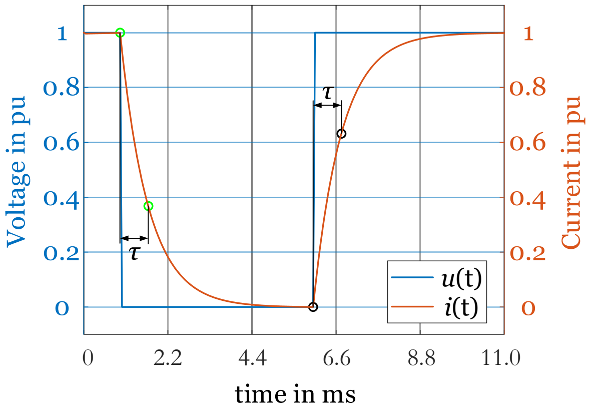

Figure 3.13: Current following the application of a voltage step to the example case motor. The motor inductance is determined from the time constant $\tau = \frac{L}{R} \implies L = \tau R$, where τ is the time between turn-on and 63 % of the maximum current, as indicated.

The time constant is determined both through 3D-FEA and experimentally. The rectangular voltage signal's amplitude and frequency are chosen to obtain a current amplitude similar to the example case drive's rated current. The experimental investigations provided the same results. They are reported on in Appendix B.2. From

---

[2] These positions differ from 0 and 45 mechanical degrees, respectively, because of the asymmetric airgap. The difference has been determined experimentally.

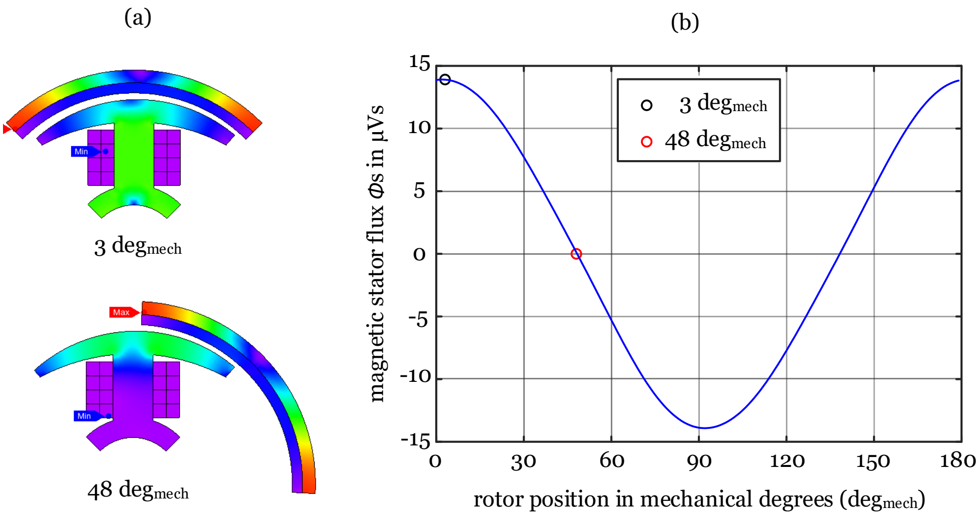

Figure 3.14: 3D-FEM (a) simulated flux density distributions and (b) computed stator flux in the stator core, as a function of the rotor position.

the main inductance, the different inductances are determined through additional 3D-FEA as follows:

- Rotor Overhang Inductance L_{OH}
  This inductance is determined by comparing two 3D-FEA models, one with rotor overhang, one without, where the difference in inductance provides L_{OH}. The two models have been shown in Figure 2.2(a) and (b) in Section 2.1.

- End Turn Inductance L_{end}
  To determine the end turn inductance, the 3D-FEA model without rotor overhang (Figure 2.2(b)) is compared with a 2D-FEA model which is extended into the axial direction by the length of the stator core. The difference in inductance between these two models provides L_{end}.

- Slot Leakage Inductance L_{slot}
  L_{slot} is determined as the difference between the airgap inductance L_{g} and the total motor inductance of the 2D-FEA model. The airgap inductance is computed by $L_{\mathrm{g}} = 2pN\frac{\phi_{\mathrm{g}}}{I}$, where $2p$ is the number of poles, N is the number of turns per coil, ϕ_{g} is the computed airgap flux, and I is the corresponding coil current.

Results

Figure 3.15 shows the results of this inductance investigation. Compared to the 10.7 % magnet related leakage paths, the share of leakage inductances is, with 52 % in total, much larger. This is explained by the large aspect ratios, i.e., rotor overhang and end windings of approximately the same length as the stator core, see, e.g., Figure 2.2(a) and (b) (Section 2.1).

(a)

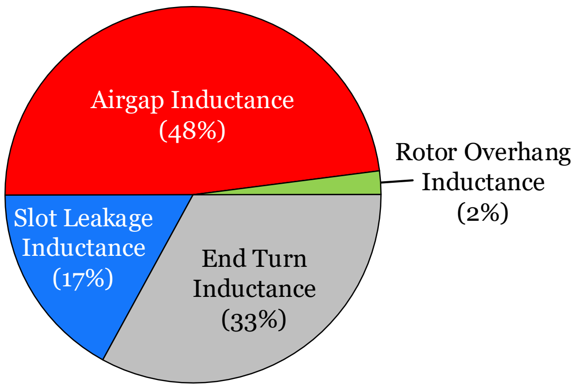

(b)

Inductance	Symbol	Value	Share
-	-	mH	%
Airgap Inductance	L_{g}	2.6	48
Slot Leakage Inductance	L_{slot}	0.9	17
End Turn Inductance	L_{end}	1.8	33
Rotor Overhang Inductance	L_{OH}	0.1	2
Total Motor Inductance	L_{s}	5.4	100

Figure 3.15: Inductance separation of the example case drive, (a) graphical representation as pie chart and (b) corresponding data with absolute and relative values.

3.2.3 Summary Stray Paths

With approximately a 10 % and 50 % share of leakage, respectively, only roughly 90 % and 50 %, respectively, of the flux generated by the magnets or the winding contributes to the torque development of the motor. These orders of magnitude will not change with rather small design changes.

For magnet related leakage, Hanselman [23, p. 72] states a share between 0 % and 10 % for PM motor topologies with surface mounted magnets. This reference from the literature has been confirmed with the investigations in this section.

The winding present with the example case drive suggests a significant share of end turn inductance. With 33 %, this significant share has been confirmed. Therefore, the end turn inductance has the largest influence on the current related stray paths.

In the frame of the master thesis [40], mentioned at the beginning of this section, the FE model of the example case drive has been enhanced with respect to the materials' magnetization, considering material degradation due to cutting, and enhancing the modeling of the bifilar winding. Details for these enhancements are provided in Section 2.1.

Chapter 4

Computer Aided System Optimization

This chapter presents optimization methodologies for solving the inverse problem of FHP drives for pump and fan applications system design. First, a survey of the basics of optimization, with the selection of an appropriate optimization methodology is given. The application of this optimization methodology to the models in use, forming a multiphysical system, is presented subsequently. Then, the utilization of surrogate models is discussed. The chapter concludes with a specific application of space mapping to the drives of interest.

4.1 Statement of the Problem

For a long time, scientists have desired to model the world to foresee the behavior of a certain system. This process of stating causes and calculating the respective effects is called forward problem. With design tasks, often the opposite approach is required, the inverse problem. For certain requirements given, an application fulfilling these requirements has to be identified. Tight requirements in automotive applications require not only the consideration of the electric motor design, but also, e.g., of power electronics and the mechanical systems. With the advent of modern power-electronics based variable speed drives, the degrees of freedom of a certain design problem, and thus the dimensionality of the problem have increased. This chapter suggests a framework for the analysis to eventually identify the best suited drive for a certain set of requirements within a reasonable time.

4.2 Choice of an Optimization Methodology

This subsection presents a short review on common optimization methodologies. Such optimization methodologies are utilized for investigating an objective function $f(x)$ for the global minimum or maximum. This is necessary for answering the question of what might be the best solution for a problem, if the requirements were submitted to $f^{-1}(x)$. Properties of the optimization methodologies and of the objective function are discussed to find an optimization methodology for the design of FHP drives for pump and fan applications. The following discussion is based on [58,59].

4.2.1 Gradient-Based Optimization

Gradient-based algorithms are mathematical methods to identify the global minimum or maximum of an objective function $f(x)$. The algorithms identify the slope $f'(x)$ and proceed into this direction, as illustrated in Figure 4.1. It is not necessary to compute $f(x)$, but important to know the first order derivative $f'(x)$. The algorithm's stepsize can be determined by the coefficient α, where $x_{\text{new}} \leftarrow x_{\text{old}} + \alpha f'(x_{\text{old}})$, i.e., the new position x_{new} is determined from the old position x_{new} and the product of α and $f'(x_{\text{old}})$. The choice of α significantly influences the performance of the algorithm: 1) If α is too small, the algorithm might find a local minimum or maximum, or 2) if α is too large, the algorithm might overshoot minimum or maximum positions and therefore might require longer to converge. Approaches exist, e.g., Newton's Method, in which the algorithms' speed is adjusted when the algorithm approaches minimum or maximum positions by: $x \leftarrow x - \alpha \frac{f'(x)}{f''(x)}$. This approach requires a second order derivative $f''(x)$. For multi-dimensional optimization problems, the second order derivative $f''(x)$ becomes a so-called Hessian matrix $\mathbf{H}_{\text{f}}$, which is not straightforward to determine. Newton's Method would require a division by this matrix, which requires the matrix to be invertible.

4.2.2 Stochastic Optimization

At large, stochastic optimization refers to certain techniques to identify optimal solutions by employing randomness. The ideas for stochastic optimization come from observations in nature. Examples for this observations are, the evolutionary

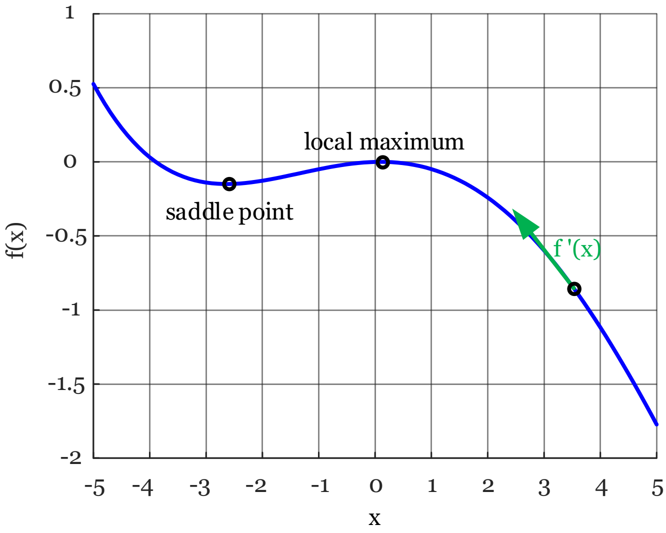

Figure 4.1: Arbitrary example function to illustrate the principle approach and challenges of gradient-based optimization.

behavior of nature as present in Evolution Strategies [60] and Genetic Algorithms [61, 62], the analogy of the cooling of fluids as present in Simulated Annealing [63], and the imitation of the social behavior of a bird flock or of a school of fish as present in Particle Swarm Optimization [64].

Similar to gradient-based optimization, stochastic optimization works iteratively, as presented in the following pseudo-code:

```
$f(x) \leftarrow$ initial parameter $x$
while $f(x)$ is the ideal solution or out of time do
    $f_t(x) \leftarrow$ Tweak($f(x)$)
    if Quality($f_t(x)$) > Quality($f(x)$) then
        $f(x) \leftarrow f_t(x)$
    end if
end while
return $f(x)$.
```

The algorithm tests the quality of new candidate solutions in the region of the current candidate. Candidate solutions with higher quality are adopted, candidates with lower quality are discarded. In contrast to gradient-based optimization, this approach does not require the computation of $f'(x)$. Only the existence of $f(x)$ is required. This enables the algorithm to investigate black-box like systems, where $f'(x)$ may be unknown.

4.2.3 Optimization Technique Selection

The required optimization algorithm has to find the region of the global optimum with high probability, and must be stable in convergence. The optimization algorithm also has to be capable of handling models of different mathematical origins. Such model variety is present when multiphysical optimization within reasonable time is required. An example for such variety is the multiphysical model, presented in Section 4.3, the analytic and the FE model, presented in Section 2.2, and a surrogate model, presented in Section 4.4.

The existence of an invertible Hessian matrix $\mathbf{H}_\mathrm{f}$, required for multi-objective gradient-based optimization, cannot be guaranteed for all the models described above. Therefore, stochastic optimization is chosen for the investigated optimization tasks in this thesis. The NSGA-II[1] genetic algorithm [65] is adopted for further utilization due to its robustness. The algorithm is built into the SyMSpace® simulation and optimization environment described in Section 1.2.3.

4.2.4 Employing the Optimization Methodology to the Models

Employing the selected theoretical optimization methodology to the models in use is implemented as shown in Figure 4.2. The different models in use are assembled with SyMSpace®, the built-in optimizer therefore has access to all models. The models are either directly implemented in SyMSpace®, or interfaced via Python® scripts. Information can therefore be exchanged in between all models in use.

It is possible to compute the models in parallel to increase the speed of the optimization process.

The used NSGA-II optimization algorithm is implemented in this optimizer. The settings for the optimization algorithm, i.e., population size, archive size, crossover probability, mutation probability, etc., can be adjusted. The optimization process can be live monitored, i.e., with visualization of the Pareto-front, metrics for convergence, or statistics of the objectives.

Eventually, the export of CAD data of the final design(s) is possible.

---

[1] Non-Dominated Sorting Genetic Algorithm-II

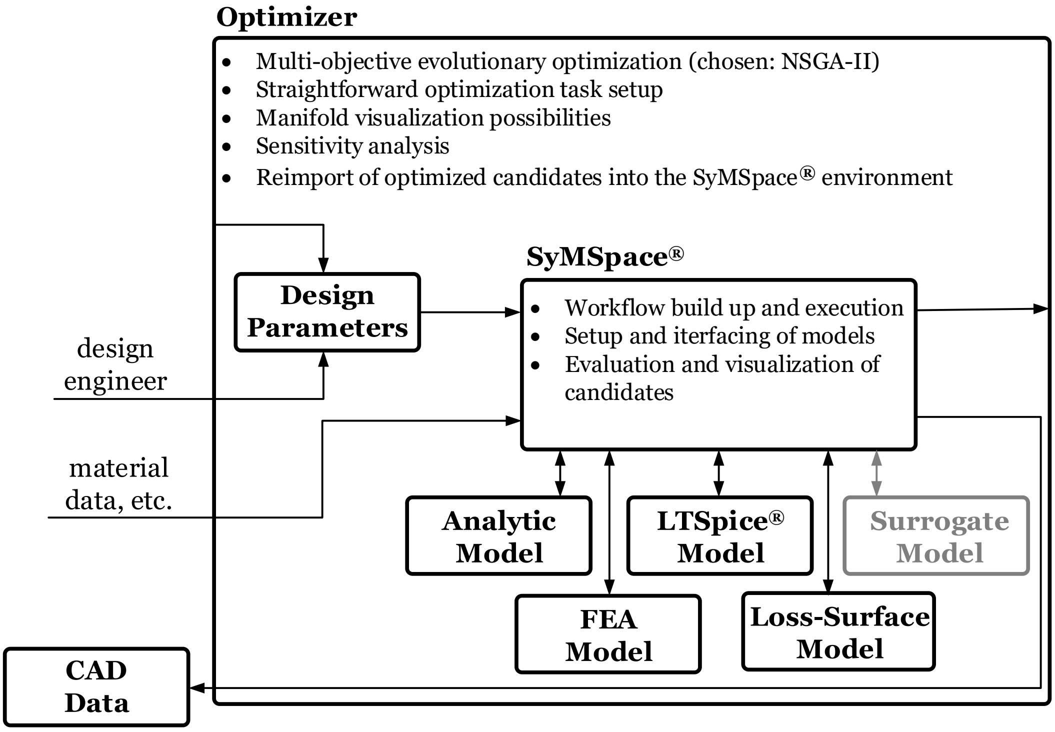
Optimizer
Multi-objective evolutionary optimization (chosen: NSGA-II)
Straightforward optimization task setup
Manifold visualization possibilities
Sensitivity analysis
Reimport of optimized candidates into the SyMSpace® environment
Design Parameters
SyMSpace®
Workflow build up and execution
Setup and iterfacing of models
Evaluation and visualization of candidates
design engineer
material data, etc.
Analytic Model
LTSpice® Model
Surrogate Model
FEA Model
Loss-Surface Model
CAD Data

Figure 4.2: Block diagram on how the different models in use are assembled via SyMSpace® to enable automated optimization with the superior optimizer and eventually export CAD data of the final design.

4.3 Multiphysical System Modeling

Pump and fan applications are mechatronic systems, in which the electromagnetic, electronic, and mechanical systems need to be considered. The isolated consideration of these disciplines leads to optimal sub-components which might be detrimental for the overall system performance. Hence, this thesis suggests comprehensive system optimization, elaborated on in the following.

4.3.1 Setup

The system modeling of the example case drive is shown in Figure 4.3 as a block diagram. Modeling of the electronic and mechanical system is implemented in LTSpice®. The electromagnetic system is considered via an FE model.[2] From that FE model, flux linkage and cogging torque are exported to the model in LTSpice®.

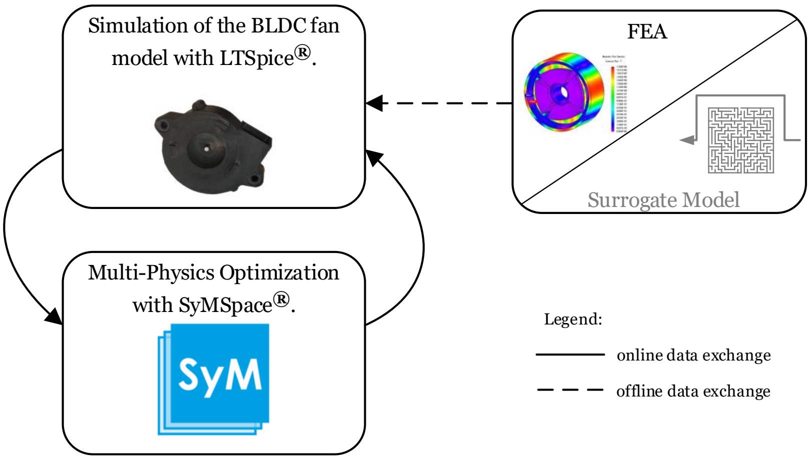
Simulation of the BLDC fan model with LTSpice®.
FEA
Surrogate Model
Multi-Physics Optimization with SyMSpace®.
SyM
Legend:
online data exchange
offline data exchange

Figure 4.3: Block-diagram of the multi-physics optimization setup.

Figure 4.4 shows details of this LTSpice® model. Boxes colored in black are directly modeled in LTSpice®, boxes in green are lookup-tables with data imported from the FE model, and the orange box is a simple load characteristic for a fan, with $P_{\text{fan}} \propto n^3$.

For solving the differential equations of the blocks in Figure 4.4, the numerical SPICE® solver is used. This solver can be considered stable in convergence, and it provides reliable results. The solver is straightforward to interface and therefore integrates well in the SyMSpace® environment.

---

[2] The surrogate model also mentioned in this block is designated for substituting for the FE model. More information on this surrogate modeling approach is reported on in Section 4.4.

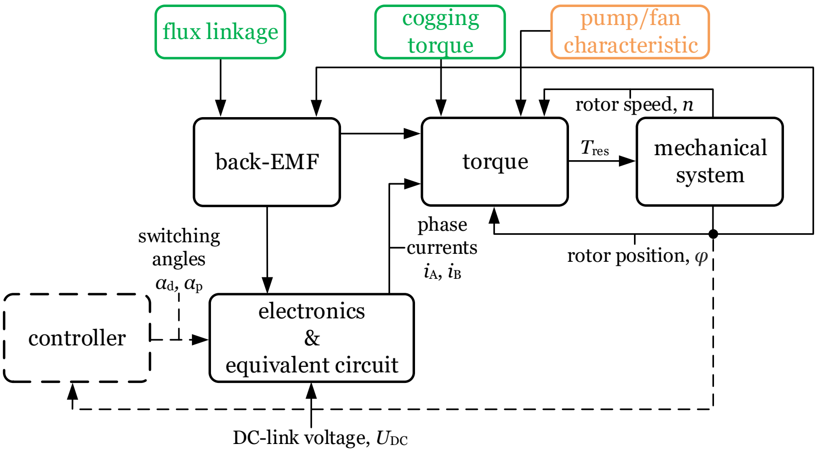
flux linkage
cogging torque
pump/fan characteristic
rotor speed, n
back-EMF
torque
T_{res}
mechanical system
switching angles α_{d}, α_{p}
phase currents i_{A}, i_{B}
rotor position, φ
controller
electronics & equivalent circuit
DC-link voltage, U_{DC}

Figure 4.4: Block diagram of the multiphysical system setup as implemented in LTSpice®.

4.3.2 Example Case Study: Switching Angle Optimization for a BLDC Switching Strategy

This example case study is provided to enhance the system model setup description in Section 4.3 with application oriented results. The authors' experimental investigations reported on in [32] are re-evaluated with respect to the application of an optimization algorithm. The setup shown in Figure 4.4 is used. The optimal switching angles are again determined, however, while the optimization in [32] was based on an experimental trial and error approach, stochastic optimization of optimal switching angles is utilized in the following.

Optimization goal

Figure 4.5 reviews experimentally determined phase currents of the example case drive. Comparing Figures 4.5(a) and (b), the phase currents become more rectangularly shaped by the additional delay of the turn-on angle α_{d}, and the peaks at the beginning and at the end of the conduction period are reduced. For each operating point, an optimum combination of α_{p} and α_{d} can be achieved. This results in a smoother output torque and, notably due to the reduction of the current peaks, lower I^2R losses in the winding.[3]

---

[3] Commonly, current control with PWM is utilized for current shaping.

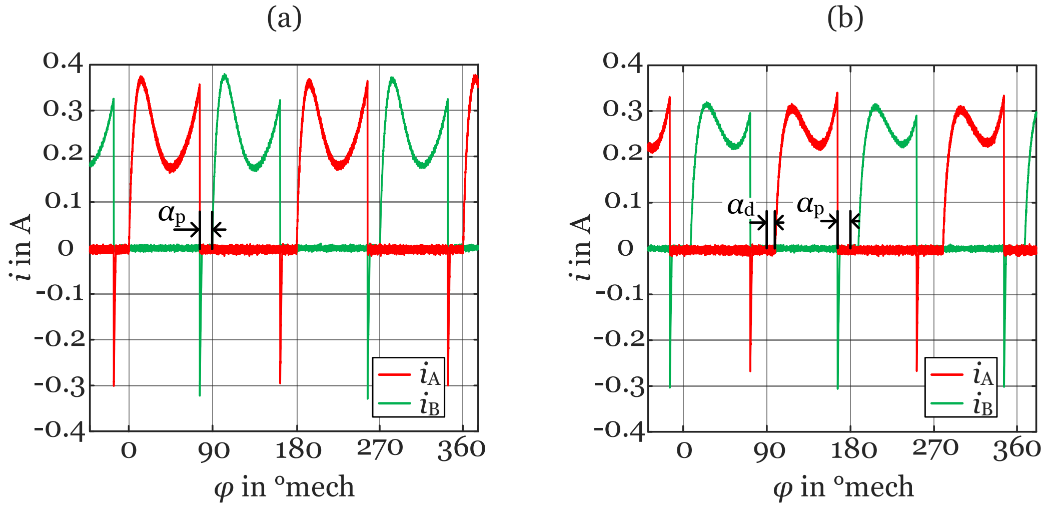

Figure 4.5: Measured phase currents without and with delay of the turn-on angle α_d, reported on in [32].

Methodology

The optimization workflow is realized with the SyMSpace® optimizer, presented in Section 4.2.4, and illustrated in Figure 4.6. The optimization algorithm changes the switching angles α_d and α_p to identify the minimum input power consumption at constant load.[4] For the experiments, U_{DC} is variable and can be adjusted to maintain constant rotor speed, since no auxiliary speed controller is used. The input power consumption P_{in} is evaluated.

T_{res} is the result of the torque balance, as shown in Figure 4.4. Keeping T_{res} close to zero results in a steady state of the mechanical system. With this steady state, mechanical speed, and hence the load, remain constant.

As with the experimental trial-and-error based investigations of [32], a range of rotor speeds, commonly used for such fan applications, from 3000 to 8000 rpm, with steps of 1000 rpm, is investigated.

The model of the drive had been validated by measurements exemplarily for an operating point of 5000 rpm. As per Figure 4.7, the model represents the measured behavior very well.

---

[4] 27.4 million different individuals are possible. That results from a resolution of the angles of 0.1 mechanical degrees within a range from 2 to 20 mechanical degrees for α_p and from 0 to 15 mechanical degrees for α_d, and 10 mV resolution for the voltage U_{DC} within a range from 5 to 15 V.

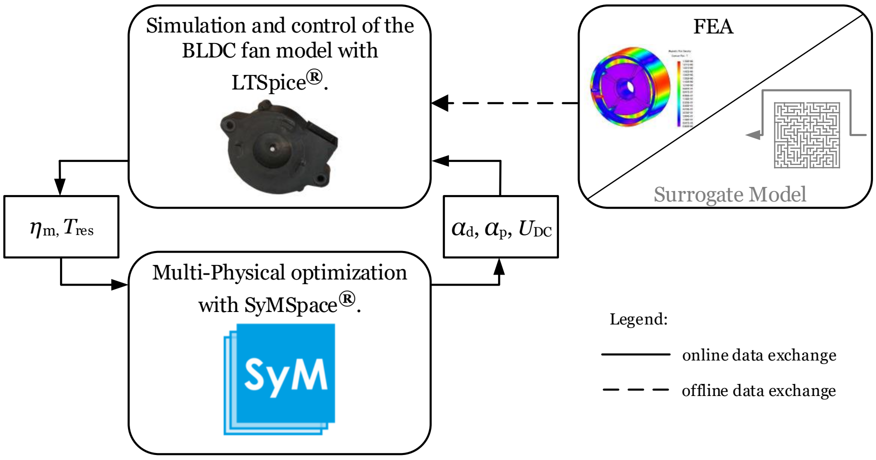
Simulation and control of the BLDC fan model with LTSpice®.
FEA
Surrogate Model
η_{m}, T_{res}
α_{d}, α_{p}, U_{DC}
Multi-Physical optimization with SyMSpace®.
SyM
Legend:
online data exchange
offline data exchange

Figure 4.6: Optimization methodology, with a refined sketch of Figure 4.3.

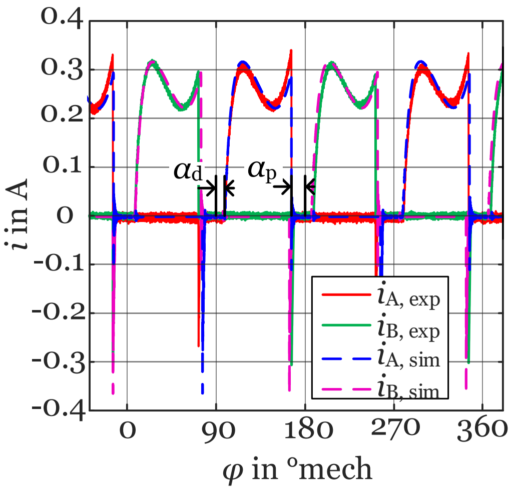

Figure 4.7: Comparison of the phase currents, measured as reported in [66] and simulated (Figure 4.4), of the example case drive, for an operating point of 5000 rpm.

Results

Optimization tasks were run for rotor speeds from 3000 to 8000 rpm, as previously mentioned. Figure 4.8 shows some results for the rated speed of 5000 rpm; the results for the whole investigated speed range are presented in Table 4.1.

Figure 4.8(b) illustrates the input power distribution for 4 optimal candidate solutions (PS2-PS5) and 1 non-optimal candidate solution (PS1).[5] The non-optimal candidate solution is shown to illustrate the worst case in terms of motor efficiency.

PS2-PS5 lead to similar input power distributions. The non-optimal PS1 reveals a slightly lower motor efficiency. The difference in α_d and α_p between PS1 and PS2-5 is significant. Conversely, only a small difference is shown in terms of motor efficiency. The results therefore exhibit a low sensitivity between the change of switching angles and input power distribution. U_DC for PS1 is 7.2 V and 7.7 V for PS2-PS5.

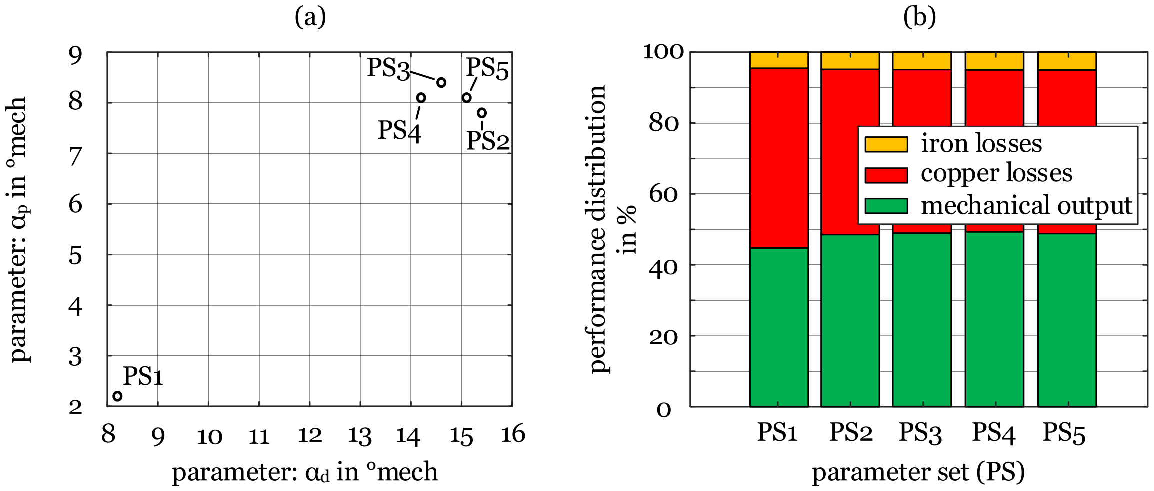

Figure 4.8: Result of an optimization run for the example case drive's rated speed of 5000 rpm (a) showing optimal candidate solutions PS2-PS5, and a non-optimal candidate solution PS1, and (b) the corresponding performance distribution[6].

---

[5] PS refers to a parameter set. A PS consists of α_d, α_p, and U_DC, see Figure 4.6. Since only the comparison of α_d and α_p between experimental results, as reported on in [32], and simulation is of interest, U_DC is not provided.

[6] The green bars all indicate the same output power given by the load of the fan at the given speed.

Table 4.1 depicts the investigated range of rotor speed, comparing between experimental results, as reported on in [32], and the simulation. The input powers differ by 10 % at maximum. The optimal angles found by the optimization algorithm differ significantly in comparison to the experimental results obtained with a trial-and-error approach.

Table 4.1: Experimental and simulated results for optimum turn-off and turn-on angles of α_p and α_d at different speeds n.

	experimental			simulation			
n	$\alpha_\text{p,opt}$	$\alpha_\text{d,opt}$	P_in	$\alpha_\text{p,opt}$	$\alpha_\text{d,opt}$	P_in	ΔP_in
rpm	$^\circ_\text{mech}$	$^\circ_\text{mech}$	W	$^\circ_\text{mech}$	$^\circ_\text{mech}$	W	%
3000	12.6	13	0.34	8.3	11.3	0.34	0
4000	14.5	10.2	0.78	21.3	15.4	0.8	2.6
5000	15.9	7	1.47	8.4	14.6	1.4	-4.8
6000	17.5	5.2	2.47	15.2	0.4	2.5	1.2
7000	19.4	2.8	4.19	24.1	10.3	3.9	-6.9
8000	20.3	0.4	6.95	10.9	11.8	6.3	-9.4

4.4 Surrogate Modeling

4.4.1 Overview

In the case of modeling of FHP drives, the need for using computationally expensive models has been shown in Section 3.2. Surrogate models use a black-box like approach. Stochastic optimization with a genetic algorithm is a suitable method to submit such models to. Therefore, design approaches based on surrogate modeling have gained attention as they bridge the gap between analytic and numerical approaches in manifold engineering disciplines [67–70], with the aim of making optimization possible. Examples of such surrogate modeling approaches are kriging, response surface, space mapping, and artificial neural networks [71–73]. The setup of these models requires some training, and the models are then valid for a certain parameter space and topology, as it may be given by a certain FHP drive. Of all approximation based approaches above, space mapping was chosen for further investigations for the following two reasons:

1. Space mapping requires a coarse and a fine model, which come with different computational effort and accuracy. For modeling (FHP) PM motors, this setup is possible to achieve and

2. in addition to the evaluation time of the coarse model, only algebraic operations are necessary to obtain an output with reasonable accuracy. Therefore, the computation time drops significantly, allowing for evolutionary optimization algorithms.

First, the space mapping theory of the approach is presented, then, the application of space mapping for modeling the example case FHP drive is outlined exemplarily.

4.4.2 Investigated Space Mapping Approach

Invented in 1994, in the field of microwave applications [74], the approach has proven to be successful in many engineering disciplines, e.g., [67–70, 75–77].

Principle Idea

Space mapping is a derivation of surrogate models [78]. A basic graphical representation of this idea is shown in Figure 4.9. An arbitrarily chosen polynomial function represents the response of a real world application for a certain input parameter. Exact information on the system can only be obtained at some points (denoted as red circles) which have been determined with time-consuming evaluation methods, e.g., 3D-FEA. To obtain information on the system response on the full parameter space within a reasonable time, a suitable approximation must be determined, as depicted with the dashed green line in Figure 4.9.

As depicted in Figure 4.10, the utilization of this space mapping approach is twofold:

1. The fine model generates a validation space from which exact data can be obtained and used, e.g., in the multiphysical model presented in Section 4.3 and

2. the aligned coarse model enables otherwise time-consuming models to be submitted to global optimization, with the genetic algorithm presented in Section 4.2.2.

With typical engineering applications, as with the example case drive of this thesis, multiple input variables are used and varied. This is sketched in Figure 4.10, where the multiple variables are summarized as vectors $\vec{\varphi}_f$ and $\vec{\varphi}_c$. $\vec{\varphi}_f$ is the input vector for the fine model and $\vec{\varphi}_c$ is the input vector for the coarse model, consisting of the variables shown in Table 2.1 in Section 2.2.1.

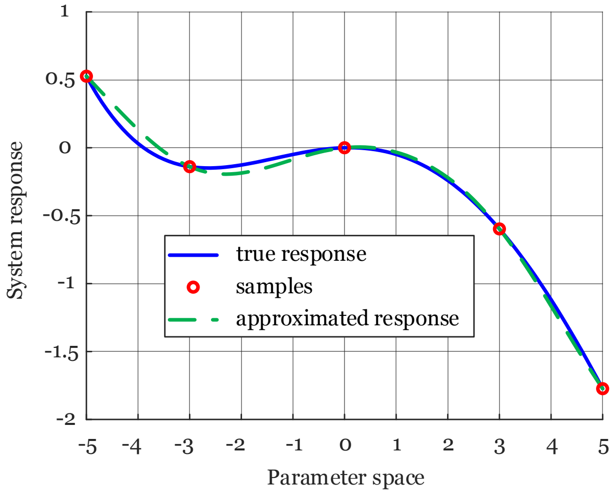

Figure 4.9: Sketch of the idea of a surrogate model.

The identification of a suitable transformation (4.1) between a coarse and a fine model, with the constraint that (4.2) holds for each of the base points is the main challenge of space mapping.

$$\vec{\varphi}_{\mathrm{c}} = \mathbf{P}(\vec{\varphi}_{\mathrm{f}}) \tag{4.1}$$

$$||\vec{R}_{\mathrm{f}}(\vec{\varphi}_{\mathrm{f}}) - \vec{R}_{\mathrm{c}}(\vec{\varphi}_{\mathrm{c}})|| \leq \epsilon \tag{4.2}$$

P is a predefined and desirable invertible transformation, $\vec{R}_{\mathrm{f}}(\vec{\varphi}_{\mathrm{f}})$ is the fine model response for a parameter set $\vec{\varphi}_{\mathrm{f}}$, $\vec{R}_{\mathrm{c}}(\vec{\varphi}_{\mathrm{c}})$ is the coarse model response for a parameter set $\vec{\varphi}_{\mathrm{c}}$, and ϵ a small positive constant.

In other words, it is desirable, that the model responses provide almost equal results while the input vectors $\vec{\varphi}_{\mathrm{c}}$ and $\vec{\varphi}_{\mathrm{f}}$ differ.

Details on the Transformation

The transformation **P** is determined in an iterative process, starting with a set of fine model base points $\mathbf{B}_{\mathrm{f}} = \{\vec{\varphi}_{\mathrm{f}}^{1}, \vec{\varphi}_{\mathrm{f}}^{2}, ..., \vec{\varphi}_{\mathrm{f}}^{m}\}$. Subsequently, $\vec{R}_{\mathrm{f}}(\vec{\varphi}_{\mathrm{f}}^{i})$, $i = 1, 2, ..., m$ is

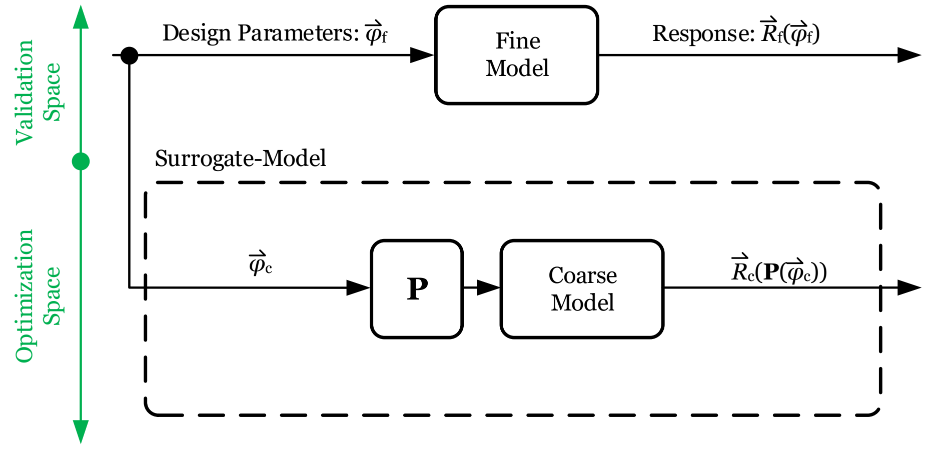
Validation Space
Optimization Space
Design Parameters: $\vec{\varphi}_{\mathrm{f}}$
Fine Model
Response: $\vec{R}_{\mathrm{f}}(\vec{\varphi}_{\mathrm{f}})$
Surrogate-Model
$\vec{\varphi}_{\mathrm{c}}$
P
Coarse Model
$\vec{R}_{\mathrm{c}}(\mathbf{P}(\vec{\varphi}_{\mathrm{c}}))$

Figure 4.10: Principle idea of the space mapping approach, based on [79].

determined, and a set of coarse model base points $\mathbf{B}_{\mathrm{c}} = \{\vec{\varphi}_{\mathrm{c}}^{1}, \vec{\varphi}_{\mathrm{c}}^{2}, ..., \vec{\varphi}_{\mathrm{c}}^{m}\}$ is identified via parameter extraction (PE), so that (4.2) holds for each pair of corresponding base points in $\mathbf{B}_{\mathrm{f}}$ and $\mathbf{B}_{\mathrm{c}}$. This PE is an optimization process on its own, where different optimization algorithms can be used. Using these initial sets $\mathbf{B}_{\mathrm{f}}$ and $\mathbf{B}_{\mathrm{c}}$, $\mathbf{P}_1$ can be established. If the transformation does not meet (4.2), further sets can be added throughout the iterative process, detailed in Appendix C.2.1.

This determination of **P** is also called (offline) model enhancement. Strategies that add information to **P** during an actual design optimization have also been proposed, which is better known as aggressive space mapping. In the scope of this thesis, model enhancement with input mapping is used to obtain a coarse system response so that (4.2) holds true.

Each transformation $\mathbf{P}_{\mathrm{j}}$ (with j being the jth iteration of transformation enhancement) is defined as a linear combination of some predefined and fixed fundamental functions $f(\vec{\varphi}_{\mathrm{f}})$, which translates into the following matrix form:

$$\vec{\varphi}_{\mathrm{c}} = \mathbf{P}_{\mathrm{j}}(\vec{\varphi}_{\mathrm{f}}) = \mathbf{A}_{\mathrm{j}} f(\vec{\varphi}_{\mathrm{f}}) \tag{4.3}$$

where $\mathbf{A}_{\mathrm{j}}$ is a $k \times m$ transformation matrix. Considering the mapping $\mathbf{P}_{\mathrm{j}}$ for all points in the sets $\mathbf{B}_{\mathrm{f}}$ and $\mathbf{B}_{\mathrm{c}}$, leads to:

$$\left[\vec{\varphi}_{\mathrm{c}}^{1}\ \vec{\varphi}_{\mathrm{c}}^{2}\ ...\ \vec{\varphi}_{\mathrm{c}}^{m_j}\right] = \mathbf{A}_{\mathrm{j}} \left[f(\vec{\varphi}_{\mathrm{f}}^{1})\ f(\vec{\varphi}_{\mathrm{f}}^{2})\ ...\ f(\vec{\varphi}_{\mathrm{f}}^{m_j})\right]. \tag{4.4}$$

Defining

$$\mathbf{C} = \left[\vec{\varphi}_{\mathrm{c}}^{1}\ \vec{\varphi}_{\mathrm{c}}^{2}\ ...\ \vec{\varphi}_{\mathrm{c}}^{m_j}\right] \tag{4.5}$$

as suggested in [74] and

$$\mathbf{D} = \left[f(\vec{\varphi}_\mathrm{f}^{1})\; f(\vec{\varphi}_\mathrm{f}^{2})\; \dots\; f(\vec{\varphi}_\mathrm{f}^{m_j}) \right] \tag{4.6}$$

(4.4) can be rewritten as

$$\mathbf{C} = \mathbf{D}\mathbf{A}_\mathrm{j}^{T}. \tag{4.7}$$

Eventually, the least-squares solution to this system is

$$\mathbf{A}_\mathrm{j}^{T} = \left(\mathbf{D}^{T}\mathbf{D}\right)^{-1}\mathbf{D}^{T}\mathbf{C}. \tag{4.8}$$

For illustrating this abstract concept, an example on how to derive an initial transformation can be found in Appendix C.2.1.

In this example, the example case drive's geometry is scaled up by 20 % and 40 % in radial direction. The parameter sets of these machine designs form the base points $\mathbf{B}_\mathrm{f}$ and $\mathbf{B}_\mathrm{c}$. With a parameter extraction process, the parameter sets of $\mathbf{B}_\mathrm{c}$ are adapted so that (4.2) holds.

As referred to in Appendix C.2.1, these adapted parameter sets form $\mathbf{B}_\mathrm{m}$. Submitting these parameter sets to the coarse model provides coarse model responses, so that (4.2) holds. With the transformation $\mathbf{P}$, (4.2) holds for the limited parameter space upon which $\mathbf{P}$ is based.

$\mathbf{P}$ is determined by its transformation matrix $\mathbf{A}_\mathrm{j}$, which can be determined with (4.8). With this transformation, fine parameter sets $\vec{\varphi}_\mathrm{f}$ can be submitted to the coarse model with input space mapping. Thus, the coarse model response $\vec{R}_\mathrm{c}$ resembles the fine model response $\vec{R}_\mathrm{f}$ with reasonable accuracy and short computational time.

The transformation in Appendix C.2.1 turned out to be non-invertible. Thus, a transformation of a coarse to a fine parameter set is not possible. The transformation also shows a sensitivity to slight changes of the matrix elements in $\mathbf{C}$ and $\mathbf{D}$. Iteratively adding more parameter sets, as described in Appendix C.2.1, could improve this sensitivity.

4.5 Summary Computer Aided System Optimization

Automating parts of the design process and hence aiding the design engineers' decisions is a timely topic. For designing electrical drives, multiple disciplines have to be considered, and hence the determination of the best solution for a given problem proves to be very challenging.

With stochastic optimization, a robust and promising variant of enhancing the motor or drive design process is introduced. This approach identifies the global optimum with very high probability and can be well integrated in a software that assembles and links the different models in use.

Instead of utilizing a single design software, with its corresponding limitations, system simulation and optimization that allows for the selection of the individually optimum tools via implemented interfaces is set up.

With surrogate models, a possibility for reducing computational effort is introduced. Approaches such as space mapping, but also radial basis functions (used with the loss-surface algorithm) or artificial neural networks (recently introduced in SyMSpace®) could be used for substituting the FEA model, as shown in Figure 4.3.

Chapter 5

Reflections on the Topic

5.1 Systematic Design Workflow

A design process should be carried out systematically so that all who are participating can contribute efficiently. A formal representation of such a systematic design workflow, as presented in [80], is used as the baseline for the discussion. Figure 5.1 portrays such a formal design process. It is presented in three parts, with additional detailed descriptions and practical implementation examples. A conventional workflow is shown and is compared to the proposed workflow that takes advantage of the new tools, illustrating the different improvements with respect to workflow systematization and saving design time.

For the workflows' systematization, an interface is provided for the models in use. This interface is the SyMSpace® environment, the implementation is depicted in Figure 4.2 in Section 4.2.4. With this setup, following the design workflow is straightforward because repetitive tasks are implemented in the software, plausibility checks and parameter limitations prevent errors, and accessing the input and output data of the models is standardized.

The expected decrease in design time is based on the application of different modeling techniques and the automation of repetitive optimization tasks.

As presented in Figure 5.2, at the beginning of every design process is a problem which is intended to be solved. In this example case, the parameters that determine the magnetic motor circuit are to be identified so that the desired performance is met. The first step in finding a solution to this problem comprises two elements: First, the identification of an independent parameter set defining the geometry, presented in Table 2.1, and second, the definition of the specification parameters, presented

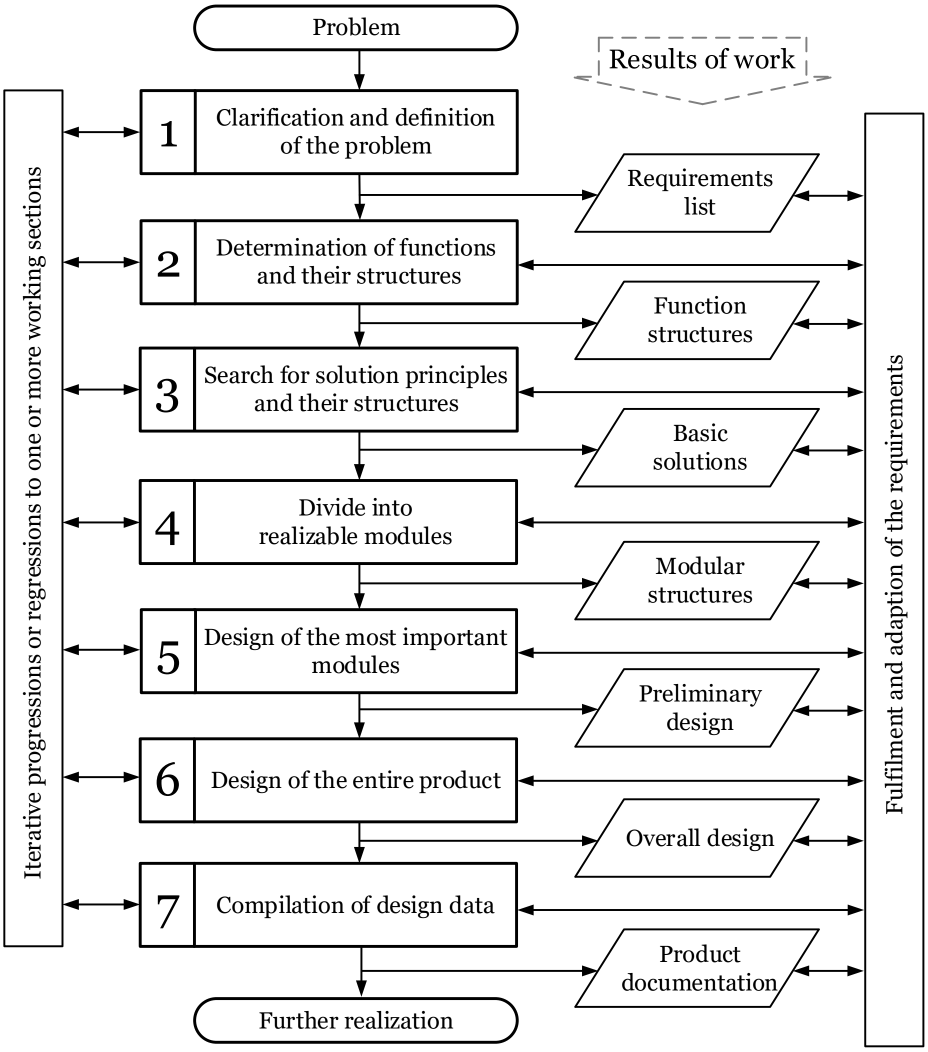
Problem
Results of work
1
Clarification and definition of the problem
Requirements list
2
Determination of functions and their structures
Function structures
3
Search for solution principles and their structures
Basic solutions
4
Divide into realizable modules
Modular structures
5
Design of the most important modules
Preliminary design
6
Design of the entire product
Overall design
7
Compilation of design data
Product documentation
Further realization
Iterative progressions or regressions to one or more working sections
Fulfilment and adaption of the requirements

Figure 5.1: Generic design process, illustrated as per [80].

in Table 2.2; both tables can be found in Section 2.2.1. The parameter sets are implemented in the SyMSpace® environment.

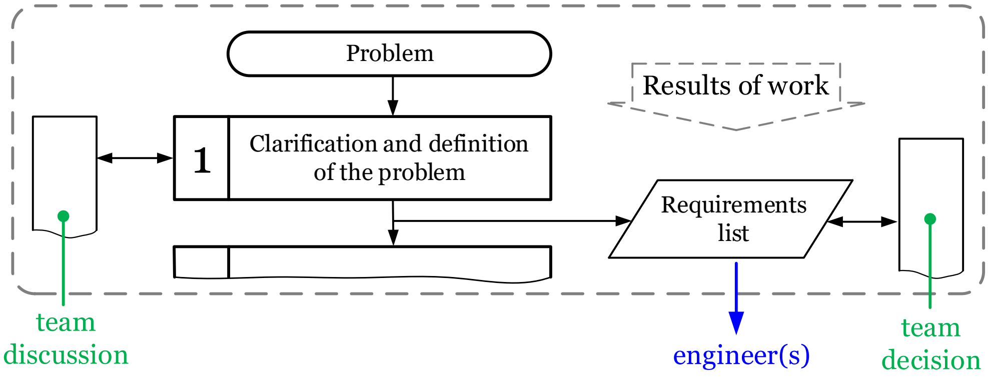

Figure 5.2: Part I of the general design process.

Figure 5.3 presents the different steps of this generic design process. The steps 2 - 4, enclosed by the dashed green line, are the core functionality of the proposed workflow. Within these steps, all required functionality is implemented. This functionality is the utilization of appropriate modeling techniques and the accessibility of these models with a standardized interface.

Figure 5.4 reveals how such functionality is implemented in SyMSpace®. Functions for directly calculating parameters or interfaces between other software can be defined in this tree structure. The containers for these functions are filled with existing or self developed models presented in Section 2.2 and Section 4.3. This fulfills Steps 2 and 3 of the approach in Figure 5.3.

Step 4 is represented with Figure 5.5. The model functions are separated into logical modules to enable exchangeability and extensibility. These modules consist of analytic equations or interfaces between external models. The exchangeability allows for straightforward modifications. For example, the geometry equations for an outer-rotor topology can be exchanged by equations for an inner-rotor topology.

Figure 5.5 shows how such a modular tree structure is implemented in SyMSpace®. Every module represents a container with the implemented functionality. Highlighted with rectangles in red is an iron loss module. This module contains the loss-surface algorithm presented in Section 3.1.1. The algorithm is implemented in an external Python® function. The interface for applying settings to the algorithm is

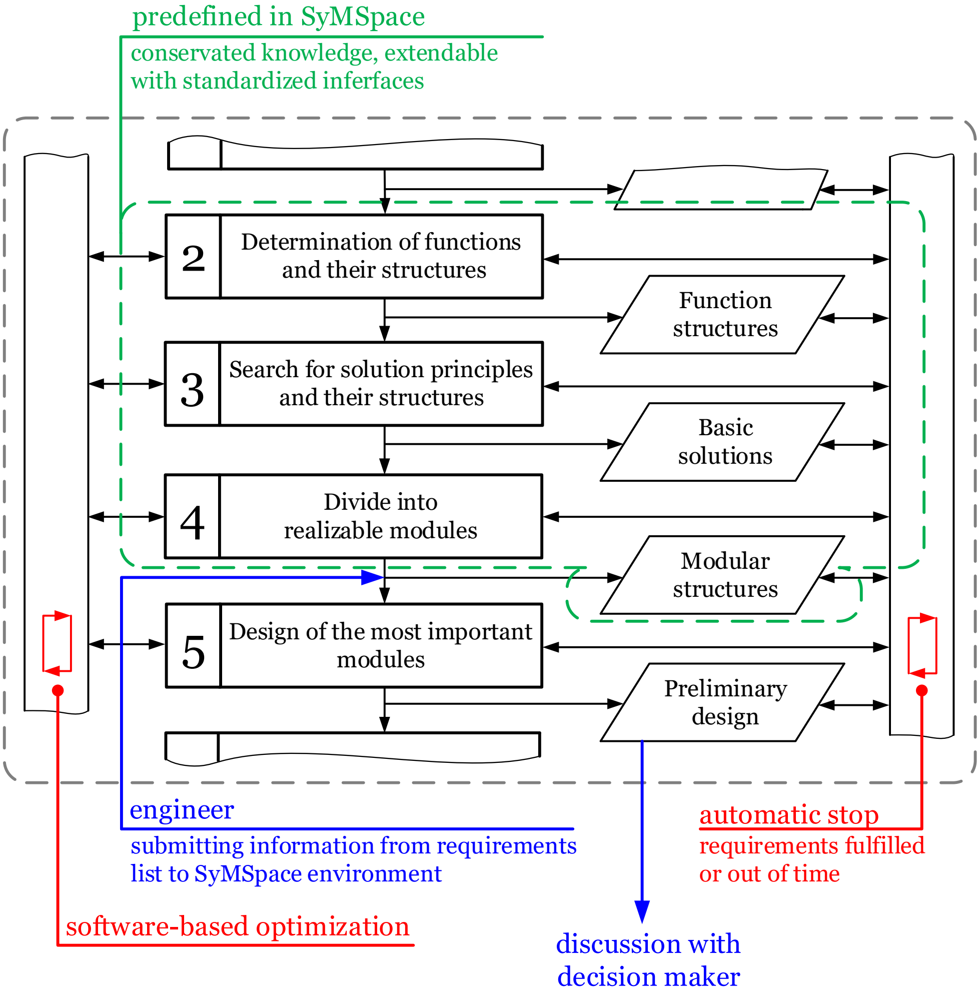
predefined in SyMSpace
conservated knowledge, extendable with standardized inferfaces
2
Determination of functions and their structures
Function structures
3
Search for solution principles and their structures
Basic solutions
4
Divide into realizable modules
Modular structures
5
Design of the most important modules
Preliminary design
engineer
submitting information from requirements list to SyMSpace environment
automatic stop
requirements fulfilled or out of time
software-based optimization
discussion with decision maker

Figure 5.3: General design process: details steps 2 to 5.

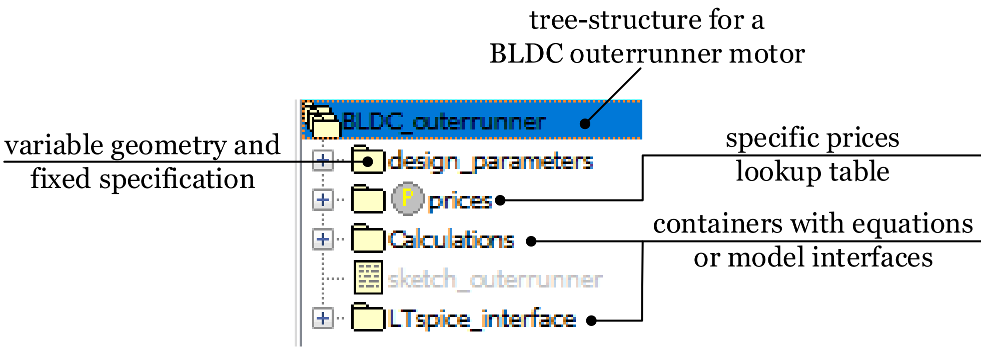
tree-structure for a BLDC outerrunner motor
BLDC_outerrunner
design_parameters
prices
Calculations
sketch_outerrunner
LTspice_interface
variable geometry and fixed specification
specific prices lookup table
containers with equations or model interfaces

Figure 5.4: Logical tree structure of the electric motor model implemented in the SyMSpace® environment.

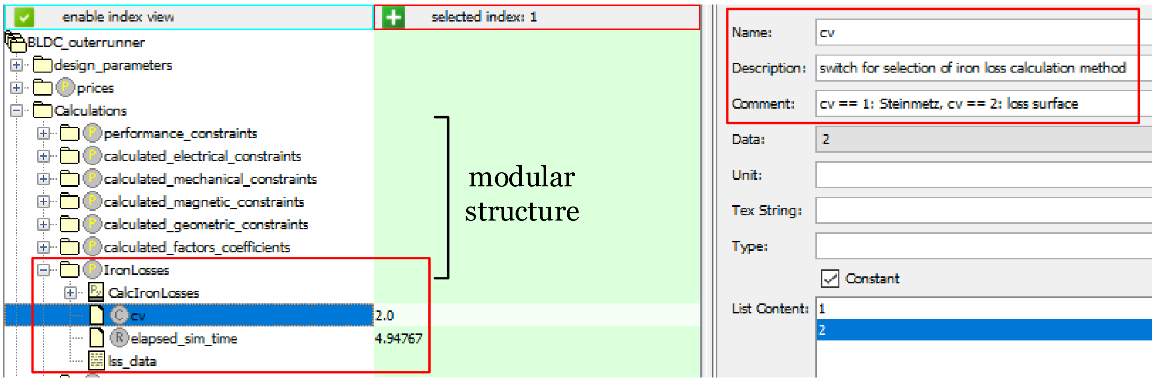
☑ enable index view
selected index: 1
BLDC_outerrunner
design_parameters
prices
Calculations
performance_constraints
calculated_electrical_constraints
calculated_mechanical_constraints
calculated_magnetic_constraints
calculated_geometric_constraints
calculated_factors_coefficients
IronLosses
CalcIronLosses
cv
elapsed_sim_time
lss_data
modular
structure

cv 2.0
elapsed_sim_time 4.94767

Name: cv
Description: switch for selection of iron loss calculation method
Comment: cv == 1: Steinmetz, cv == 2: loss surface
Data: 2
Unit:
Tex String:
Type:
☑ Constant
List Content: 1
2

Figure 5.5: Modular structure of the electric motor model with highlighted iron loss module implemented in the SyMSpace® environment.

visible. The input parameters, e.g., magnetic flux density, and the ouput parameters, e.g., specific iron losses, are directly interfaced via respective variables.

In the last phase of the proposed design workflow, a candidate solution's characteristics are investigated. Characteristics of interest could be an efficiency map, power density, and motor torque or speed constants. These characteristics are important measures for a design's quality. Step 7 of Figure 5.6 covers this workflow. In Step 6, further design aspects, not related to the magnetic circuit are carried out, e.g., design of the drives' housing.

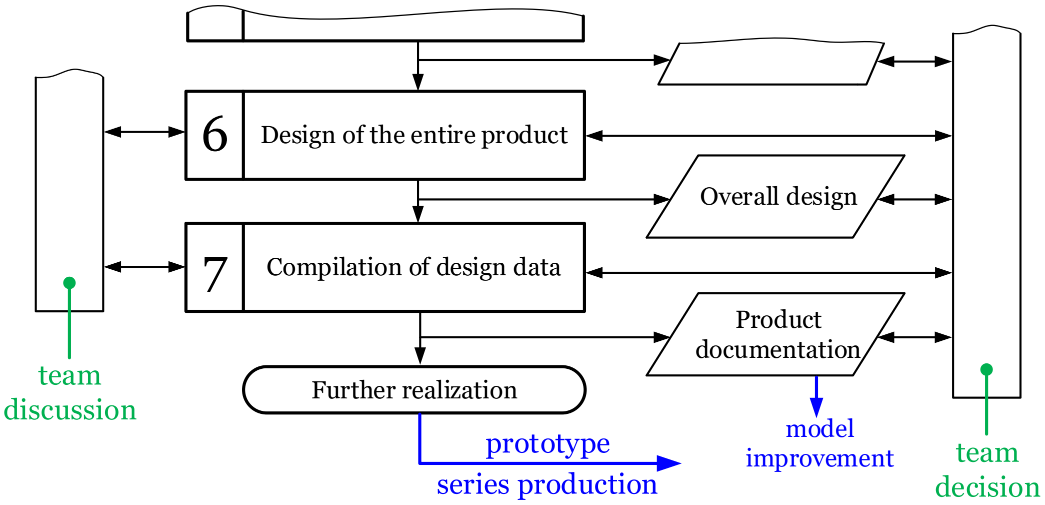
6
Design of the entire product
Overall design
7
Compilation of design data
Product documentation
Further realization
prototype
series production
model improvement
team discussion
team decision

Figure 5.6: Compilation of design data of an optimal candidate solution, completing the proposed design workflow.

5.2 Example Case Study

To provide this systematic design concept with tangible results, an example case study is presented. This study accompanies the design of an FHP outer-rotor application. The design time investigation is based on empirical data. This empirical data is gained from the evaluation of both a conventional and a proposed workflow. The conventional workflow utilizes one of the established software frameworks for electric motor design, and a trial-and-error approach for optimization. The proposed workflow finds the optimal design with the presented systematics.

5.2.1 Topology Choice Workflow

A common subject of discussion in this early design stage of FHP pump and fan applications is which motor topology to select. Due to manufacturing reasons and the availability of certified power electronics, single- and three-phase applications are most common, both in inner- and outer-rotor configuration. The proposed workflow utilizing the SyMSpace® environment is capable of showing the performance limits, e.g., in terms of efficiency, for different topologies in a quick and systematic way.

Figure 5.7 shows such a topology comparison. Figure 5.7(a) is a single-phase and Figure 5.7(b) a three-phase topology, all other specification parameters and the outer dimensions are the same. The efficiency for each topology is highlighted in the list of performance constraints, and the systematic organization with different indices in one common project, at the bottom of the screenshots.

Figure 5.8 compares a conventional topology choice workflow with the workflow proposed based on the tools of this thesis, including a timeline.

With the proposed workflow, a reduction of design time by 50 % is expected for this design step. This is achieved by leaving the topology choice to the SyMSpace® optimizer. As presented in Figure 5.7, the analytic model can be used for single-, or multi-phase investigations.

As shown in Figure 5.8, the proposed workflow consists of two design steps. SyMSpace® I is the setup of the optimization task. In this task, design parameters are initialized, limits of these parameters are set, and settings for the optimization algorithm are selected. SyMSpace® II contains the automated optimization and evaluation of the results.

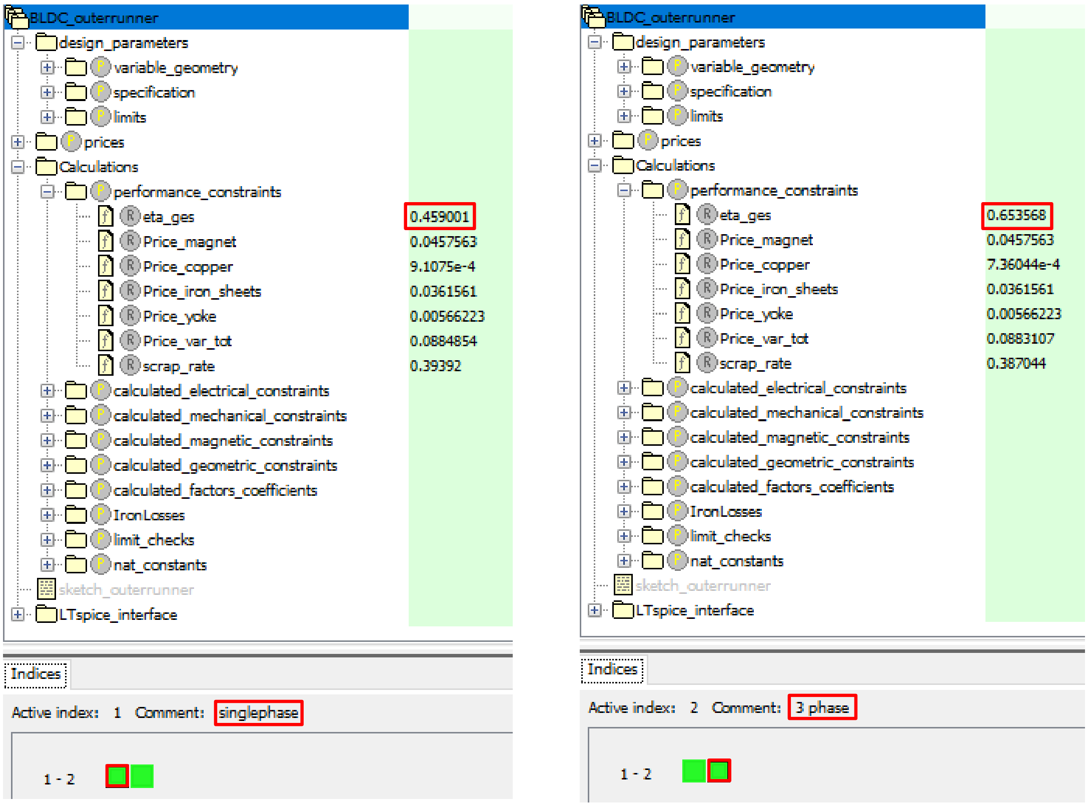

(a)

- BLDC_outerrunner
  - design_parameters
    - variable_geometry
    - specification
    - limits
  - prices
  - Calculations
    - performance_constraints
      - eta_ges 0.459001
      - Price_magnet 0.0457563
      - Price_copper 9.1075e-4
      - Price_iron_sheets 0.0361561
      - Price_yoke 0.00566223
      - Price_var_tot 0.0884854
      - scrap_rate 0.39392
    - calculated_electrical_constraints
    - calculated_mechanical_constraints
    - calculated_magnetic_constraints
    - calculated_geometric_constraints
    - calculated_factors_coefficients
    - IronLosses
    - limit_checks
    - nat_constants
  - sketch_outerrunner
  - LTspice_interface

Indices

Active index: 1 Comment: singlephase

1 - 2 🟩 🟩

(b)

- BLDC_outerrunner
  - design_parameters
    - variable_geometry
    - specification
    - limits
  - prices
  - Calculations
    - performance_constraints
      - eta_ges 0.653568
      - Price_magnet 0.0457563
      - Price_copper 7.36044e-4
      - Price_iron_sheets 0.0361561
      - Price_yoke 0.00566223
      - Price_var_tot 0.0883107
      - scrap_rate 0.387044
    - calculated_electrical_constraints
    - calculated_mechanical_constraints
    - calculated_magnetic_constraints
    - calculated_geometric_constraints
    - calculated_factors_coefficients
    - IronLosses
    - limit_checks
    - nat_constants
  - sketch_outerrunner
  - LTspice_interface

Indices

Active index: 2 Comment: 3 phase

1 - 2 🟩 🟩

Figure 5.7: Topology comparison of (a) a single-phase topology with an efficiency of 45.9 % and (b) a three-phase topology of an FHP machine with same specification and outer dimensions with 65.4 % efficiency in the SyMSpace® environment.

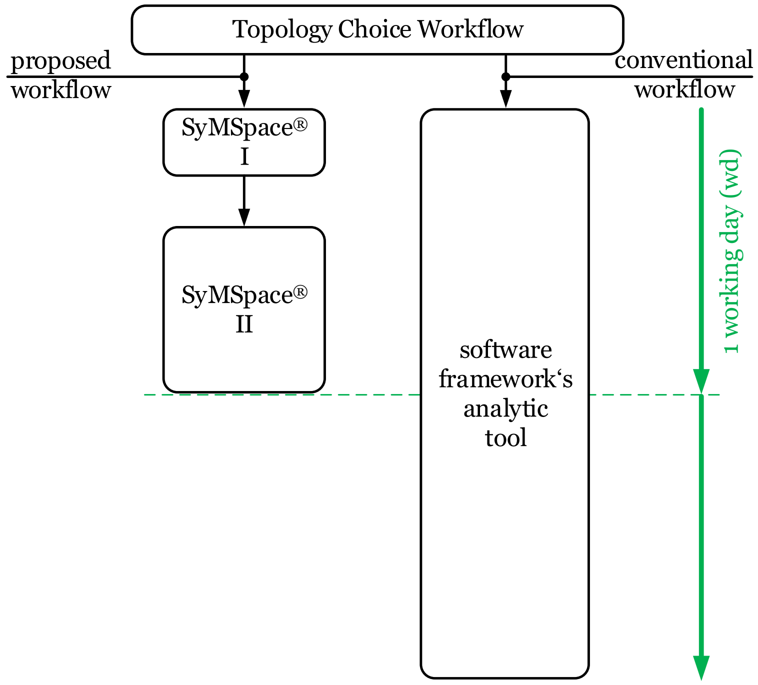
Topology Choice Workflow
proposed workflow
conventional workflow
SyMSpace® I
SyMSpace® II
software framework's analytic tool
1 working day (wd)

Figure 5.8: Topology choice workflow, with an expected 50 % decrease of design time; SyMSpace® I is the setup of the optimization task, SyMSpace® II contains the automated optimization and evaluation of the results[1].

The decrease in the design time for this topology choice workflow can be explained by the automated optimization introduced.

5.2.2 Design Workflow

Once the topology has been decided upon, the detailed design and optimization can begin.

Figure 5.9 shows the design workflow of the magnetic circuit, resembling Step 5 from Figure 5.3. For this example case study, it is assumed that the specifications now change n times during the design workflow. This is indicated by the loop at the SyMSpace® blocks in the proposed workflow. Each change of specification involves a rerun of the optimization task. Therefore, a globally optimum result can be achieved with high probability, even after a change in specification. With the conventional workflow, model changes are complex, e.g., due to the reassembling of the mesh. Therefore, with the conventional method it is likely to only achieve a local optimum as changes in the model tend to be avoided.

---

[1] A working day, shortened as wd, is defined as 8 hours at 60 minutes each.

Although a significant change in specification occurred, a decrease of design time by approximately 20 % is expected. This decrease is achieved by the automated optimization with a computational fast model.

Eventually, the FE motor design software is also utilized with the proposed workflow. This is necessary for refining, e.g., the stator tooth geometry, which is not covered by the fast model.

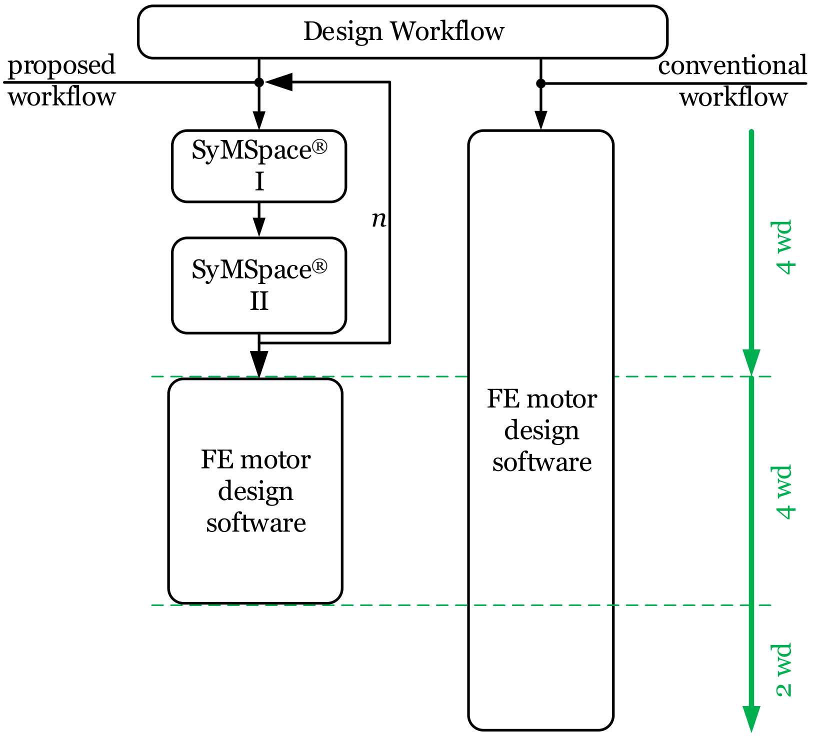
Design Workflow
proposed workflow
conventional workflow
SyMSpace® I
SyMSpace® II
n
FE motor design software
FE motor design software
4 wd
4 wd
2 wd

Figure 5.9: Comparison of the design workflow of the magnetic circuit of the conventional workflow, utilizing an FE motor design software, with the proposed workflow using SyMSpace®; SyMSpace® I is the setup of the optimization task, SyMSpace® II contains the automated optimization and evaluation of the results.

Figure 5.10 portrays the cost-efficiency Pareto-front of the example case design process. In addition to the Pareto-optimal candidate solutions, a metric for the convergence of the optimization process, or a sensitivity analysis of the parameters are both available within SyMSpace®. This helps the design engineer in choosing a candidate solution for further investigations.

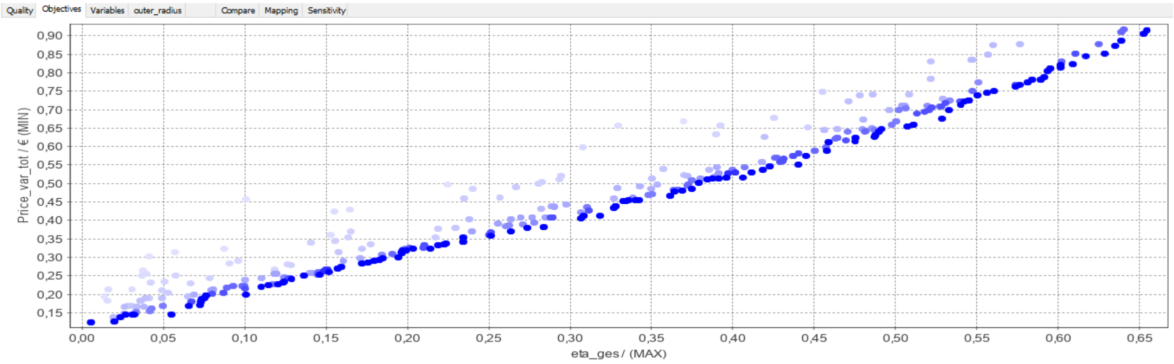

Figure 5.10: Cost-efficiency Pareto-front from the investigated design process of the example case application.

5.2.3 Compilation of Design Data

Figure 5.11 compares the determination of an efficiency map for the example case application. A decrease in the design time of approximately 67 %, from three working days to one working day, is expected. This figure is based on investigations on computational effort of the simulation setups in use. The FE motor design setup takes approximately two hours for calculating one operating point. The proposed setup, presented in Figure 4.3 in Section 4.3, needs only approximately thirty seconds. As presented in Figure 4.3, the proposed workflow also requires data from the FE motor design software. This data is already available due to FE computations for design refinement, as shown in Figure 5.9. In the proposed workflow, this data must only be computed once, and can be reused for the computation of different operating points. This underlines the advantage of interfacing the best suited models for electric motor design.

5.2.4 Summary Example Case Study

Summarizing the design times in Figure 5.8, Figure 5.9, and Figure 5.11, an overall decrease in the design time of 67 % down to 33 % is evident. This decrease in the design time can be explained by introducing a different design systematization. This systematization is based on utilizing different, partly computational less expensive models, and submitting them to automated optimization within a well-structured environment with clear, well-defined interfaces.

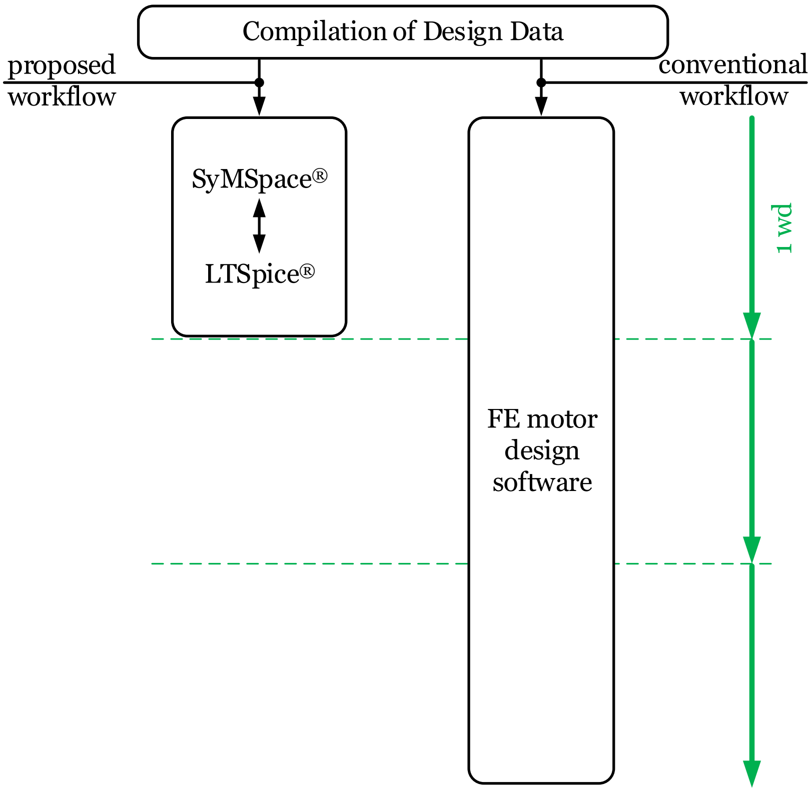
Compilation of Design Data
proposed workflow
conventional workflow
SyMSpace®
LTSpice®
FE motor design software
1 wd

Figure 5.11: Compared workflows for efficiency map determination of the example case application. A decrease of design time by approximately 67 %, down to 33 %, is expected, due to lower computational effort.

Conclusion

This thesis contributes to established models and workflows, widely used for designing electric machines. Studies based on the presented example case drive provide results to make the introduced abstract concepts more tangible.

For determining iron losses, a loss-surface approach, based on experimental data, is developed. With this loss-surface approach, the difference between experimental and computed results can be reduced to below 5 %. Widely used approaches, e.g., based on the Steinmetz-equation, underestimate iron losses and require the aid of correction factors. The loss-surface approach is implemented in a Python® function, integrated in the SyMSpace® environment.

Magnet related stray paths and inductances are analyzed and separated with an FEA. Approximately 90 % of the magnet flux is available for torque generation, in contrast to approximately 50 % of the current related flux, as presented in Section 3.2. The FEA considers material degradation, as experimental data for the stator laminations and the rotor yoke is provided.

The thesis provides an analytic model, a finite element model, and a multiphysical model for electric machine design and system simulation. These models exhibit good congruity with experimental data. For computational expensive models, an alternative approach based on space mapping is discussed.

The introduced SyMSpace® environment accesses these models and allows for multi-objective optimization. A design workflow, utilizing these models and allowing for the automation of repetitive tasks, is implemented. By comparison, an established design process would require 33 % more in design time. The SyMSpace® environment provides a modular setup. This modular setup allows for extendibility for the models in the future.

Appendix A

Baseline Illustrations

A.1 Test-Setup for Static Material Investigations

A.1.1 Baseline Illustrations for Material Investigations

The relative permeabilities of the stator laminations and of the rotor yoke were determined to identify the degree to which the true values would differ. The stator laminations and the rotor yoke were investigated by dynamic and static material tests according to IEC standards 60404-6 and 60404-4, respectively. The AC-Test according to IEC standard 60404-6 utilizes the test setup described in Appendix B.1.2, the DC-Test according to IEC standard 60404-4 uses the setup shown in Appendix A.1.2. The results are presented in Figure 2.5 in Section 2.1, and reveal a large difference to the datasheet values. These results were used within the FEA models, described in Appendix A.2.

A.1.2 Description of the DC-Test

This section reports on the static material investigations. Figure A.1 shows the components of the test bench used to investigate the soft magnetic material. The ring sample, introduced in Appendix B.1.3 serves as the material under test, working essentially like a transformer. The power amplifier has a rated power of up to 15 kVA with a maximum voltage of 270 V_{peak} and a bandwith of 5 kHz (-3 dB). The power resistor is introduced as a minimum load for the power amplifier. The primary current i_{pri} along with the primary voltage u_{pri} of the ring sample are measured with a programmable high precision data recorder from [81], where the magnetic field H is derived from i_{pri}. u_{sec} is submitted to a fluxmeter from [82], for deriving the magnetic flux ϕ_{sec}, this signal is submitted to the data recorder as well. The experimental setup and post-processing of the data meets the standard IEC60404-4:1995 [83]. The magnetic field strength *H* is chosen to meet the operating range of the rotor yoke.

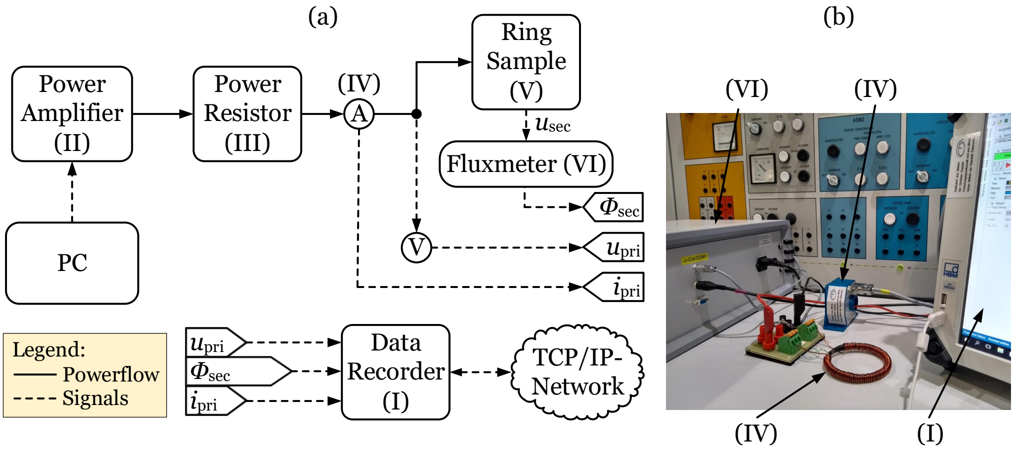
(a)
Power Amplifier (II)
Power Resistor (III)
(IV)
A
Ring Sample (V)
u_{sec}
Fluxmeter (VI)
Φ_{sec}
V
u_{pri}
i_{pri}
PC
Legend:
—— Powerflow
---- Signals
u_{pri}
Φ_{sec}
i_{pri}
Data Recorder (I)
TCP/IP-Network
(b)
(VI)
(IV)
(IV)
(I)

Figure A.1: Test setup to determine the relative permeabilities of the stator laminations and of the rotor yoke with (a) block diagram and (b) photos of the setup, as reported on in [40].

A.2 Details of the FEA Models Used

Figures A.2 and A.3 show the 2D- and 3D-meshes of FEA implementations of the example case drive of Section 2.1.

With each model, symmetries were exploited to keep the mesh elements and therefore the computational effort low. In both models, the important airgap area was provided with a finer mesh resolution with at least 5 layers within the airgap. For the 3D-model, a fine mesh resolution for the air region in the area of the overhang structures was identified as necessary, too. As mentioned in Section 2.1, these overhang structures strongly influence the magnetic circuit.

In both cases, 2D and 3D, transient magnetic analyses were performed, computed in parallel on 8 cores on a desktop computer. The 2D model evaluates within a matter of minutes, whereas the 3D model takes several hours.

(a)

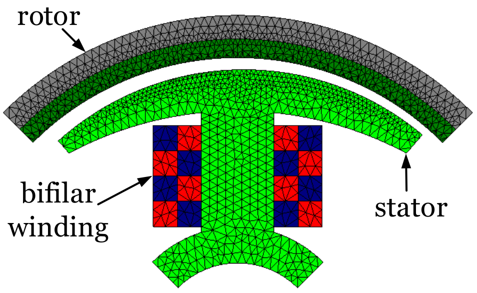
rotor
bifilar winding
stator

(b)

Parameter	Value
analysis method	2D transient magnetic analysis
parallelism	8 cores, desktop
mesh elements	4628
analysis time	~1m

Figure A.2: 2D-FEA model of the example case drive, (a) sketch of its mesh, and (b) details on the implementation and evaluation.

(a)

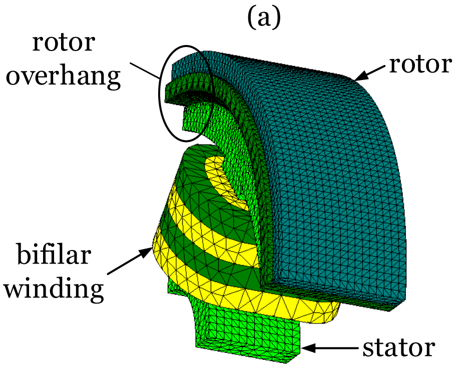
rotor overhang
rotor
bifilar winding
stator

(b)

Parameters	Value
analysis method	3D transient magnetic analysis
parallelism	8 cores, desktop
mesh elements	488.312
analysis time	approximately 2h

Figure A.3: 3D-FEA model of the example case drive with (a) a sketch of its mesh, and (b) details on implementation and evaluation.

A.3 Analytic Model as MATLAB® Code

The following code is a representation of the analytic PM motor's model. It is based on the implementation presented in [41, p. 125ff], extended with equations for an outer-rotor geometry and with the loss-surface approach for iron loss computation. This model is used as outlined in Section 2.2.1.

```
% Builds a permanent magnet motor using basic parameters
% ------------------------------------------------------
%
% variable parameters are:
%                       + outer stator radius: R_so
%                       + airgap height: h_ag)
%                       + number of pole pairs: p
%                       + number of stator slots: Q
%                       + magnet height: h_mg
%                       + stator tooth dimensions: d1, d2, d3
%                       + distance between toothtips: w_s
%                       + motor length: L_mt
%
% fixed parameters are:
%                       + magnet fraction: alpha_m (alpha_m < 1
%                       + remanent flux density: B_r
%                       + coercive field strength: H_c
%                       + max. peak phase voltage: E_max
%                       + rated mechanical speed: n_mech
%                       + rated mechanical power: P_mech
%                       + upper operating temperature (winding):
%                       eps_oper_high
%                       + lower operating temperature (magnet):
%                       eps_oper_low
%                       + reference temperature: eps_ref
%                       + number of phases: N_ph
%                       + iron stack factor: k_st
%                       + copper filling factor of the winding: k_cp
%                       + max. allowed flux density: B_max

% ------------------------------------------------------
function Motor = OuterPMMotor(VariableMachineParameters, FixedMachineParameters, NatConstants, Prices)

% limits for plausibility checks
%TORQUE_CONSTANT_LOWER_LIMIT = 0;
%CONDUCTOR_RADIUS_LOWER_LIMIT = 0;
%B_AG_LOWER_LIMIT = 0;

% setting variable machine parameters
Motor.R_so = VariableMachineParameters.R_so;
Motor.h_ag = VariableMachineParameters.h_ag;
Motor.alpha_m = VariableMachineParameters.alpha_m;
Motor.p = VariableMachineParameters.p;
Motor.QB_r = VariableMachineParameters.Q;
Motor.h_mg = VariableMachineParameters.h_mg;
Motor.d1 = VariableMachineParameters.d1;
Motor.d2 = VariableMachineParameters.d2;
Motor.d3 = VariableMachineParameters.d3;
Motor.w_s = VariableMachineParameters.w_s;
Motor.L_mt = VariableMachineParameters.L_mt;

% setting fixed machine parameters
Motor.B_r = FixedMachineParameters.B_r;
Motor.H_c = FixedMachineParameters.H_c;
Motor.E_max = FixedMachineParameters.E_max;
Motor.n_mech = FixedMachineParameters.n_mech;
Motor.P_mech = FixedMachineParameters.P_mech;
Motor.eps_oper_high = FixedMachineParameters.eps_oper_high;
Motor.eps_oper_low = FixedMachineParameters.eps_oper_low;
Motor.eps_ref = FixedMachineParameters.eps_ref;
Motor.N_ph = FixedMachineParameters.N_ph;
Motor.k_st = FixedMachineParameters.k_st;
Motor.k_cp = FixedMachineParameters.k_cp;
Motor.B_max = FixedMachineParameters.B_max;


%% Calculate air-gap flux and geometric variables
% inner rotor radius: R_ri
Motor.R_ri = Motor.R_so + Motor.h_ag;
% flux concentration factor: C_phi
Motor.C_phi = 2*Motor.alpha_m/(1+Motor.alpha_m);
% angular pole pitch: theta_p
Motor.theta_p = pi/Motor.p;
% angular slot pitch: theta_s
Motor.theta_s = 2*pi/Motor.Q;
% pole pitch at the outside surface of the stator: tau_p
Motor.tau_p = Motor.R_so*Motor.theta_p;
% slot pitch at the outside surface of the stator: tau_s
Motor.tau_s = Motor.R_so*Motor.theta_s;
% plausibility check for tau_s
if Motor.tau_s <= Motor.w_s
    error('Slot␣opening␣is␣bigger␣than␣the␣tooth␣width␣space!');
end
% temperature related change of remanent flux density
Motor.B_r = Motor.B_r*(1 + NatConstants.beta_magnet*(Motor.eps_oper_low - Motor.eps_ref));
% relative permeability of the magnet
Motor.mu_r = abs(Motor.B_r)/(abs(Motor.H_c)*NatConstants.mu_0);
% magnet leakage factor: k_ml
Motor.k_ml = 1 + 4*Motor.h_mg/(pi*Motor.mu_r*Motor.alpha_m*Motor.tau_p)*log(1+pi*Motor.h_ag/((1-Motor.alpha_m)*Motor.tau_p));
% permeance coefficient: P_c
Motor.P_c = Motor.h_mg/(Motor.h_ag*Motor.C_phi);
% Carter coefficient: k_c
Motor.k_c = (1-Motor.w_s/Motor.tau_p+4*Motor.h_ag/(pi*Motor.tau_p)*log(1+pi*Motor.w_s/(4*Motor.h_ag)))^(-1);
% air gap flux density
Motor.B_ag = Motor.B_r*Motor.C_phi/(1+Motor.mu_r*Motor.k_c*Motor.k_ml/Motor.P_c);
% plausibility check for air gap flux density
if Motor.B_ag < B_AG_LOWER_LIMIT
    error('Magnet␣can␣be␣demagnetized␣with␣this␣design!');
end
% air gap area: A_ag
Motor.A_ag = Motor.L_mt*Motor.tau_p*(1+Motor.alpha_m)/2;
% air gap flux: phi_ag
Motor.phi_ag = Motor.A_ag*Motor.B_ag;
% height auf the stator back iron: w_bi (for stator and rotor)
Motor.w_bi = Motor.phi_ag/(2*Motor.B_max*Motor.k_st*Motor.L_mt);
% outer rotor radius
Motor.R_ro = Motor.R_ri + Motor.h_mg + Motor.w_bi;
% number of slots per pole: N_sm
Motor.N_sm = Motor.Q/(2*Motor.p);
% tooth width at the bottom: w_tb (correction factor for flux squeeze at
% the tooth bottom (1-Motor.w_s/Motor.tau_s)^(-1))
Motor.w_tb = 2*Motor.w_bi/Motor.N_sm*(1-Motor.w_s/Motor.tau_s)^(-1);
% tooth width at the top (pole shoe width): w_t
Motor.w_t = Motor.tau_s-Motor.w_s;
% plausibility check for stator tooth geometry
if Motor.w_t < Motor.w_tb
     error('Pole␣shoe␣is␣smaller␣than␣stator␣tooth!');
end

% inner stator radius: R_si
Motor.R_si = Motor.R_so - (Motor.d1 + Motor.d2 + Motor.d3);
% conductor area
Motor.A_s = Motor.d3*(Motor.theta_s*(Motor.R_si+Motor.d3/2)-Motor.w_tb);
%length of the end winding
Motor.L_ew = (Motor.R_si + Motor.d3/2)*pi/Motor.Q;
% stator height
Motor.h_stator = Motor.d1 + Motor.d2 + Motor.d3 + Motor.w_bi;
% comprehensive stator area
Motor.A_stator_comp = Motor.h_stator * (Motor.theta_s*(Motor.R_so-Motor.h_stator/2));
% stator area between toothtips
Motor.A_tt = (Motor.d1+Motor.d2) * Motor.w_s;
% approximated (triangles) area below stator shoe
Motor.A_bs = Motor.d2*(Motor.w_t-Motor.w_tb)/2;
```

```
% stator area containing iron
Motor.A_iron = Motor.A_stator_comp - (Motor.A_s + Motor.A_tt + Motor.A_bs);
% mechanical rotor frequency
Motor.f_mech = Motor.n_mech/60;
% mechanical motor torque
Motor.T = Motor.P_mech/(2*pi*Motor.f_mech);
% electrical field frequency
Motor.f_elec = Motor.f_mech*Motor.p;
% electrical angular speed
Motor.omega_elec = 2*pi*Motor.f_elec;
% mechanical angular speed
Motor.omega_mech = 2*pi*Motor.f_mech;
% slot pitch in electrical radians
Motor.theta_se = pi*2*Motor.p/Motor.Q;
% number of slots per pole per phase
Motor.N_spp = Motor.Q/(2*Motor.p*Motor.N_ph);
% number of slots per phase
Motor.N_sp = Motor.N_spp*2*Motor.p;
% coil-pole fraction
Motor.alpha_cp = floor(Motor.N_spp)/Motor.N_spp;
%coil pitch at the rotor inside radius
Motor.tau_c = Motor.alpha_cp*Motor.tau_p;
% pitch factor
Motor.k_p = Motor.alpha_cp;
% coil pitch in electrical radians
Motor.theta_ce = pi*Motor.alpha_cp;
% skew factor for square wave flux density distribution
%Motor.k_s = 1-Motor.theta_se/(2*pi);
Motor.k_s = 1;
% distribution factor
Motor.k_d = sin(Motor.N_spp*Motor.theta_se/2)/(Motor.N_spp*sin(Motor.theta_se/2));
% number of coductors per slot
Motor.N_cond = floor(Motor.E_max/(2*Motor.p*Motor.k_d*Motor.k_p*Motor.k_s*Motor.B_ag*Motor.L_mt*Motor.R_ri*Motor.N_spp*Motor.omega_mech));
% copper wire radius (k_cp = copper filling factor)
Motor.R_cond = sqrt(Motor.A_s*Motor.k_cp/(Motor.N_cond*pi));
% plausibility check for copper wire radius
if Motor.R_cond <= CONDUCTOR_RADIUS_LOWER_LIMIT
    error('Radius␣of␣the␣copper␣wire␣too␣small');
end

% total current for the required torque
Motor.I_s = Motor.T/(Motor.p*Motor.k_d*Motor.k_p*Motor.k_s*Motor.B_ag*Motor.L_mt*Motor.R_ri*Motor.N_spp);
% rms phase current
Motor.I_ph = Motor.I_s/(Motor.N_cond*Motor.N_ph);
% plausibility check for the torque constant
if Motor.T/Motor.I_ph <= TORQUE_CONSTANT_LOWER_LIMIT
   error('Torque␣constant␣too␣low!');
end
% current density
Motor.J_c = Motor.I_s/(Motor.k_cp*Motor.A_s);
% winding resistance of the conductors in the slot
Motor.Res_s = (NatConstants.rho_cu*Motor.N_cond^2*Motor.L_mt)/(Motor.k_cp*Motor.A_s);
% winding resistance of the end turns
Motor.Res_e = (NatConstants.rho_cu*Motor.N_cond^2*pi*Motor.tau_c)/(2*Motor.k_cp*Motor.A_s);
% comprehensive phase resistance
Motor.Res_ph = Motor.N_sp*(Motor.Res_s+Motor.Res_e);
% temperature related change of resistance
Motor.Res_ph = Motor.Res_ph*(1 + NatConstants.beta_cu*(Motor.eps_oper_high - Motor.eps_ref));
% ohmic motor loss
Motor.P_ohm = Motor.N_ph*Motor.I_ph^2*Motor.Res_ph;
%iron volume of the complete motor
Motor.Vol_ir = Motor.k_st*Motor.L_mt*Motor.A_iron*Motor.Q;

% calculating iron losses of the machine
p_fe = CalcIronLosses(Motor.B_max, Motor.n_mech, Motor.p);

Motor.P_iron = p_fe*Motor.Vol_ir;

% calculation of demagnetization current
Motor.H_m = -Motor.H_c/(1+Motor.P_c);
Motor.B_m = Motor.B_r+NatConstants.mu_0*Motor.mu_r*Motor.H_m;
Motor.I_dm = 2*Motor.B_m*(Motor.h_mg+ Motor.mu_r*Motor.h_ag)/(Motor.N_cond*Motor.mu_r*NatConstants.mu_0);
```

```
% check difference between operating point and demagnetization
if Motor.I_dm < 1.5*Motor.I_ph
    error('Excessive␣spare␣current!');
end

%% calculation of efficiency
Motor.eta_ges = Motor.P_mech / (Motor.P_mech + Motor.P_ohm + Motor.P_iron + Motor.P_wind);

%% calculation of the (variable) costs
% magnet volume
Motor.Vol_magnet = Motor.alpha_m*pi*((Motor.R_ri+Motor.h_mg)^2-Motor.R_si^2)*Motor.L_mt;
% costs of the rotor magnet
Motor.Price_magnet = Prices.price_magnet*Motor.Vol_magnet*NatConstants.rho_magnet;
% copper volume
Motor.Vol_copper = Motor.Q*(Motor.L_mt+Motor.L_ew)*Motor.A_s*Motor.k_cp;
% price of the copper
Motor.Price_copper = Prices.price_copper*Motor.Vol_copper*NatConstants.rho_copper;
% total iron volume (including cutouts)
Motor.Vol_ir_tot = Motor.R_so^2*pi*Motor.L_mt*Motor.k_st;
% price of the iron sheets
Motor.Price_iron_sheets = Prices.price_ironsheets*Motor.Vol_ir_tot*NatConstants.rho_ironsheets;
% iron scrap rate
Motor.ScrapRate = 1-(Motor.Vol_ir_tot-Motor.Vol_ir)/Motor.Vol_ir_tot;
% yoke volume
Motor.Vol_yoke = pi*(Motor.R_ro^2 - (Motor.R_ri+Motor.h_mg)^2)*Motor.L_mt;
% price of the yoke
Motor.Price_yoke = Prices.price_yoke*Motor.Vol_yoke*NatConstants.rho_yoke;
% total variable costs
Motor.Price_var_tot = Motor.Price_magnet + Motor.Price_copper + Motor.Price_iron_sheets + Motor.Price_yoke;

end
```

Appendix B

Improved Modeling Approaches

B.1 Details on Loss-Surface Investigations

B.1.1 Overview

The loss-surface method for determining iron losses in magnetic circuits requires the experimental determination of magnetic flux density, its time derivative, and the iron losses in a sample, see Section 3.1.1. Appendix B.1.1 details how these data have been obtained and provides an overview, Appendix B.1.2 details the test setup, and Appendix B.1.3 provides more details on the samples used.

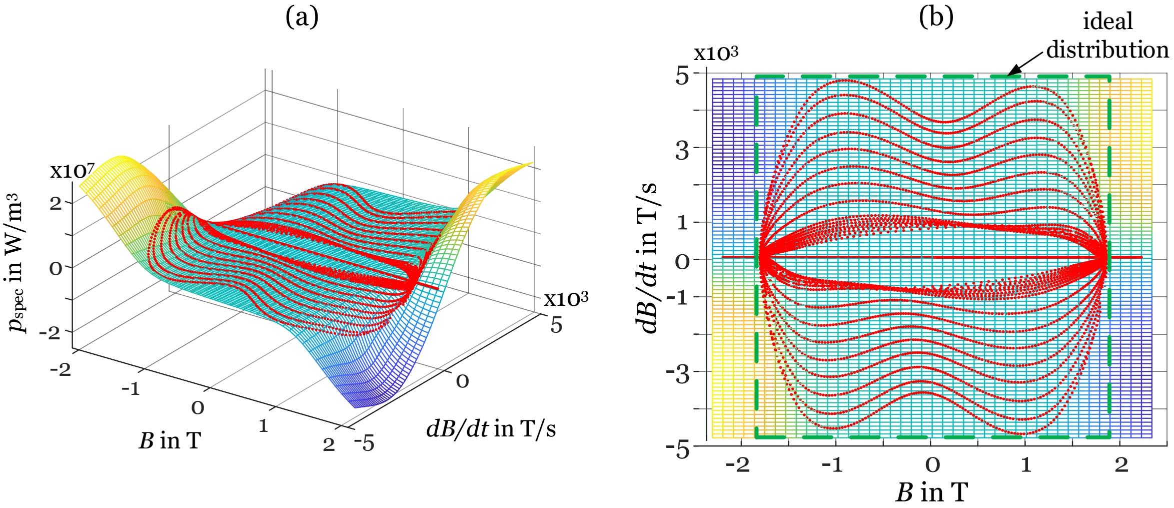

Figure B.1: Experimentally determined loss-surface with the measured supporting points (red dots); (a) 3D overview and (b) 2D view, indicating the difference between ideal and real distributions of measured supporting points.

Figure B.1 exemplarily presents an experimentally determined loss-surface, both in 3D and in 2D. The measured supporting points are shown as red dots, the calculated loss-surface is depicted as the colored surface. Figure B.1(b) illustrates the main challenges to obtaining appropriate experimental data, in which an ideal distribution of measured supporting points is indicated as a rectangle with a dashed green line. The real and the ideal situations differ strongly in areas with high absolute values of dB/dt and B. An ideal triangularly shaped flux density would allow for the obtaining of the ideal rectangularly shaped distribution of measured supporting points (Figure B.2), as sketched in Figure B.1(b).

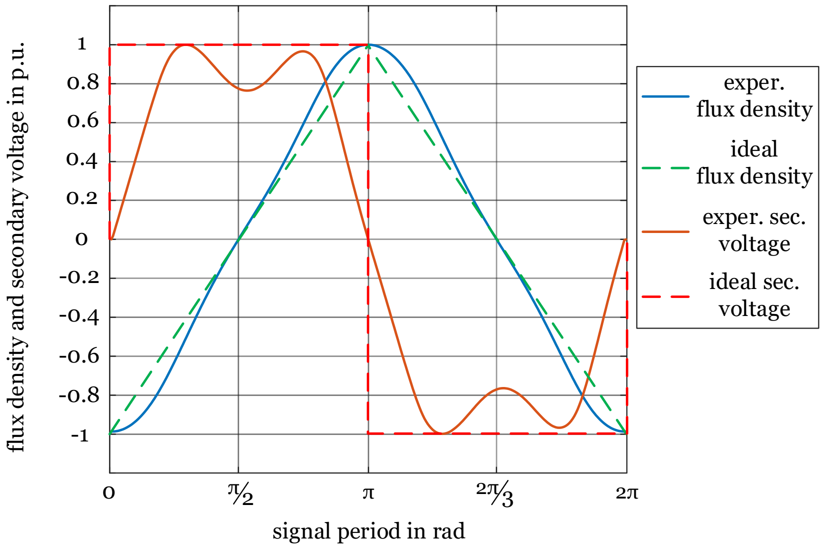

Figure B.2: Ideal and experimentally realized flux densities and secondary voltages as a function of time.

Figure B.2 also shows the experimentally obtained flux density and secondary voltage as a function of time. For low frequencies, the inductive reactance is small, and hence the power supply operates at its lower voltage limit. With the present setup, the lowest possible frequency that provided satisfactory results was 30 Hz. Otherwise, the maximum frequency of the power supply and the power supply's maximum voltage are the limiting factors.

The loss-surface was determined based on multiple experimentally obtained sets of data for f=[30...500] Hz and B up to ±1.7 T.

B.1.2 Test Setup for Loss-Surface Measurements

Figure B.3 shows the components of the test bench used to investigate soft magnetic material. The test specimen block indicates an Epstein frame or a toroidal specimen, with both working essentially like a transformer. The power amplifier has a rated power of up to 15 kVA with a maximum voltage of 270 V_{peak} and a bandwith of 5 kHz (-3 dB). An isolating transformer is used to block DC offsets. The primary current i_{pri} along with the primary and secondary voltages of the transformer, u_{pri} and u_{sec}, are measured with a programmable high precision data recorder, where the magnetic field H and the magnetic flux density B are calculated from i_{pri} and u_{sec}, respectively.

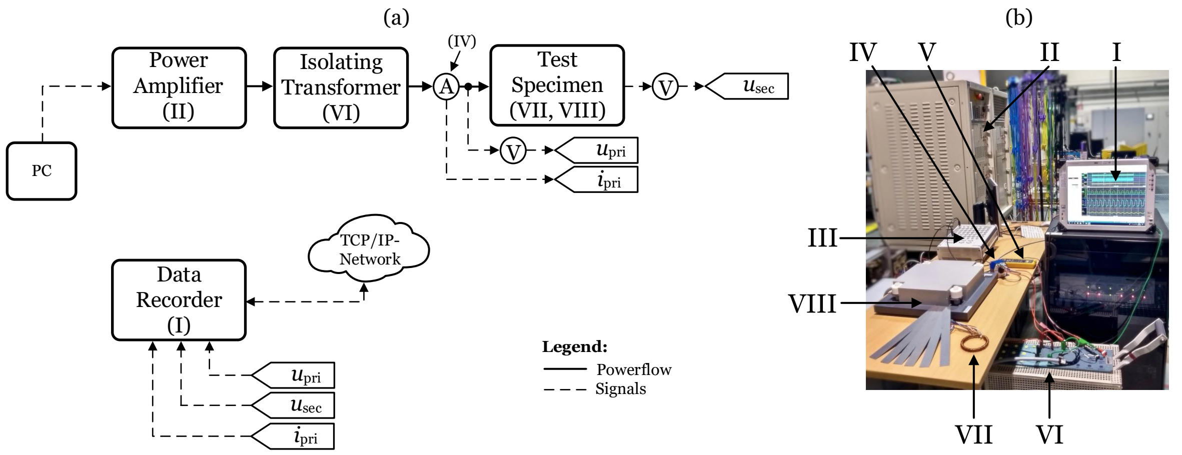
(a)
Power Amplifier (II)
Isolating Transformer (VI)
(IV)
A
Test Specimen (VII, VIII)
V
u_{sec}
V
u_{pri}
i_{pri}
PC
TCP/IP-Network
Data Recorder (I)
u_{pri}
u_{sec}
i_{pri}
Legend:
Powerflow
Signals
(b)
IV
V
II
I
III
VIII
VII
VI

Figure B.3: Test bench hardware overview, (a) shows the block diagram and (b) a picture of the test setup, linked together with numbers from I to VIII.

B.1.3 Toroidal Iron Sample for Loss-Surface Measurements

A toroidal ring setup was chosen for validation because of its simple magnetic circuit. Its iron stack cross-sectional area was chosen to closely resemble that of FHP drives (e.g., studied in [25]). The sample of soft magnetic material was prepared according to the standard IEC 60404-4:2009-08 [83], the most important quantities are defined and summarized in Table B.1 and Figure B.4.

Table B.1: Parameters of the toroidal iron stack used for validation.

Parameter	Value	Dimension
D	88.2	mm
d	80	mm
D/d	~ 1.1	–
N_{pri}	111	turns
N_{sec}	209	turns
Material	M250-35A	–
Lamination thickness (iron w/o isolation)	0.35	mm
Number of sheets	15	–
Total stack height (iron with isolation and glue)	5.3	mm

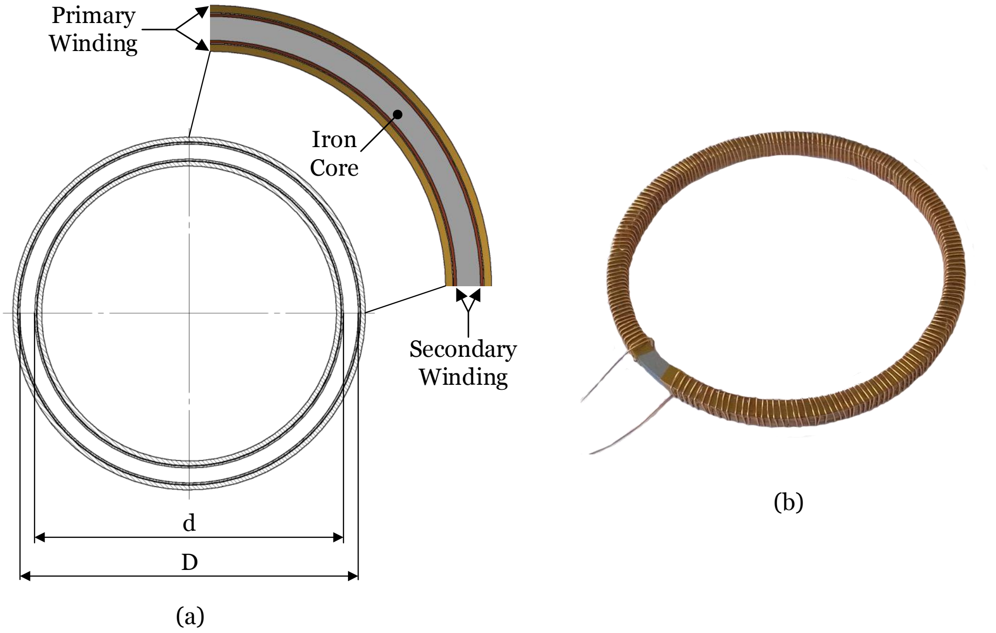

Figure B.4: Toroidal iron stack used for the validation of the loss-surface approach, (a) sketch with a detailed description, and (b) intermediate picture of the stack solely with the secondary winding. The parameters are shown in Table B.1.

B.2 Test-Setup for Stray Path Investigations

B.2.1 Description

For the experimental investigations of the machine, a motor test bench as shown in Figure B.5 is used. This motor test bench comprises a servo motor [84] (II) to load the machine under investigation, which is fitted on a mounting bracket. This servo motor can be operated with speed, position, and torque control. The rotor of the machine under investigation (III) can be directly attached to the servo motor while the stator (IV) is mounted on a holding device. This mechanical setup is shown in Figure B.6. For the measurements, a data recorder (I) from HBM® [81] is used, which provides high accuracy. Also, the coil current of the stator is measured with the use of a current sensor (V) from [85].

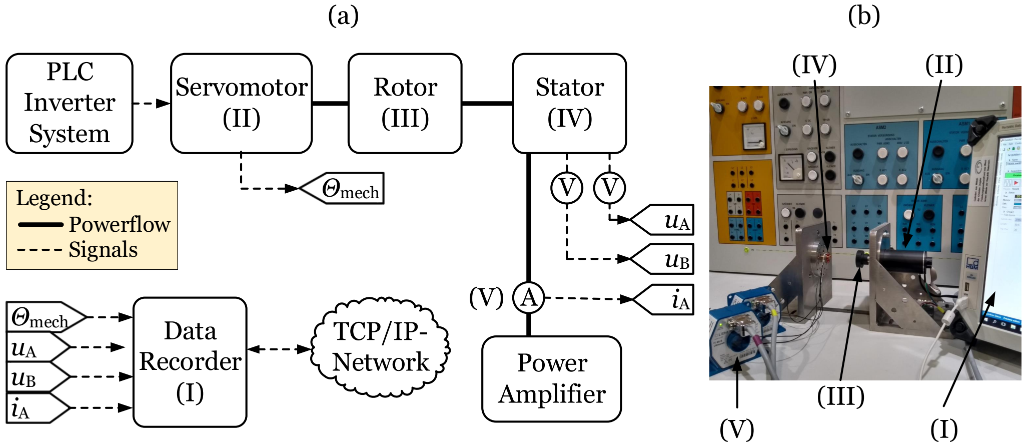
(a)
(b)
PLC Inverter System
Servomotor (II)
Rotor (III)
Stator (IV)
Legend:
Powerflow
Signals
Θ_{mech}
V
V
u_A
u_B
(V)
A
i_A
Power Amplifier
Θ_{mech}
u_A
u_B
i_A
Data Recorder (I)
TCP/IP-Network
(IV)
(II)
(III)
(V)
(I)

Figure B.5: Motor test bench, (a) block diagram and (b) overview photo of the setup, as reported on in [40].

B.2.2 Measurements

- BEMF
  The BEMF, as shown in Figure 2.3, is measured at the motor's no-load. The servo motor rotates the rotor cup controlled with its speed controller, the data recorder is connected to the windings via stator coil terminal (see Figure B.6(b)), measuring the BEMF. The position sensor's signal of the servomotor is recorded too, so that the BEMF can be measured as a function of the rotor position.

- Inductance
  Reproducible measurements of the motor inductance require alignment of the rotor with the rotor positions at 3 and 48 mechanical degrees, as described in Section 3.2.2. Hence, the servo motor's position is controlled. The rectangular voltage is applied to the stator winding with the power amplifier, the signals u_A, u_B, and i_A, as shown in Figure B.5, are recorded with the data recorder, and are post-processed as explained in Section 3.2.2.

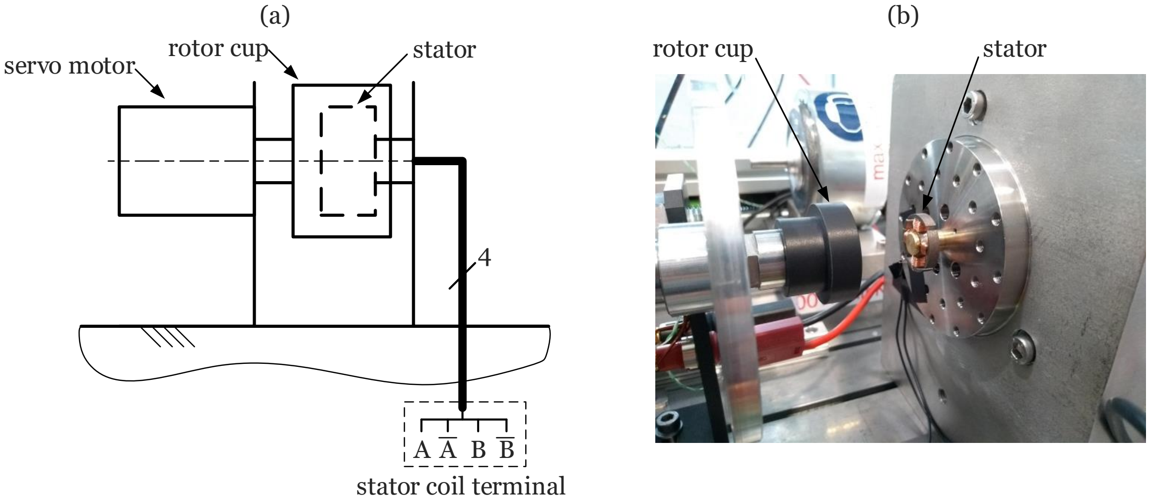
(a)
servo motor
rotor cup
stator
4
A
$\overline{\mathrm{A}}$
B
$\overline{\mathrm{B}}$
stator coil terminal
(b)
rotor cup
stator

Figure B.6: Motor test bench, (a) sketch of the mechanical setup and (b) detailed photo of the setup.

Appendix C

Computer Aided System Optimization

C.1 Switching Angle Investigations

C.1.1 Test-Setup for Switching Angle Investigations

Figures C.1 (a) and (b) show the block diagram and a picture of the experimental test setup, respectively. It comprises a data recorder (I), a BLDC motor (II), an encoder (III), a driver circuit (IV), current transducers (V), a rapid control prototyping system (VI), and a DC power supply (VII).

This setup is used for determining the experimental results presented in Section 4.3.2.

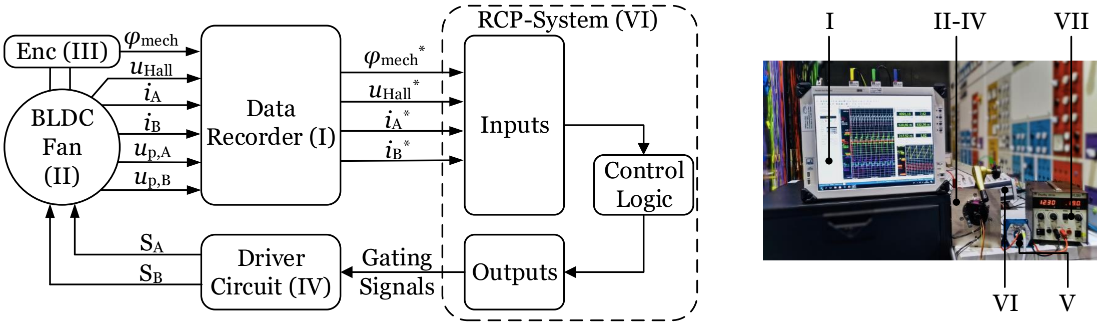
Enc (III)
BLDC Fan (II)
φ_{mech}
u_{Hall}
i_A
i_B
$u_{p,A}$
$u_{p,B}$
Data Recorder (I)
φ_{mech}^*
u_{Hall}^*
i_A^*
i_B^*
RCP-System (VI)
Inputs
Control Logic
Outputs
Gating Signals
Driver Circuit (IV)
S_A
S_B
I
II-IV
VII
VI
V

(a) (b)

Figure C.1: Block diagram of the experimental test setup, (a) sketch of the mechanical setup and (b) overview photo.

Circuit voltages and currents, the rotor position φ, and the signal of the Hall effect sensor are measured with the data recorder and processed with the rapid control prototyping system. The Hall sensor is mounted close to the rotor-magnet to properly detect the BEMF zero crossings and thus control the switches of the BLDC drive. To this aim, the magnetic encoder is synchronized with this Hall signal and measures the relative rotor position from the zero-crossing positions. Hence, commutation is possible at the desired rotor position.

The data are collected with a high precision data recorder Gen3i®, equipped with two GEN610B cards, from HBM® [81], three IT 60-S current transducers from LEM® [85], and an AEAT-601B magnetic encoder from Broadcom® [86].

C.2 Space Mapping

C.2.1 Transformation Case Study

The application of space mapping is illustrated for design modifications of the example case drive. From the example case drive's geometry, two scaled up geometries are introduced, increased by 20 % and 40 % in the radial direction. This creates a basis of 3 different motor sizes for interpolation. Motor dimensions and specifications are set with the parameters in Table 2.1 and Table 2.2 as provided in Section 2.1. The models are evaluated in terms of motor volumes $V_{\mathrm{M,tot}}$ and the motor efficiencies η_{M}. $V_{\mathrm{M,tot}}$ are provided by a parametric CAD model which is also utilized for FEA, the motor efficiencies η_{M} are determined with the multiphysical model introduced in Section 4.3.

Table C.1 presents the base points $\mathbf{B}_{\mathrm{f}}$ and $\mathbf{B}_{\mathrm{c}}$, with the corresponding model responses $\vec{R}_{\mathrm{f}}(\vec{\varphi}_{\mathrm{f}})$ and $\vec{R}_{\mathrm{c}}(\vec{\varphi}_{\mathrm{c}}$, containing motor volumes $V_{\mathrm{M,tot}}$ and the motor efficiencies η_{M} as conflicting objectives. R_{RO} is the outer rotor radius, e_{RRO} is the relative difference with respect to the basic version. e_{VMtot} and $e_{\eta_{\mathrm{M}}}$ are the relative differences with regard to the respective baseline version values.

Details on parameter and model response vectors are as follows:

$$\vec{\varphi}_{\mathrm{c,f}} = \left[R_{\mathrm{so}}\ h_{\mathrm{ag}}\ h_{\mathrm{mg}}\ d_1\ d_2\ d_3\ w_{\mathrm{s}}\right]^T , \tag{C.1}$$

$$\vec{R}_{\mathrm{c,f}} = \left[V_{\mathrm{M,tot}}\ \eta_{\mathrm{M}}\right]^T , \tag{C.2}$$

where $\vec{\varphi}_{\mathrm{c,f}}$ are parameter vectors containing the geometry information, and $\vec{R}_{\mathrm{c,f}}$ are the model response vectors, containing the motor volume $V_{\mathrm{M,tot}}$, and the motor efficiency η_{M}.

Table C.1: Basis of 3 different motor sizes for interpolation, from the example case drive's geometry two scaled up geometries in radial direction are provided. Presented are the outer-rotor radii R_{RO}, the total motor volumes $V_{\mathrm{M,tot}}$ and the motor efficiencies η_{M}.

model type –	radial length %	R_{RO} mm	$V_{\mathrm{M,tot}}$ mm^3	η_{M} %
coarse model	100	13.75	2523	48.8
	120	16.5	3694	62.8
	140	19.25	5112	73.1
fine model	100	13.75	2447	49.3
	120	16.5	3583	65.3
	140	19.25	4959	76.1

Table C.1 presents the models' responses for the same parameter vectors $\vec{\varphi}_{\mathrm{c}} = \vec{\varphi}_{\mathrm{f}}$. From this basis, the parameter vector of the coarse model $\vec{\varphi}_{\mathrm{c}}$ is varied by the optimization algorithm presented in Section 4.2.2, so that (C.3) holds.

$$\min_{\vec{\varphi}_{\mathrm{c,f}}\in\Re^n} \|\vec{R}_{\mathrm{f}}(\vec{\varphi}_{\mathrm{f}}) - \vec{R}_{\mathrm{c}}(\vec{\varphi}_c)\|, \tag{C.3}$$

The results of this mapping are provided in Table C.2. Information on the necessary mapping is available at the introduced three base points. To facilitate interpolation between these base points, a transformation **P** is established.

Table C.2: Results of the mapped coarse models to meet (C.3). e_{V} and e_η are the relative differences of $V_{\mathrm{M,tot}}$ and η_{M}, respectively. Additions m and f in the indices of (C.4) refer to the mapped and fine model, respectively.

model type –	radial length %	R_{RO} mm	$V_{\mathrm{M,tot}}$ mm^3	e_{V} %	η_{M} %	e_η %
mapped coarse model	100	13.3	2345	-4.2	49.1	-0.4
	120	16.0	3412	-4.8	63.9	-2.1
	140	18.9	4814	-2.9	74.8	-1.7

$$e_{\mathrm{V}} = \left(\frac{V_{\mathrm{M,tot\text{-}m}}}{V_{\mathrm{M,tot\text{-}f}}} - 1\right) \cdot 100\%; \; e_\eta = \left(\frac{\eta_{\mathrm{M\text{-}m}}}{\eta_{\mathrm{M\text{-}f}}} - 1\right) \cdot 100\% \tag{C.4}$$

The methodology for establishing the transformation **P** is provided in Section 4.4.2. Submitting fine and the mapped parameter vectors from this case study to (4.8) in Section 4.4.2 establishes the discussed linear transformation **P** between the base points $\mathbf{B}_{\mathrm{m,f}}$.

As discussed in Section 4.4.2, the transformation turned out to be not invertible with the limited parameter set of this case study. Iteratively adding more base points, as described above, may improve the quality of the transformation.

Bibliography

[1] A. Höfer, W. Peschkow, and P. Hamon, "Electric Axles in the Stress Field of NVH, Efficiency and Power Density," *ATZ worldwide*, vol. 122, no. 4, pp. 46–51, Apr. 2020.

[2] S. Leitner, H. Gruebler, and A. Muetze, "Innovative Low-Cost Sub-Fractional HP BLDC Claw-Pole Machine Design for Fan Applications," *IEEE Transactions on Industry Applications*, vol. 55, no. 3, pp. 2558–2568, Jan. 2019.

[3] A. Kunz, M. Kunz, H. Vollert, and M. Förster, "Electromechanical Brake Booster for all Drive Concepts and Automated Driving," *ATZ worldwide*, vol. 120, no. 4, pp. 58–61, Apr. 2018.

[4] J. Hirt, "Cooling and Dehumidification of LED Headlights," *ATZ worldwide*, vol. 116, no. 5, pp. 36–39, May 2014.

[5] A. Reul, K. Fecke, and H. Stobrawe, "Adjustable Oil Pump for the Lubrication of Transmissions," *ATZ worldwide*, vol. 116, no. 12, pp. 30–35, Nov. 2014.

[6] Volkswagen AG. (1997) 00054443000-Golf_Vento_-_Grundausstattung_ab_August_1995. [Accessed: Nov. 20, 2019]. [Online]. Available: https://erwin.volkswagen.de/

[7] ——. (2017) K0059210000-Grundausstattung_ab_August_2012. [Accessed: Nov. 20, 2019]. [Online]. Available: https://erwin.volkswagen.de/

[8] V. Unterfrauner, R. Winzer, and H. Messner, "Efficient and Cost-effective Transmission Actuation," *ATZ worldwide*, vol. 121, pp. 32–37, Nov. 2019.

[9] C. Köglsperger, V. Unterfrauner, and S. Zollitsch, "Brake-by-Wire - From Formula E to Concept Development," *ATZ worldwide*, vol. 122, pp. 54–59, Jan. 2020.

[10] T. Leiber, H. Leiber, and A. van Zanten, "Brake Boosters for Automated Driving," *ATZ worldwide*, vol. 121, pp. 48–53, Feb. 2019.

[11] S. Chowdhury, L. Leitzel, and M. Zima, "Thermal System for Electric Vehicles with Coolant-based Heat Pump," *ATZ worldwide*, vol. 121, no. 5, pp. 48–53, May 2019.

[12] Volkswagen AG. (2019) Annual Report 2018. [Accessed: Dec. 11, 2019]. [Online]. Available: https://www.volkswagenag.com/en/InvestorRelations/news-and-publications/Annual_Reports.html

[13] A. Muetze, S. Leitner, H. Gruebler, and F. Krall, "Performance Improvements of Auxiliary Drives for Automotive Pump and Fan Applications," *Elektrotechnik und Informationstechnik*, Apr. 2020.

[14] A. Neubert and M. Müller, "Validation of a Window Regulator - From Prototype to Product," *ATZ worldwide*, vol. 122, pp. 42–47, Aug. 2020.

[15] C.-L. Xia, *Permanent Magnet Brushless DC Motor Drives and Controls*. Singapore: Wiley, 2012, vol. (1., 1. publ. ed.).

[16] ThyssenKrupp Technologies AG. (2005) ThyssenKrupp Presta presents electric steering systems of the future. [Online]. Available: https://www.thyssenkrupp.com/en/newsroom/press-releases/press-release-47288.html

[17] A. Rau, "Dezentrale elektrische Antriebe im Automobil," *ATZ - Automobiltechnische Zeitschrift*, vol. 108, no. 11, pp. 940–944, Nov 2006.

[18] G.-J. Su and J. McKeever, "Low-Cost Sensorless Control of Brushless DC Motors With Improved Speed Range," *IEEE Transactions on Power Electronics*, vol. 19, no. 2, pp. 296–302, Mar 2004.

[19] X. Sun, Z. Deng, C. Wang, and J. Wu, "A Sensorless Method with Torque Ripple Suppression for Brushless DC Motors," in *2016 19th International Conference on Electrical Machines and Systems (ICEMS)*, Nov 2016, pp. 1–4.

[20] S. Ogasawara and H. Akagi, "An Approach to Position Sensorless Drive for Brushless DC Motors," in *Conference Record of the 1990 IEEE Industry Applications Society Annual Meeting*, vol. 1, Oct 1990, pp. 443–447.

[21] T. Lee, M. Seo, Y. Kim, and S. Jung, “Motor Design and Characteristics Comparison of Outer-Rotor-Type BLDC Motor and BLAC Motor Based on Numerical Analysis,” *IEEE Transactions on Applied Superconductivity*, vol. 26, no. 4, pp. 1–6, June 2016.

[22] S. Sakunthala, R. Kiranmayi, and P. N. Mandadi, “A study on industrial motor drives: Comparison and applications of PMSM and BLDC motor drives,” in *2017 International Conference on Energy, Communication, Data Analytics and Soft Computing (ICECDS)*, Aug. 2017, pp. 537–540.

[23] D. Hanselman, *Brushless Permanent Magnet Motor Design*, 2nd ed. Ohio, USA: Magna Physics Publishing, 2006.

[24] S. Huber, M. Koch, R. Krovvidi, and M. Fock, “Steering Actor for Safety-critical Systems,” *ATZ worldwide*, vol. 123, pp. 30–33, Jan 2021.

[25] S. Dunkl, A. Muetze, and G. Schoener, “Design Constraints of Small Single-Phase Permanent Magnet Brushless DC Drives for Fan Applications,” *IEEE Transactions on Industry Applications*, vol. 51, no. 4, pp. 3178–3186, Jul. 2015.

[26] L. L. Wang, J. X. Shen, P. C. K. Luk, W. Z. Fei, C. F. Wang, and H. Hao, “Development of a Magnetic-Geared Permanent-Magnet Brushless Motor,” *IEEE Transactions on Magnetics*, vol. 45, no. 10, pp. 4578–4581, Oct. 2009.

[27] B. K. Lee and M. Ehsani, “Advanced BLDC motor drive for low cost and high performance propulsion system in electric and hybrid vehicles,” in *IEMDC 2001. IEEE International Electric Machines and Drives Conference (Cat. No.01EX485)*, June 2001, pp. 246–251.

[28] W. Wang, Z. Wu, W. Jin, and J. Ying, “Starting methods for hall-less single phase BLDC motor,” in *31st Annual Conference of IEEE Industrial Electronics Society, 2005. IECON 2005.*, Nov. 2005.

[29] S. Bentouati, Z. Zhu, and D. Howe, “Permanent magnet brushless dc motors for consumer products,” *IET Conference Proceedings*, pp. 118–122(4), Jan. 1999. [Online]. Available: https://digital-library.theiet.org/content/conferences/10.1049/cp_19991001

[30] L. I. Iepure, L. Tutelea, and I. Boldea, “FEM analysis and control of a tapered airgap single phase PMSM,” in *2008 11th International Conference on Optimization of Electrical and Electronic Equipment*, May 2008, pp. 241–248.

[31] Hoe-Cheon Kimr, Jun-Hee Han, and Tae-Uk Jung, “Analysis of torque characteristic according to the asymmetrical airgap of the BLDC motor for cooling-fan,” in *2013 International Conference on Electrical Machines and Systems (ICEMS)*, Oct. 2013, pp. 1277–1280.

[32] H. Grübler, S. Leitner, A. Muetze, and G. Schoener, “Improved Switching Strategy for a Single-Phase Brushless Direct Current Fan Drive and its Impact on Efficiency,” *IEEE Transactions on Industry Applications*, vol. 54, no. 6, pp. 6050–6059, Nov. 2018.

[33] C. Chiu, Y. Chen, Y. Liang, and R. Liang, “Optimal Driving Efficiency Design for the Single-Phase Brushless DC Fan Motor,” *IEEE Transactions on Magnetics*, vol. 46, no. 4, pp. 1123–1130, April 2010.

[34] S. Leitner, H. Gruebler, and A. Muetze, “Low-Cost Sub-Fractional Horsepower Brushless Direct Current Claw-Pole Machine Topology for Fan Applications,” in *2018 IEEE Applied Power Electronics Conference and Exposition (APEC)*, Mar. 2018, pp. 1242–1248.

[35] Elmos Semiconductor AG. (2017) 500mA BLDC Motor Controller–E523.81. [Accessed: Oct. 22, 2019]. [Online]. Available: https://www.elmos.com/produkte/motor-control-ics/brushless-dc-motor-controller-ic/e52381.html

[36] Python Software Foundation. (2021) Python. [Feb., 09, 2021]. [Online]. Available: https://www.python.org/

[37] Linz Center of Mechatronics GmbH. (2021) SyMSpace - The System Model Space. [Feb., 09, 2021]. [Online]. Available: https://symspace.lcm.at/

[38] Analog Devices. (2020) LTspice Simulation Software. [Oct., 20, 2020]. [Online]. Available: https://www.analog.com/en/design-center/design-tools-and-calculators/ltspice-simulator.html

[39] JSOL Corporation. (2019) JMAG-Designer, FEA Software for Electromechanical Design. [Mar., 31, 2019]. [Online]. Available: https://www.jmag-international.com

[40] T. Kulterer, "Investigation of Stray Paths in Fractional Horsepower Permanent-Magnet Motors," Master's thesis, Electric Drives and Machines Institute - Graz University of Technology, 2019.

[41] D. C. Hanselman, *Brushless Permanent Magnet Motor Design*, 2nd ed. The Writers' Collective, 2003.

[42] D. Wilson, "Navigating the complexities of motor control," in *Texas Instruments Motor Control Compendium*, 2010.

[43] F. Krall, "Analysis and Implementation of Algorithms for Calculation of Iron Losses for Fractional Horsepower Electric Motors," Master's thesis, Graz University of Technology, 2017.

[44] R. Lazar and N. Hanigovszki, "Efficiency and Loss Distribution Comparison for a Motor Drive System with and without LC-Filter," in *2018 20th European Conference on Power Electronics and Applications (EPE'18 ECCE Europe)*, 2018, pp. P.1–P.8.

[45] T. Yamada, "Advances in JMAG Designer: Talk at TU Graz," *JSOL Corporation*, Jul. 2019.

[46] A. Krings and J. Soulard, "Overview and Comparison of Iron Loss Models for Electrical Machines," *Journal of Electrical Engineering*, vol. 10, pp. 162–169, May 2010.

[47] M. Reinlein, A. Hoffmann, T. Hubert, and A. Kremser, "Systematic error of analytical iron loss approaches in electrical machines," in *Innovative Small Drives and Micro-Motor Systems; 9. GMM/ETG Symposium*, 2013, pp. 1–6.

[48] T. Chevalier, A. Kedous-Lebouc, B. Cornut, and C. Cester, "A new dynamic hysteresis model for electrical steel sheet," *Physica B: Condensed Matter*, vol. 275, no. 1-3, pp. 197–201, Jan. 2000.

[49] L. Li, A. Kedous-Lebouc, A. Foggia, and J. Mipo, "An Iron Loss Model (Loss Surface) for FeCo Sheet and Its Application in Machine Design," in *The XIX International Conference on Electrical Machines - ICEM 2010*. IEEE, Sep. 2010.

[50] G. Bramerdorfer and D. Andessner, "Accurate and Easy-to-Obtain Iron Loss Model for Electric Machine Design," *IEEE Transactions on Industrial Electronics*, vol. 64, no. 3, pp. 2530–2537, Mar. 2017.

[51] F. Preisach, “Über die magnetische Nachwirkung,” *Zeitschrift für Physik*, vol. 94, no. 5-6, pp. 277–302, May 1935.

[52] D. Jiles and D. Atherton, “Theory of ferromagnetic hysteresis,” *Journal of Magnetism and Magnetic Materials*, vol. 61, no. 1-2, pp. 48–60, Sep. 1986.

[53] J. P. A. Bastos and N. Sadowski, *Magnetic Materials and 3D Finite Element Modeling*, C. Press, Ed. Taylor & Francis Group, 2014.

[54] M. J. D. Powell, “Some Algorithms for Thin Plate Spline Interpolation to Functions of Two Variables,” in *International Conference on Advances in Computational Mathematics*, New Delhi, Jan. 1993.

[55] S. Leitner, G. Krenn, H. Gruebler, and A. Muetze, “Rheometer-Based Cogging and Hysteresis Torque and Iron Loss Determination of Sub-Fractional Horsepower Motors,” *IEEE Transactions on Industry Applications*, vol. 56, no. 4, pp. 3679–3690, 2020.

[56] Stefan Leitner, Hannes Gruebler, and Annette Muetze, “Effect of Manufacturing on Magnetic Performance Parameters of Sub-Fractional Horsepower Motors,” unpublished.

[57] Germar Müller, Karl Vogt, and Bernd Ponick, *Berechnung elektrischer Maschinen*, 6th ed. Wiley-VCH, 2008, iSBN-13: 978-3-527-40525.

[58] U. Baumgartner, T. Ebner, and C. Magele, *Numerical Optimization*, 1st ed. Institute of Fundamentals and Theory in Electrical Engineering - Graz University of Technology, winterterm 2017/18.

[59] S. Luke, *Essentials of Metaheuristics*, 2nd ed. Lulu, 2013, available for free at http://cs.gmu.edu/~sean/book/metaheuristics/.

[60] I. Rechenberg, *Evolutionsstrategie : Optimierung technischer Systeme nach Prinzipien der biologischen Evolution*, ser. Problemata. Stuttgart-Bad Cannstatt: Frommann-Holzboog, 1973, no. 15.

[61] J. H. Holland, “Genetic Algorithms,” *Scientific American*, vol. 267, no. 1, pp. 66–73, 1992. [Online]. Available: http://www.jstor.org/stable/24939139

[62] ——, *Adaptation in Natural and Artificial Systems: An Introductory Analysis with Applications to Biology, Control and Artificial Intelligence*. Cambridge, MA, USA: MIT Press, 1992.

[63] R. Otten and L. van Ginneken, *The Annealing Algorithm*, ser. The Springer International Series in Engineering and Computer Science. Springer US, 1989, no. 72.

[64] D. Wang, D. Tan, and L. Liu, "Particle swarm optimization algorithm: an overview," *Soft Computing*, vol. 22, pp. 387–408, 2018.

[65] K. Deb, A. Pratap, S. Agarwal, and T. Meyarivan, "A fast and elitist multiobjective genetic algorithm: NSGA-II," *IEEE Transactions on Evolutionary Computation*, vol. 6, no. 2, pp. 182–197, 2002.

[66] H. Gruebler, F. Krall, S. Leitner, and A. Muetze, "Loss-Surface-Based Iron Loss Prediction for Fractional Horsepower Electric Motor Design," in *2018 20th European Conference on Power Electronics and Applications (EPE'18 ECCE Europe)*, Sep. 2018, pp. P.1–P.8.

[67] N. Marheinke and R. Pinnau, "Model hierarchies in space-mapping optimization: Feasibility study for transport processes," *Journal of Computational Methods in Sciences and Engineering*, vol. 12, no. 1-2, pp. 63–74, May 2012.

[68] O. Lass, C. Posch, G. Scharrer, and S. Volkwein, "Space mapping techniques for a structural optimization problem governed by the p-Laplace equation," *Optimization Methods and Software*, vol. 26, no. 4-5, pp. 617–642, Aug. 2011.

[69] M. K. Banda and M. Herty, "Towards a space mapping approach to dynamic compressor optimization of gas networks," *Optimal Control Applications and Methods*, vol. 32, no. 3, pp. 253–269, May 2011.

[70] M. Redhe and L. Nilsson, "Optimization of the new Saab 9-3 exposed to impact load using a space mapping technique," *Structural and Multidisciplinary Optimization*, vol. 27, no. 158, pp. 411–420, May 2004.

[71] G. Bramerdorfer, J. A. Tapia, J. J. Pyrhönen, and A. Cavagnino, "Modern Electrical Machine Design Optimization: Techniques, Trend, and Best Practices," *IEEE Transactions on Industrial Electronics*, vol. 65, no. 10, pp. 7672–7684, Feb. 2019.

[72] S. Silber, W. Koppelstätter, G. Weidenholzer, G. Segon, and G. Bramerdorfer, “Reducing Development Time of Electric Machines with SyMSpace,” in *2018 8th International Electric Drives Production Conference (EDPC)*, Dec. 2018, pp. 1–5.

[73] T. W. Simpson. (1998) Comparison of Response Surface and Kriging Models in the Multidisciplinary Design of an Aerospike Nozzle. [Accessed: Oct. 22, 2019]. [Online]. Available: https://ntrs.nasa.gov/archive/nasa/casi.ntrs.nasa.gov/19980046640.pdf

[74] J. W. Bandler, R. M. Biernacki, S. H. Chen, P. A. Grobelny, and R. H. Hemmers, “Space mapping technique for electromagnetic optimization,” *IEEE Transactions on Microwave Theory and Techniques*, vol. 42, no. 12, pp. 2536–2544, Dec. 1994.

[75] R. B. Ayed, J. Gong, S. Brisset, F. Gillon, and P. Brochet, “Three-Level Output Space Mapping Strategy for Electromagnetic Design Optimization,” *IEEE Transactions on Magnetics*, no. 2, pp. 671–674, Feb. 2012.

[76] L. Encica, J. J. H. Paulides, E. A. Lomonova, and A. J. A. Vandenput, “Aggressive Output Space-Mapping Optimization for Electromagnetic Actuators,” *IEEE Transactions on Magnetics*, vol. 44, no. 6, pp. 1106–1109, Jun. 2008.

[77] G. Crevecoeur, L. Dupre, and R. V. de Walle, “Space Mapping Optimization of the Magnetic Circuit of Electrical Machines Including Local Material Degradation,” *IEEE Transactions on Magnetics*, vol. 43, no. 6, pp. 2609–2611, Jun. 2007.

[78] A. J. Booker, J. E. Dennis, P. Frank, D. Serafini, V. Torczon, and M. Trosset, “A rigorous framework for optimization of expensive functions by surrogates,” *Structural and Multidisciplinary Optimization*, vol. 1, no. 1, pp. 1–13, Feb. 1999.

[79] J. Bandler, “Space Mapping-Have You Ever Wondered About the Engineer's Mysterious “Feel" for a Problem? [Speaker's Corner],” *IEEE Microwave Magazine*, vol. 19, no. 2, pp. 112–122, Mar. 2018.

[80] *Systematic embodiment design of technical products*, Verein Deutscher Ingenieure (VDI) Std. VDI2223, 2004.

[81] HBM GmbH. (2018) HBM Genesis High-Speed Data Aquisition System. [Accessed: May, 19, 2018]. [Online]. Available: https://www.hbm.com/en/3868/data-recorder-gen3i-and-transient-recorder/

[82] Dr. Brockhaus Messtechnik GmbH. (2020) Fluxmeter F10. [Accessed: Dec, 17, 2020]. [Online]. Available: https://brockhaus.com/measurements/products/hardmagnetic/flux-series/f10/

[83] *Magnetic Materials - Part 4: Methods of measurement of d.c. magnetic properties of magnetically soft materials*, International Electrotechnical Commission (IEC) Std. 60 404-2, Rev. 2009-08, 1995.

[84] Faulhaber Group. (2021) 4490H036B BLDC Servomotor. [Accessed: Mar., 8, 2021]. [Online]. Available: https://www.faulhaber.com/en/products/series/4490b/

[85] LEM Holding SA. (2014) Current Transducer IT 60-S ULTRASTAB. [Accessed: May, 19, 2018]. [Online]. Available: https://www.lem.com/en/it-60s-ultrastab

[86] Broadcom Ltd. (2018) AEAT-601B-F06 Magnetic Incremental Encoder. [Accessed: Jan, 22, 2018]. [Online]. Available: https://www.broadcom.com/products/motion-control-encoders/magnetic-encoders/aeat-601bf06